Title
Development of Molecular Catalysts to Bridge the Gap between Heterogeneous and Homogeneous Catalysts

Author
Ye, Rong

Publication Date
2017

Peer reviewed|Thesis/dissertation

Development of Molecular Catalysts to Bridge the Gap between Heterogeneous and Homogeneous Catalysts

by
Rong Ye

A dissertation submitted in partial satisfaction of the
requirements for the degree of
Doctor of Philosophy
in
Chemistry
in the
Graduate Division
of the
University of California, Berkeley

Committee in charge:

Professor Gabor A. Somorjai, Chair
Professor F. Dean Toste
Professor Alexander Katz

Fall 2017

Abstract

Development of Molecular Catalysts to Bridge the Gap between Heterogeneous and Homogeneous Catalysts
by

Rong Ye

Doctor of Philosophy in Chemistry

University of California, Berkeley

Professor Gabor A. Somorjai, Chair

Catalysts, heterogeneous, homogeneous, and enzymatic, are comprised of nanometer-sized inorganic and/or organic components. They share molecular factors including charge, coordination, interatomic distance, bonding, and orientation of catalytically active atoms. By controlling the governing catalytic components and molecular factors, catalytic processes of a multichannel and multiproduct nature could be run in all three catalytic platforms to create unique end-products. Unifying the fields of catalysis is the key to achieving the goal of 100% selectivity in catalysis.

Recyclable catalysts, especially those that display selective reactivity, are vital for the development of sustainable chemical processes. Among available catalyst platforms, heterogeneous catalysts are particularly well-disposed toward separation from the reaction mixture via filtration methods, which renders them readily recyclable. Furthermore, heterogeneous catalysts offer numerous handles – some without homogeneous analogues – for performance and selectivity optimization. These handles include nanoparticle size, pore profile of porous supports, surface ligands and interface with oxide supports, and flow rate through a solid catalyst bed. Despite these available handles, however, conventional heterogeneous catalysts are themselves often structurally heterogeneous compared to homogeneous catalysts, which complicates efforts to optimize and expand the scope of their reactivity and selectivity.

Ongoing efforts are aimed to address the above challenge by heterogenizing homogeneous catalysts, which can be defined as the modification of homogeneous catalysts to render them in a separable (solid) phase from the starting materials and products. Specifically, we grow the small nanoclusters in dendrimers, a class of uniform polymers with the connectivity of fractal trees and generally radial symmetry. Thanks to their dense multivalency, shape persistence and structural uniformity, dendrimers have

proven to be versatile scaffolds for the synthesis and stabilization of small nanoclusters. Then these dendrimer-encapsulated metal clusters (DEMCs) are adsorbed onto mesoporous silica. Through this method, we have achieved selective transformations that had been challenging to accomplish in a heterogeneous setting, e.g. π-bond activation and aldol reactions. Extensive investigation into the catalytic systems under reaction conditions allowed us to correlate the structural features (e.g. oxidation states) of the catalysts and their activity. Moreover, we have demonstrated that supported DEMCs are also excellent catalysts for typical heterogeneous reactions, including hydrogenation and alkane isomerization. Critically, these investigations also confirmed that the supported DEMCs are heterogeneous and stable against leaching.

Catalysts optimization is achieved through the modulation of various parameters. The clusters are oxidized (e.g., with $PhICl_2$) or reduced (e.g., with H_2) *in situ*. Changing the dendrimer properties (e.g., generation, terminal functional groups) is analogous to ligand modification in homogeneous catalysts, which affect both catalytic activity and selectivity. Similarly, pore size of the support is another factor in determining product distribution. In a flow reactor, the flow rate is adjusted to control the residence time of the starting material and intermediates, and thus the final product selectivity.

Our approach to heterogeneous catalysis affords various advantages: (1) the catalyst system can tap into the reactivity typical to homogeneous catalysts, which conventional heterogeneous catalysts could not achieve; (2) unlike most homogeneous catalysts with comparable performance, the heterogenized homogeneous catalysts can be recycled; (3) improved activity or selectivity compared to conventional homogeneous catalysts is possible because of uniquely heterogeneous parameters for optimization.

While localized surface plasmon resonance (LSPR) provides a powerful platform for nanoparticle catalysis, our studies suggest that in some cases interband transitions should be considered as an alternative mechanism of light-driven nanoparticle catalysis. The benefits already demonstrated by plasmonic nanostructures as catalysts provided the impetus for examining complementary activation modes based on the metal nanoparticle itself. Leveraging these transitions has the potential to provide a means to highly active catalysis modes that would otherwise be challenging to access. For example, for the preparation of highly active metal catalysts on a subnanosized scale is challenging, thus limiting their exploitation and study in catalysis. Our work suggests a novel and facile strategy for the formation of highly active gold nanocluster catalysts by light illumination of the interband transitions in the presence of the appropriate substrate.

Table of Contents

Acknowledgements

I would like to thank Professor Gabor Somorjai for giving me the opportunity to work in his laboratory and for providing research directions. His multidisciplinary research program allows me to access a wide range of research areas and learn a variety of techniques in my graduate study. I would like to specifically thank Professor Somorjai for being a role model in a scientific career, assigning me challenging projects that increase my competence and skill level, communicating strong support and confidence in me, offering counseling in my career development, providing sponsorship for awards, and protection from unproductive criticism. I will be forever grateful for his constant kindness, guidance and support. I would like to thank Ms. Inger Coble for her immense support, and continuous assistance in handling nearly every problem that arises within the Somorjai group.

During my time in the Somorjai group, I was taught by many people and I would like to thank the entire group from 2013 – 2017 for their help. I am especially grateful to Dr. Elad Gross, Dr. Kyungsu Na, Dr. Selim Alayoglu, Dr. Walter Ralston, Dr. Christophe Deraedt, and Mr. Wen-Chi Liu for mentoring and/or scientific discussions. I am also very fortunate to be able to work with four talented undergraduate students, Ms. Bing Yuan, Mr. Franco F. Faucher, Mr. Matthew Chang, and Mr. Brent Wickemeyer. I learned a lot from working with them as a research mentor.

Outside the Somorjai group, I was extremely fortunate to collaborate with the Toste group, the Alivisatos group, and the Zheng group. I would like to thank Prof. F. Dean Toste for being my co-advisor in research and providing valuable advice on experimental details in specific and research directions in general. In addition to these group leaders, I am grateful to Dr. Jie Zhao, Dr. Aleksandr Zhukhovitskiy, Dr. Hexiang Deng, Dr. Yue-Biao Zhang, Dr. Juncong Jiang, Dr. Son Nguyen, Dr. Kai-Yang Niu, and Dr. Feng Lin, who broadened my horizons in research.

I thank Ms. Lynn Keithlin, who helped me out during my difficult times in switching research groups. She allowed me to earn my living as a graduate student instructor, which shaped my teaching skills and enabled me to win the teaching awards later. I could not keep a positive mind in looking for a reliable advisor without her encouragement, either.

I also thank the Graduate Student Instructor teaching and resource center at UC Berkeley, especially Dr. Linda M. von Hoene, for training me to be confident as a graduate student instructor and grating me three prestigious campus-wide teaching awards and a teaching certificate. In addition, she inspired me to be a qualified research mentor through the Student Mentoring and Research Teams (SMART) program.

I would like to thank my family. My mother and father have provided endless support for me, not only during my time at Berkeley, but throughout my entire life. My parents supported me for two decades of school and pushed me to always do my best.

They supported my decision to study abroad and many other decisions I made without interference. I will be forever grateful.

The research contained within this dissertation was supported by the U.S. Department of Energy, Office of Science, Office of Basic Energy Sciences, Chemical Sciences, Geosciences, and Biosciences Division, under contract DE-AC02-05CH11231.

Introduction

This dissertation contains eight chapters. Chapter 1 provides an overview of modern molecular catalysis science and explains the desire to unify the heterogeneous, homogeneous, and enzyme catalysts. Chapter 2 discusses the main experimental techniques involved in the research in this dissertation. Chapter 3 gives an overview of the supported dendrimer-encapsulated metal clusters, a key research area in this dissertation. Chapters 4-6 cover the details of studying supported dendrimer-encapsulated metal clusters in specific reactions, including the ring-opening of cyclopropane derivatives, aldol reactions, and the hydroisomerization of methylcyclopentane. Chapter 7 covers an unexpected method of the formation of highly active clusters, i.e., through the hot carriers generated from harvesting the energy from light via the interband transition of gold nanoparticles. A thorough investigation of the mechanism of the hot carrier generation is presented. Chapter 8 provides a different way of studying the hydroisomerization of methylcyclopentane, namely, through platinum nanoparticles supported onto mesoporous zeolites. The effects of acid concentrations and strengths on the product selectivity are analyzed in detail.

An artwork designed for the manuscript of Chapter 3 was published as the cover art of the September Issue of *Accounts of Chemical Research* in 2017. Since this cover art can serve as an apt illustration of the theme of this dissertation, it is cited below (credit: American Chemical Society). In this figure, the tree rooted to the ground represents a supported dendrimer. The yellow spheres on the left or right side of the branches denotes the metal clusters in the reduced (metallic) or oxidized (ionic) states, respectively. The supported dendrimer-encapsulated metal clusters are able to accelerate reactions that typically require either heterogeneous (e.g. hydrogenation) or homogeneous (π-bond activation) catalysts. Thus, the catalyst system of supported dendrimer-encapsulated metal clusters represents a strategy of bridging the gap between heterogeneous and homogeneous catalysis.

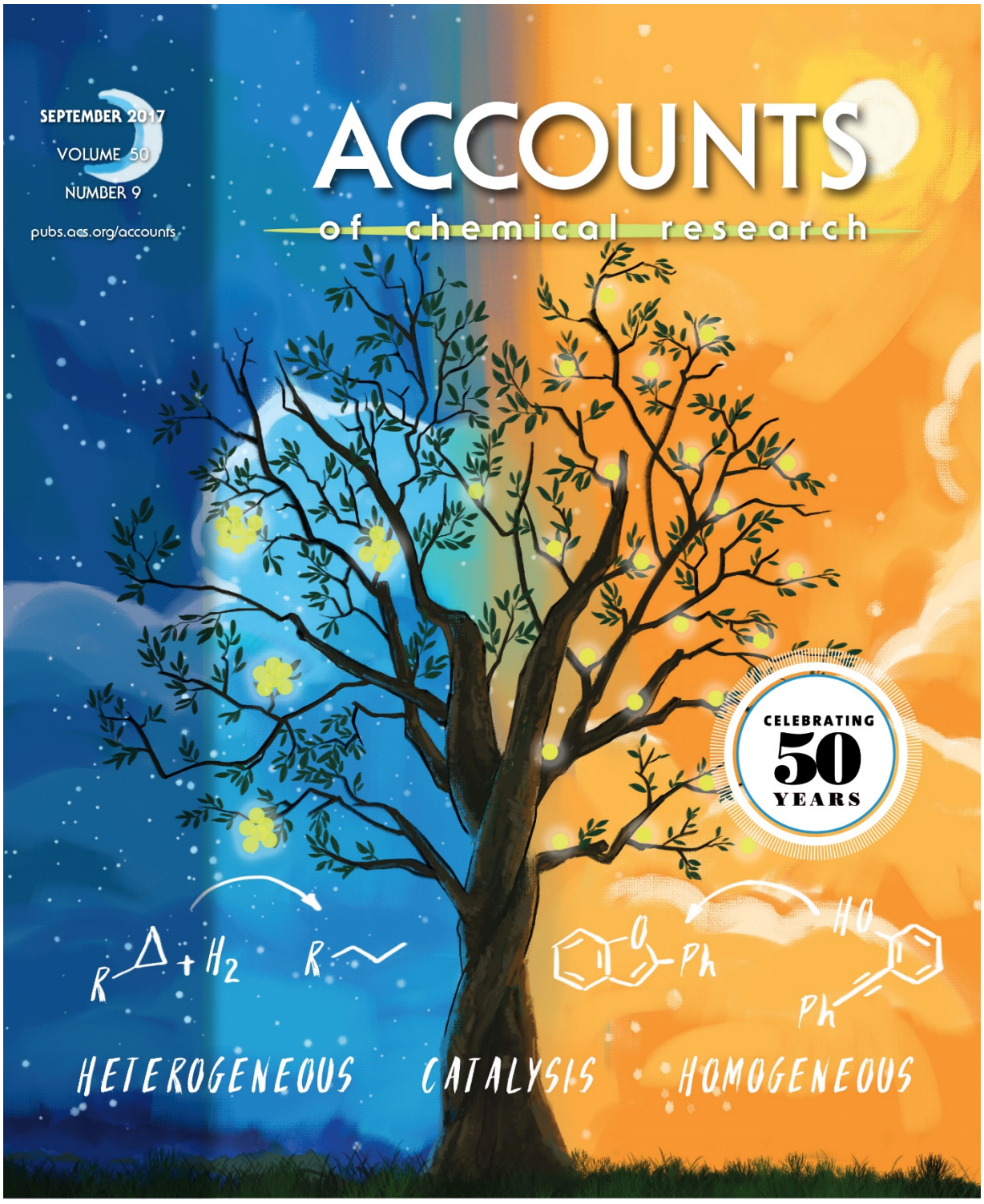

Curriculum Vitae (as of November 2017)

EDUCATION

University of California, Berkeley: Ph.D. candidate, Physical Chemistry, 2013–2017 (expected)

Advisor: Prof. Gabor A. Somorjai; **Co-advisor**: Prof. F. Dean Toste.

University of California, Los Angeles: M.S., Inorganic Chemistry, 2011–2012

Sun Yat-Sen University: B.E., Polymeric Material and Engineering, 2007–2011

Advisor: Prof. Xiao-Ming Chen.

RESEARCH

Doctoral research in the groups of Prof. Gabor A. Somorjai and Prof. F. Dean Toste, University of California, Berkeley, Berkeley, CA (2013 – present)

- Development of highly active and recyclable dendrimer-encapsulated nanocatalysts with tunable product selectivity.
- Mechanistic investigation of metal nanoparticle-catalyzed solution phase organic reactions.
- Development of novel heterogeneous catalysts to achieve enantioselectivity.

These projects involve (1) a wide repertoire of colloidal synthesis of precious metal nanoparticles and mesoporous materials, (2) characterization of these materials (e.g., TEM, ICP-OES, physisorption), (3) surface characterization (e.g., XPS, EXAFS), (4) structure determination techniques (e.g., NMR spectroscopy, GC-MS).

HONORS & AWARDS

1. The International Precious Metals Institute Student Award for Precious Metals Research (2017)
2. Student Mentoring and Research Teams (SMART) graduate mentor of UC Berkeley (2017) – top 1%
3. Materials Research Society Graduate Student Silver Award (2017)
4. ACS Graduate Student Travel Award (2017)
5. Teagle Foundation Award for Excellence in Enhancing Student Learning (2015) – 1 of 3 Awarded idea: "Prompting Critical Thinking through Metacognition and Electronic Scheduling".

6. Teaching Effectiveness Award (2015) – 1 of 14
   Awarded idea: "Achieving Higher Efficiency in Chemistry Labs Using Electronic Scheduling".
7. Outstanding Graduate Student Instructor Award (2014) – top 9%
8. National Scholarship for Outstanding Undergraduates in China (2009) – top 1%
9. First Class Scholarship for Outstanding Students of SYSU (2007-2010) – top 5%

PUBLICATIONS (# indicates equal contribution)

1. **Ye, R.**; Zhukhovitskiy, A. V.; Deraedt, C. V.; Toste, F. D.; Somorjai, G. A. Supported Dendrimer-encapsulated Metal Clusters: Toward Heterogenizing Homogeneous Catalysts, *Acc. Chem. Res.* **2017**, *50*, 1894-1901. **(Selected for Cover Art for the September Issue)**
2. **Ye, R.**;[#] Zhao, J.;[#] Yuan, B.;[#] Liu, W.-C.; De Araujo, J. R.; Faucher, F. F.; Chang, M.; Deraedt, C. V.; Toste, F. D.; Somorjai, G. A. New Insights into Aldol Reactions of Methyl Isocyanoacetate Catalyzed by Heterogenized Homogeneous Catalysts, *Nano Lett.* **2017**, *17*, 584–589.
3. **Ye, R.**; Yuan, B.; Zhao, J.; Ralston, W. T.; Wu, C.-Y.; Unel Barin, E.; Toste, F. D.; Somorjai, G. A. Metal Nanoparticles Catalyzed Selective Carbon-Carbon Bond Activation in the Liquid Phase. *J. Am. Chem. Soc.* **2016,** *138*, 8533-8537.
4. **Ye, R.**; Hurlburt, T. J.; Sabyrov, K.; Alayoglu, S.; Somorjai, G. A. Molecular catalysis science: Perspective on unifying the fields of catalysis. *Proc. Natl. Acad. Sci. U. S. A.* **2016,** *113*, 5159-5166.
5. **Ye, R.**; Liu, W.-C.; Han, H.-L.; Somorjai, G. A. Development and Elucidation of Superior Turnover Rates and Selectivity of Supported Molecular Catalysts. *ChemCatChem*. DOI: 10.1002/cctc.201701546.
6. Zhao, J.;[#] Nguyen, S.;[#] **Ye, R.**;[#] Ye, B.;[#] Weller H.; Somorjai, G. A.; Alivisatos, A. P.; Toste. F. D. A comparison of photo-catalytic activities and of gold nanoparticles following plasmonic and interband excitation and a strategy for harnessing interband hot carriers for solution phase oxidative photo-catalysis, *ACS Cent. Sci.*, **2017**, *3*, 482−488.
7. Niu, K.-Y.;[#] Fang, L.;[#] **Ye, R.**;[#] Nordlund, D.; Doeff, M. M.; Lin, F.; Zheng, H. Tailoring Transition-Metal Hydroxides and Oxides by Photon-Induced Reactions. *Angew. Chem. Int. Ed.* **2016,** *55*, 14272-14276.
8. Deraedt, C. V.; **Ye, R.**; Toste, F. D.; Somorjai, G. A. Metal Nanoparticles Stabilized by Dendrimer as Very Efficient Catalysts for the Reverse Dehydrogenation/Hydrogenation of N-heterocycles. *J. Am. Chem. Soc.* DOI: 10.1021/jacs.7b10768.
9. Niu, K.-Y.;[#] Xu, Y.;[#] Wang, H.;[#] **Ye, R.**; Xin, H.; Tian, C.; Lin, F.; Lum, Y.; Bustillo, K.; Koper, M. T. M; Doeff, M. M; Ager, J.; Xu, R.; Zheng, H. A Spongy Nickel-Organic Photocatalyst for Nearly 100% Selective CO_2 to CO Conversion, *Science Adv.* **2017**, *3*, e1700921.
10. Deraedt, C. V. ; Melaet, G.; Ralston, W. T.; **Ye, R.**; Somorjai, G. A. Platinum and Other

Transition Metal Nanoclusters (Pd, Rh) Stabilized by PAMAM Dendrimer as Excellent Heterogeneous Catalysts: Application To the MethylCycloPentane (MCP) Hydrogenative Isomerisation. *Nano Lett.*, **2017,** *17*, 1853-1862.

11. Liu, W.-C.; Melaet, G.; Ralston, W. T.; Alayoglu, S.; Horowitz, Y.; **Ye, R.**; Hurlburt, T.; Mao, B.; Crumlin, E.; Salmeron, M.; Somorjai, G. A. Co–Rh Nanoparticles for the Hydrogenation of Carbon Monoxide: Catalytic Performance Towards Alcohol Production and Ambient Pressure X-Ray Photoelectron Spectroscopy Study. *Catal. Lett.* **2016,** *146*, 1574-1580.
12. Na, K.; Alayoglu, S.; **Ye, R.**; Somorjai, G. A. Effect of Acidic Properties of Mesoporous Zeolites Supporting Pt Nanoparticles on Hydrogenative Conversion of Methylcyclopentane. *J. Am. Chem. Soc.* **2014,** *136*, 17207-17212.
13. Hurlburt, T. J.; Liu, W.-C.; **Ye, R.**; Somorjai, G. A. Surface Science Approach to the Molecular Level Integration of the Principles in Heterogeneous, Homogeneous, and Enzymatic Catalysis. *Top. Catal.* Submitted on 10/26/2017.
14. **Ye, R.**; Zhao, J.; Wickemeyer, B. B.; Toste, F. D.; Somorjai, G. A. Integration of Homogeneous, Heterogeneous, and Enzyme Catalysts for Optimized Performances. *Nat. Catal.* Submitted on 11/2/2017.
15. **Ye, R.**; Faucher, F. F.; Somorjai, G. A. Supported Iron Catalysts for Michael Addition Reactions. *J. Mol. Catal. A: Chem.* Submitted on 11/5/2017.

JOURNAL REVIEWING

Peer reviewing for <*J. Am. Chem. Soc.*>, <*ACS Catal.*>, <*Catal. Lett.*>, <*ChemCatChem*>, <*J. Mol. Catal. A: Chem*>, etc. Independently reviewed 20+ articles.

TEACHING & SERVICE

Graduate student mentor: University of California, Berkeley, 2014 – present

Mentored five undergraduates or visiting students:

Bing Yuan, June 2014 – December 2016

Ebru Unel Barin, January 2015 – January 2016

Matthew Chang, August 2016 – June 2017

Franco F. Faucher, August 2016 – December 2017

Brent Wickemeyer June 2017 – December 2017

Laboratory safety coordinator: University of California, Berkeley, January 2014 – August 2015

Graduate student instructor: University of California, Berkeley

- Chem 112A- Organic chemistry (lecture and lab), Fall 2013
- Chem 3A- Chemical Structure and Reactivity (lecture and lab), Spring and Summer 2013

Teaching assistant: University of California, Los Angeles

Chem 20A- Chemical Structure (discussion section), Fall 2011 and Winter 2012

ORAL/POSTER PRESENTATIONS

1. MRS Fall Meeting & Exhibit, Boston, Massachusetts, November 26 – December 1, 2017
2. Nanoporous Materials & Their Applications Gordon Research Conference, Proctor Academy, Andover, NH, US, August 6-11, 2017
3. Cambridge-Berkeley Exchange Workshop, Bodega Bay, CA, US, July 16 – 21, 2017
4. 41st annual International Precious Metal Institute Conference, Orlando, FL, US, June 10 – 14, 2017
5. 25th North American Catalysis Society Meeting, Denver, CO, US, June 4 – 9, 2017
6. 253rd American Chemical Society National Meeting, San Francisco, CA, US, April 2 – 6, 2017
7. 252nd American Chemical Society National Meeting, Philadelphia, PA, US, August 21 – 25, 2016

Chapter 1 – Molecular Catalysis Science: Perspective on Unifying the Fields of Catalysis

(This chapter covers similar material as in Ye, R.; Hurlburt, T. J.; Sabyrov, K.; Alayoglu, S.; Somorjai, G. A. *Proc. Natl. Acad. Sci. U.S.A.* **2016**, *113*, 5159-5166. – reproduced with permission, copyright 2016 National Academy of Sciences.)

Abstract

Colloidal chemistry is used to control the size, shape, morphology, and composition of metal nanoparticles. Model catalysts as such are applied to catalytic transformations in the three types of catalysts: heterogeneous, homogeneous, and enzymatic. Real-time dynamics of oxidation state, coordination, and bonding of nanoparticle catalysts are put under the microscope using surface techniques such as sum-frequency generation vibrational spectroscopy and ambient pressure X-ray photoelectron spectroscopy under catalytically relevant conditions. It was demonstrated that catalytic behavior and trends are strongly tied to oxidation state, the coordination number and crystallographic orientation of metal sites, and bonding and orientation of surface adsorbates. It was also found that catalytic performance can be tuned by carefully designing and fabricating catalysts from the bottom up. Homogeneous and heterogeneous catalysts, and likely enzymes, behave similarly at the molecular level. Unifying the fields of catalysis is the key to achieving the goal of 100% selectivity in catalysis.

1.1 Background and motivation

During the last 20 years the field of catalysis has evolved into molecular science. Its exponential rise in applications and the publications that it has produced testify to its utility and scientific and technological importance. This chapter aims to summarize how this happened and points to the future in two areas of focus: 1) the molecular science of chemical energy conversion, and 2) possible integration of the three fields of catalysis, heterogeneous, homogeneous, and enzyme. Our laboratory is among the few where the field of catalysis is investigated in an integrated manner in order to develop a molecular understanding of the field of catalysis.

Two major breakthroughs have revolutionized molecular catalysis science over the last 20 years. The first is in the development of nanomaterials science,[1-4] which has made it possible to synthesize metallic,[5-7] bimetallic, and core-shell nanoparticles;[8,9] mesoporous metal oxides;[10,11] and enzymes[12-16] in the nanocatalytic range between 0.8 and 10 nm. The second innovation is in the advancement of spectroscopy and microscopy instruments[17-20] — including nonlinear laser optics;[21] sum-frequency generation vibrational spectroscopy;[22-24] and synchrotron-based instruments, such as ambient pressure X-ray photoelectron spectroscopy,[8,25-27] X-ray absorption near-edge structure (XANES), extended X-ray absorption fine structure (EXAFS),[28-30] infrared (IR) and X-ray microspectroscopies,[31] and high-pressure scanning tunneling microscopies[32,33] — that characterize catalysts at the atomic and molecular levels under reaction conditions.[34] Most of the studies that utilize these techniques focus on nanoscale technologies, such as catalytic energy conversion and information storage, which have reduced the size of transistors to below 25 nm.[35]

Catalysts are classified into three types — heterogeneous, homogeneous, and enzymatic — and in most cases range in size from 1 to 10 nm, which is even smaller than the transistors being developed by the latest size-fabrication technologies. Heterogeneous catalysts work in reaction systems with multiple phases, e.g., solid-gas or solid-liquid phase; homogeneous catalysts reside in the same phase as the reactants, almost always in the liquid phase; and enzymatic catalysts, which are most active in an aqueous solution, make use of active sites in proteins. The catalysis of chemical energy conversion provides ever-increasing selectivity in producing combustible hydrocarbons, gasoline, and diesel.

The tenets that direct our catalysis research involve nanoparticle synthesis; characterization under reaction conditions; and reaction studies using these nanoparticles to determine kinetics, selectivity, deactivation, and other catalytic kinetic parameters. These variables are studied in the same research group as they are the underpinning of molecular catalysis. The hypothesis that we are striving to support is that the three fields of catalysis (heterogeneous, homogeneous and enzyme) behave similarly on the molecular level. These ongoing studies as well as their success and future outlook are the subjects of this chapter.

1.2 Metal nanoparticles for size-dependent covalent bond catalysis

The major technique for the synthesis of nanoparticle catalysts is colloid chemistry (Fig. 1*A*). These nanoparticle-based catalysts are produced with precisely controlled sizes in the 1-10 nm range in two dimensions using the Langmuir-Blodgett technique[36] or placed on porous three-dimensional supports. The nanoparticles, mostly metals, are placed in a microporous and mesoporous support. The mesoporous support is made with mesoporous silica between 5-25 nm pores coated by a transition metal oxide. The silica is removed by leaching with sodium hydroxide to leave behind a mesoporous template that is loaded up with nanoparticles used for catalytic studies. The oxide itself, as it will be shown, is often a very important ingredient for catalytic reactions[34].

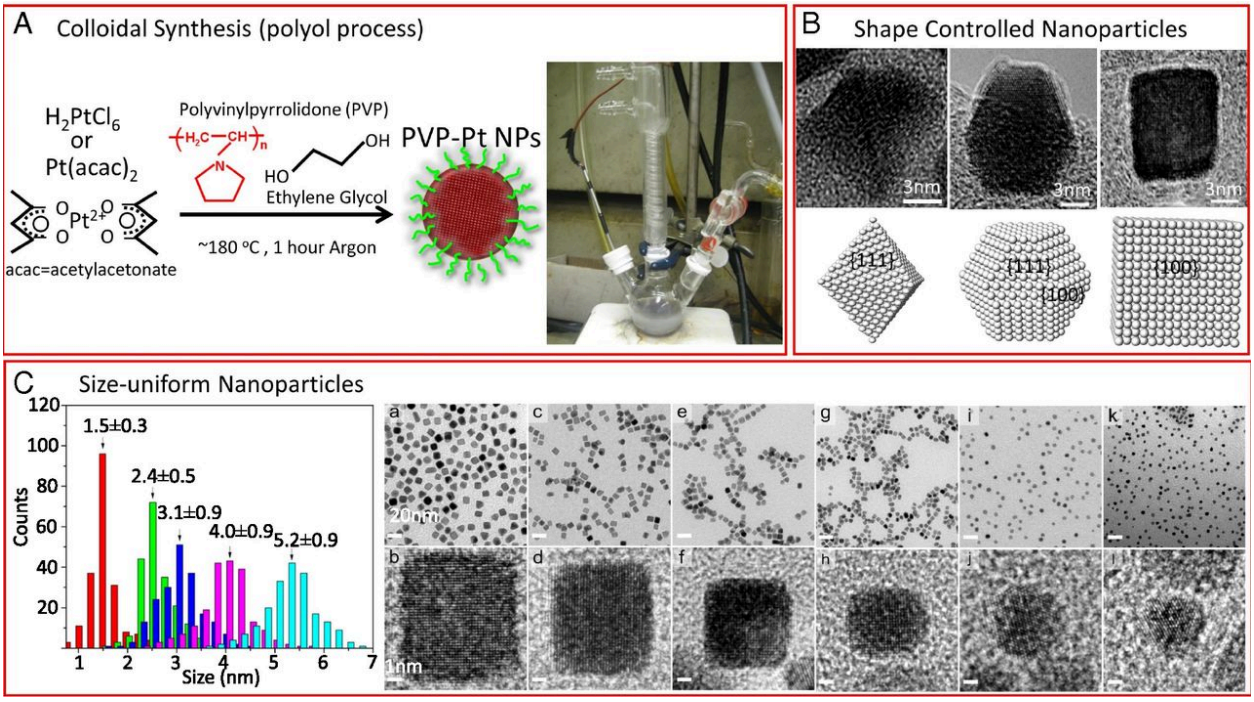

Fig. 1. Examples of size and shape control of nanoparticles. (*A*) Schematics of Pt nanoparticles synthesis by the polyol reduction method. (*B*) Transmission electron microscopy (TEM) images and ball models of Pt nanoparticles with different shapes. (*C*) Left: Particle size distribution histograms of the Pt/SBA-15 series catalysts obtained from TEM images. The number inserts indicate the mean particle diameter and standard deviation for each sample. Right: TEM and HRTEM images of Pt nanocrystals with different shape and size. TEM images of (*a*) 9 nm nanocubes, (*c*) 7 nm nanocubes, (*e*) 6 nm nanocubes, (*g*) 5 nm nanocubes, (*i*) 5 nm nanopolyhedra, and (*k*) 3.5 nm nuclei. HRTEM images of a single (*b*) 9 nm nanocube, (*d*) 7 nm nanocube, (*f*) 6 nm nanocube, and (*h*) 5 nm nanocube along the [100] zone axis. HRTEM images of a single (*j*) 5 nm nanopolyhedron, and (*l*) 3.5 nm nucleus along the [111] zone axis. The scale bars are 20

nm in the TEM images and 1 nm in the HRTEM images. Figures adapted with permission from: *B*, ref. 36, ACS; *C*(left), ref. 38, Elsevier; *C*(right), ref. 39, ACS.

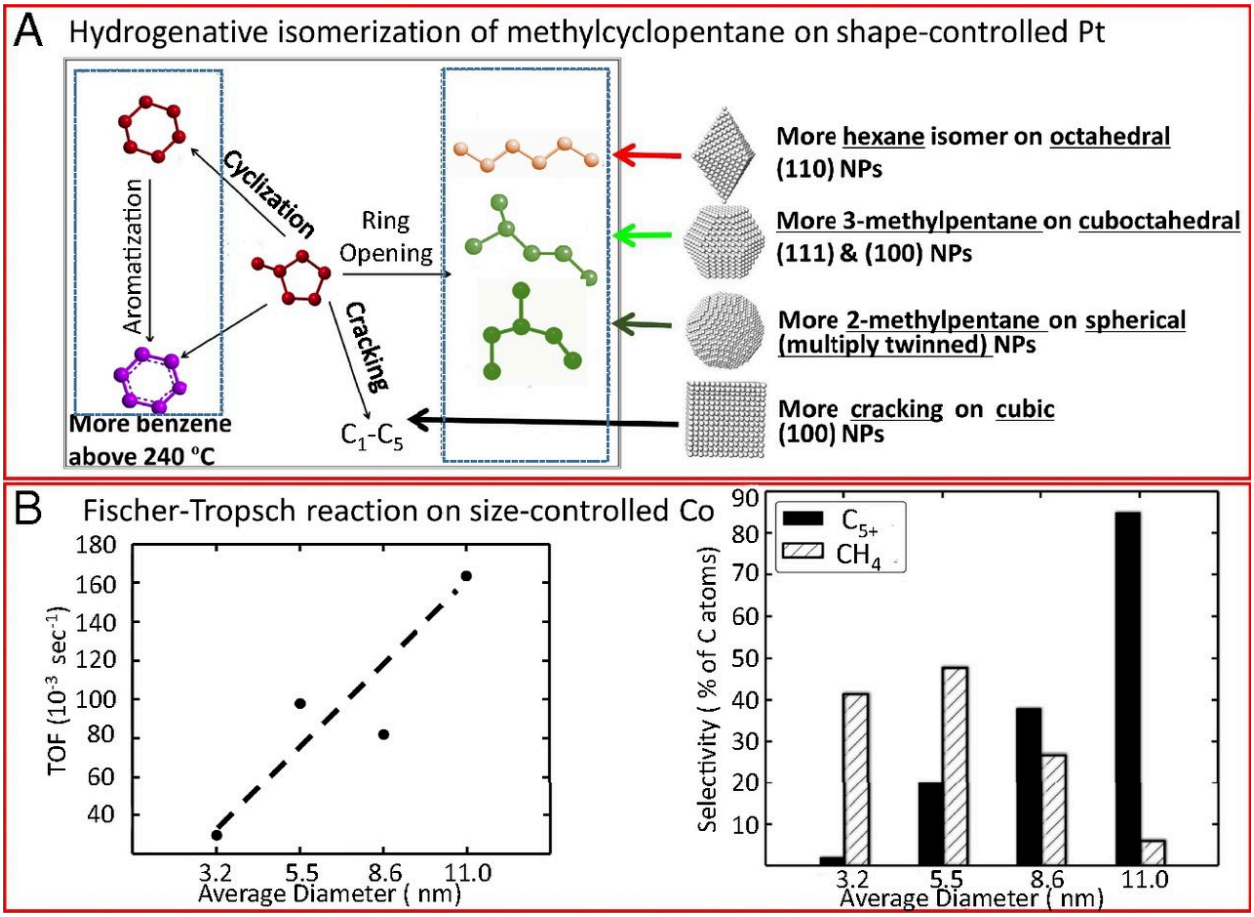

Fig. 2. Examples of shape and size dependence of nanoparticle catalysts. (*A*) Reaction pathways and possible products of methylcyclopentane hydrogenation reaction catalyzed by Pt nanoparticles with different shapes. (*B*, *Left*) CO consumption turnover frequency for the CO hydrogenation at 5 bar (H_2:CO = 2:1) for various sizes of cobalt nanoparticle catalysts supported on MCF-17. The turnover frequency (TOF) corresponds to the number of CO molecules converted in time divided by the number of cobalt atoms at the catalyst surface. (*Right*) Selectivities toward hydrocarbons with a carbon number of 5 and higher (C_{5+}) and methane selectivities (SCH_4) as a function of cobalt crystallite sizes for hydrogenation of carbon monoxide (H_2:CO = 2:1) at 5 bar and 250 °C. Both selectivities are expressed relative to the total number of carbon atoms converted. Panels adapted with permission as follows: *A*, ref. 40, Springer; *B*, ref. 41, Springer.

In our work, we found that the size and shape of metal nanoparticles control both catalytic reaction rates and selectivity. We also learned that all of these multipath reactions show size dependence in their turnover rates and selectivity.[37] It is possible to

achieve different shapes of platinum nanoparticles (Fig. 1*B*) and the size regime of platinum nanoparticles can be sharply focused in the 1.5 to 8.0 nm range (Fig. 1*C*). Such a well-defined particle size and distribution are essential to detecting the turnover rates of the hydrogenation of either benzene or toluene, as they are structure sensitive. We also observed fourfold change in turnover rates between nanoparticles of platinum in the 2–4 nm range and in the 4–6 nm range. The size and shape dependence of nanoparticles can readily be controlled by colloid science technology (Fig. 1*C*).[36,38,39] The isomerization of methylcyclopentane is much more shape dependent on the platinum nanoparticles than size dependent (Fig. 2*A*).[40] In the case of the Fischer-Tropsch CO hydrogenation reaction, the product distribution is size dependent[41] and the turnover rate increases fivefold with increasing size (Fig. 2*B*).

1.3 Characterization under reaction conditions

Previous studies only examined catalysts before use (i.e., as-made or pre-natal catalysts) and after use (i.e., spent or post-mortem catalysts) and thus could not determine how a metal nanocatalyst's structure and other properties, including composition and oxidation states, would change as a function of reaction time, temperature, and pressure.

Engineering chemical and physical properties at molecular levels is a challenging task that requires tools and strategies known as *in situ* probing to characterize catalysts in action. This *in situ* method measures macroscopic and microscopic properties simultaneously or separately under identical or similar conditions in an attempt to correlate function and structure.[31] In addition to this *in situ* approach, surface techniques — with temporal, spatial, and chemical resolutions in their respective scales of subsecond, subnanometer, and vibrational and electronic levels — are prerequisites to gaining molecular insight into catalysts' operations.[42-44] These techniques are often based on detecting outbound electrons, photons, or ions of catalysts of interest upon excitation with high-energy electrons or photons in a broad electromagnetic spectrum ranging from radio waves to IR and visible light, and to UV and X-rays. Monochromated in energies and collimated or focused in space, these probes carry electronic, vibrational, and bonding information, giving away fundamental details of the otherwise hidden components of a catalyst — pieces of a puzzle, and snapshots of a bigger picture.

Fig. 3*A* shows sum-frequency generation nonlinear optical spectroscopy,[24] which is very sensitive to the surface adsorbed species under catalytic reaction conditions.[22-24,45] Several molecular species are found[23] on the surface during ethylene hydrogenation, cyclohexene hydrogenation, and dehydrogenation (Fig. 3*B*). While some species, as well as their turnover rates, change dynamically under these conditions, others are merely spectators. The mechanistic details are revealed by sum-frequency generation under reaction conditions.

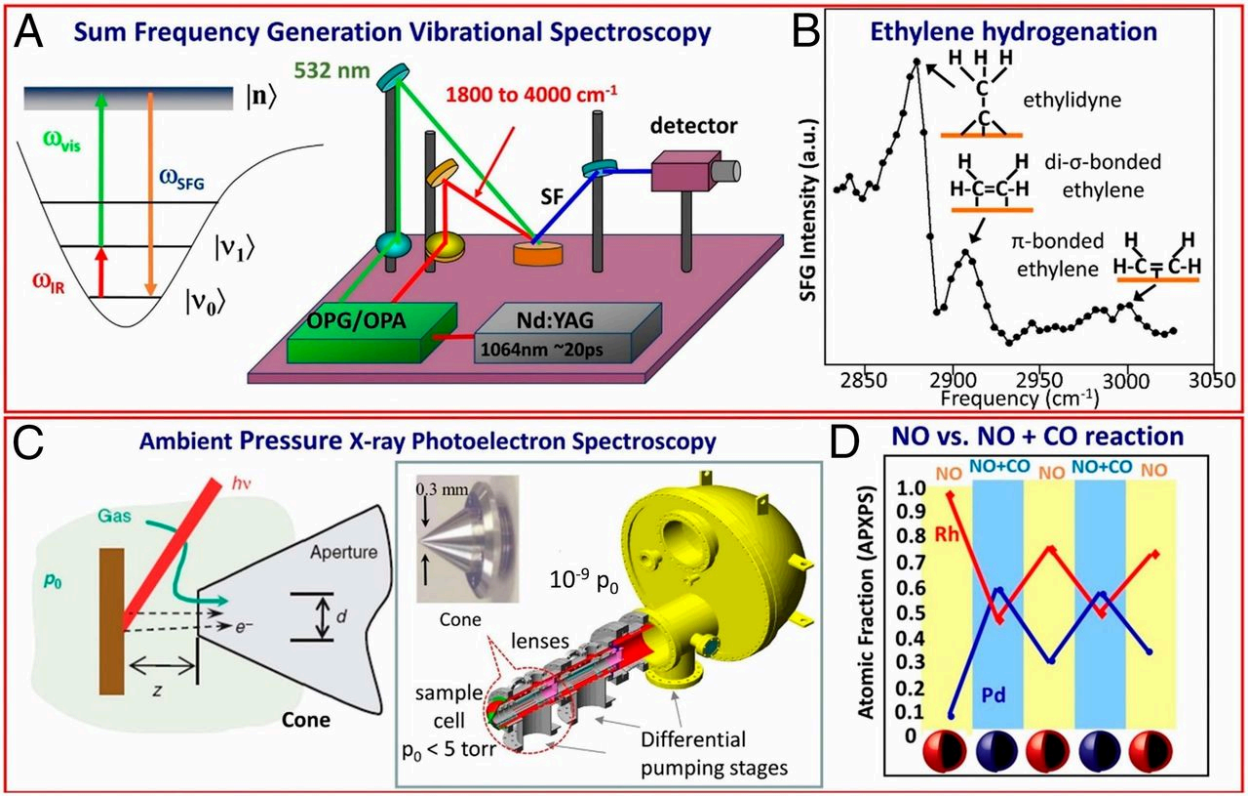

Fig. 3. In situ characterization of catalyst surfaces using sum-frequency generation (SFG) and XPS. (*A*) Schematic of a high-pressure SFG system, a vibrational spectroscopic tool for probing the adsorbed species during the catalytic reaction. (*B*) SFG spectra of adsorbed species on Pt (111) during ethylene hydrogenation under 35 torr of ethylene, 100 torr of H_2, and 625 torr of He. (*C*) Schematic of ambient pressure XPS setup at Beamline 9.3.2 of the Advanced Light Source at Lawrence Berkeley National Laboratory. (*D*) Evolution of Rh (Rh^0+Rh^{3+}) and Pd (Pd^0+Pd^{2+}) atomic fractions in the $Rh_{0.5}Pd_{0.5}$ NPs at 300 °C under oxidizing conditions (100 mtorr NO or O_2) and catalytic conditions (100 mtorr NO and 100 mtorr CO) denoted in the *x* axis. APXPS, ambient-pressure X-ray photoelectron spectroscopy; NP, nanoparticles. Panels adapted with permission as follows: *A*, ref. 25, American Chemical Society; *B*, ref. 23, Elsevier; *C*, ref. 27; *D*, ref. 8, AAAS.

Ambient pressure X-ray photoelectron spectroscopy (XPS) is shown[8,25-27] schematically in Fig. 3*C*. Bimetallic nanoparticles are shown being studied by this technique. Palladium-rhodium bimetallic nanoparticles 15 nm in size show rhodium segregation under nitric oxide (NO)-adsorption-induced oxidizing conditions. Palladium catches up with rhodium surface composition when we add a reducing gas — carbon monoxide (CO) — adsorbed on the surface.[8] The outcome of these studies is to show

that bimetallic nanoparticles undergo a surface composition change that is driven by dynamic chemical oxidizing and reducing environments (Fig. 3*D*).

A high-pressure scanning tunneling microscope (STM)[32,33] shows that the adsorbates reacting on the catalyst surface are mobile under reaction conditions. For example, when cyclohexene hydrogenation and dehydrogenation turnovers are measured under reaction conditions, the STM image is diffused. This observation indicates that the adsorbate molecules move at a faster rate than the scanning tunneling tip's surface motion of 100 Å per millisecond. However, if the surface is contaminated by carbon monoxide adsorption, cyclohexene hydrogenation and dehydrogenation reaction turnovers come to a halt, and an ordered surface structure forms, which is readily detectable by STM. We observed that not only are the adsorbed molecules mobile under catalytic reaction conditions, but the adsorbate-induced restructuring of the metal surfaces is also enhanced by high reactant pressures. The stepped platinum single crystal surfaces became clustered and rearranged at high-pressure carbon monoxide adsorption (Fig. 4*A*). This clustered formation is reversible, however: when carbon monoxide is removed from the surface by evacuation,[33] the stepped structure of the original crystal surface is reestablished.

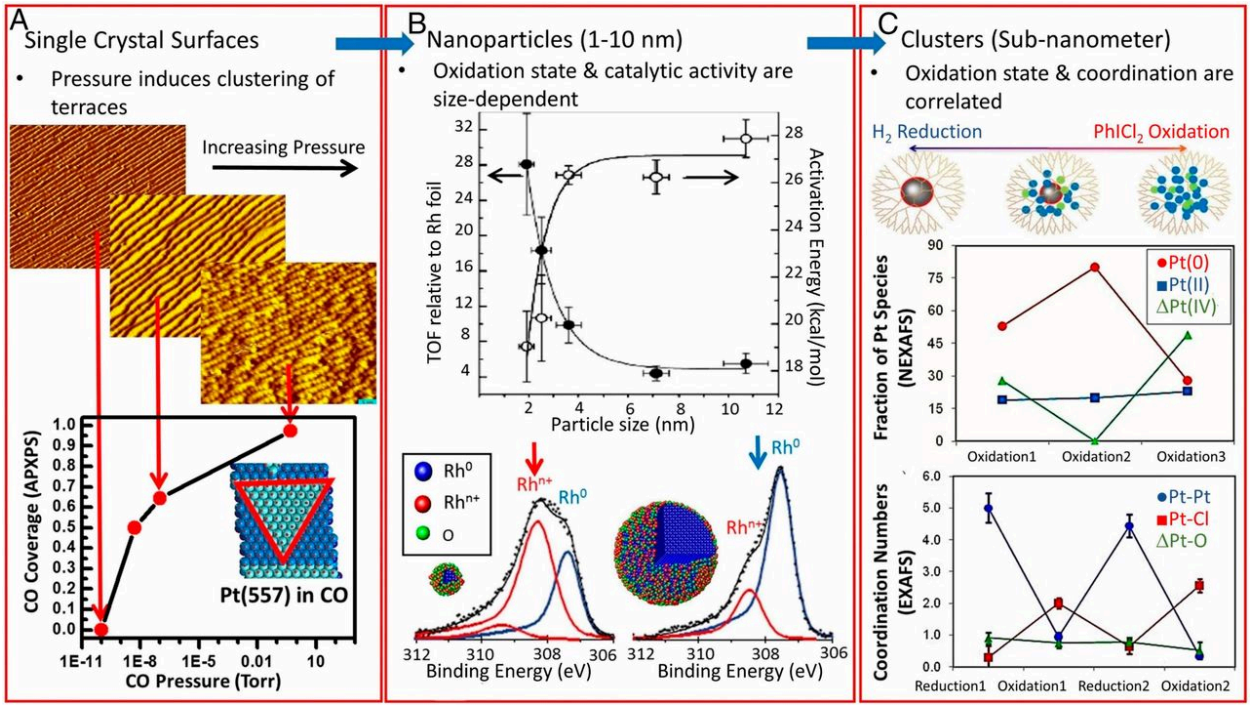

Fig. 4. In situ characterization of catalysts in decreasing sizes using STM, XPS, near-edge X-ray absorption fine structure (NEXAFS), and EXAFS. (*A*) STM images of Pt(557) in increasing pressure of CO from 1 × 10^{-10} torr to 1 torr and the corresponding CO coverage determined by APXPS. STM images are 40 nm by 50 nm in size. (*B*) Turnover frequency relative to rhodium foil at 50 torr O_2, 20 torr CO, at 200 °C, and

activation energy (150–225 °C) for CO oxidation. APXPS data show the difference of oxidation state of nanoparticles with 2 nm diameter and 11 nm diameter. (*C*, *Top*) A scheme based on the X-ray absorption spectroscopy (XAS) results, showing possible structures of the dendrimer-encapsulated Pt catalyst after reduction and oxidation treatment. The gray spheres represent the metallic Pt clusters. The surface Pt chlorides are indicated by red circles. The small blue and green species represent the Pt(II) and Pt(IV) species formed after oxidation treatment. (*Middle*) The fractions of Pt(0) and Pt(II) and Pt(IV) chloride species of the Pt catalyst derived from NEXAFS analysis. (*Bottom*) Average coordination numbers of Pt atoms in the supported Pt catalyst after a sequence of hydrogen reduction and $PhICl_2$ oxidation treatments in the toluene derived from EXAFS analysis. Panels adapted with permission as follows: *A*, ref. 33, AAAS; *B*, ref. 46; *C*, ref. 29, American Chemical Society.

1.4 Oxidation state of nanoparticles changes with decreasing size: Conversion of heterogeneous to homogeneous catalysis

When CO oxidation was studied on rhodium nanoparticle surfaces as a function of size below 2 nm, the CO oxidation rates increased by thirtyfold. Ambient pressure XPS studies[46] indicated that the higher turnover rates are due to the oxidation state of rhodium changing from metallic rhodium to rhodium^{3+} (Fig. 4*B*). Similar studies on platinum indicated that platinum nanoparticles above 1.5 nm are metallic; however, the studies also found that platinum below 1.5 nm and as low as 0.8 nm are in the 2^+ and 4^+ oxidation states.[29,47] Because very few bulk atoms are available for these nanoparticles, they become dominated by low coordination surface atoms, and as a result, their electronic structure changes. Nørskov et al.[48] have studied this process and found that the adsorption energy of oxygen on gold nanoparticles changes as a function of a decrease in size. Because there is a decrease in the gold coordination number at the adsorption sites and fewer than 55 atoms, which is slightly more than 1 nm, the gold becomes oxidized to gold 1^+ and 3^+ instead of metallic gold.

The homogeneous catalysts are usually single transition metal ions, surrounded by ligands. As a result, we tried to use these small nanoclusters, which have controlled high oxidation states to carry out homogeneous catalysis. We adsorbed the small nanoclusters on dendrimers, treelike polymers that hold these nanoparticles throughout its branches. We found that these dendrimer-encapsulated nanoparticles are excellent homogeneous catalysts, so we managed to heterogenize homogeneous catalysts by using nanoparticles composed of 40 atoms of rhodium, palladium, gold, or platinum for reactions including hydroformylation, decarbonylation, and other commonly known homogeneous catalytic reactions.[3,31,47,49-53] We demonstrated that catalytic reactivity and selectivity could be tuned by changing the dendrimer properties, in a similar fashion to ligand modification in an organometallic homogeneous catalyst.[51,53] X-ray absorption spectroscopy studies (XANES and EXAFS) showed[28-30] that the nanoparticles dispersed

to small low coordination clusters under oxidizing conditions, but reassembled to the original 1 nm particles when under reduction by reactants, products, or the dendrimers (Fig. 4*C*). This process is also reversible.

Likewise, single site homogeneous catalysts are low coordination systems comprised of ligands that control electronic structure and chemistry at the molecular level.[29,54] By controlling types and binding of ligands, a high level of selectivity (regio- and enantio-selectivity) is obtained in homogenized catalytic reactions. Capping agents used in colloidal synthesis, similar to ligands in single site organometallic complexes, can be utilized to control selectivity in heterogenized homogeneous reactions, which, as of today, remains a great challenge.

1.5 Oxide-metal interfaces as active sites for acid-base catalysis

Platinum is an excellent hydrogenation catalyst of many organic molecules, such as crotonaldehyde. When platinum nanoparticles of the same size are placed on two different oxides — silica and titania — one can see that the turnover rates and the selectivities are much higher when titania rather than silica is used as a support. The importance of the oxide support for metal catalysts to change selectivities and product distributions is well known. This phenomenon of the oxide support effect on catalytic reaction rates where the oxide alone does not carry out the same or any reaction is called positive strong metal support interaction (SMSI) in the literature.[55] It is the charge transfer ability of reducible oxide supports that acts on the performance of metal catalysts, but how does charge regulate catalytic processes?

An explanation was found by surface physics studies of hot electron emission under light illumination that was carried out by exothermic catalytic reactions on metal surfaces,[56] such as CO oxidation or hydrogen oxidation (Fig. 5*A*). The deposited energy produces high kinetic energy electrons that have a mean free path within the metal in the range of 5 to 10 nm. The chemical energy deposition in metals to produce hot electrons has been well demonstrated by Rettner and coworkers[57] using highly vibrationally excited NO molecules impinging on gold as compared to lithium fluoride surfaces. On gold, the NO molecules in the 15^{th} vibrationally excited state lose 1.5 eV energy to produce molecules in the 8^{th} vibrational state. On the other hand, the vibrationally excited NO molecules lost no energy when they scattered from lithium fluoride, which has no free electrons. The hot electron generation can be observed by using exothermic catalytic reactions on a Schottky diode on platinum and titanium oxide where the platinum is less than about 5 nm in thickness. The charge flow between the platinum and the titanium oxide allows one to determine the current flow in the battery configuration shown in Fig. 5*A*. One can detect a so-called chemicurrent, which is correlated with the turnover rate of exothermic CO oxidation or hydrogen oxidation reactions [58]. Theoretical calculations showed that the transition state in these processes involves CO_2^- or H_2O^-, which yields the chemicurrent that is proportional to the turnover

rate. In this study, acid-base catalysis is correlated with charge concentration, and not with surface area. On the other hand, covalent bond catalysis is known to be surface area dependent. These two modes of catalysis are the major ways chemistry occurs in most catalytic processes.

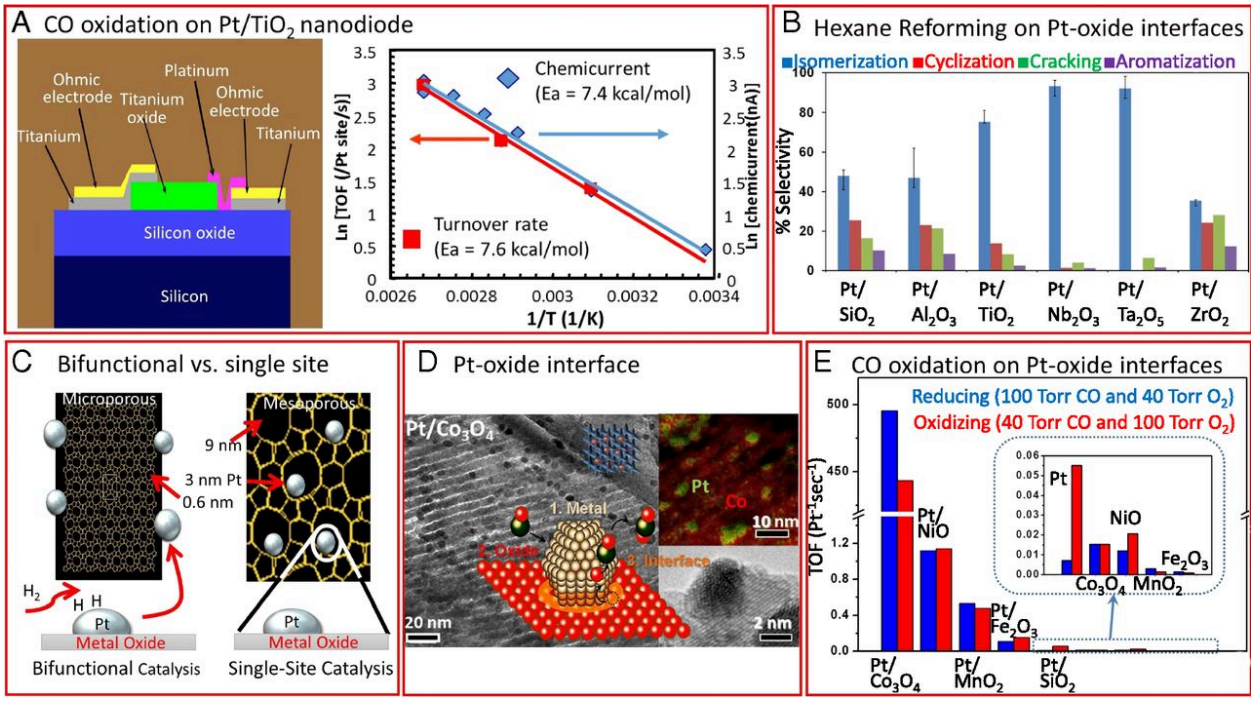

Fig. 5. Evidence for the importance of the metal oxide support on catalysis. (*A*, *Left*) Schematic of Pt/TiO_2 device. (*Right*) Arrhenius plots obtained from chemicurrent and turnover measurements on a Pt/TiO_2 diode with pressure of 6 torr of H_2 and 760 torr O_2. Both give similar activation energies, which implies that hot electron generation under hydrogen oxidation is proportional to the catalytic turnover rate. (*B*) Product distributions of *n*-hexane isomerization over 2.7 nm Pt nanoparticle catalysts supported on different kinds of oxide supports at 360 °C. (*C*) Schematics of the differences between bifunctional and single-site catalysis. (*D*, *Left*) TEM image of Pt/Co_3O_4 catalysts. (*Top Right*) Energy-dispersive spectroscopy (EDS) phase mapping of Pt/Co_3O_4 catalysts, showing the merged image of the Co K (red) and Pt L (green) lines. (*Bottom Right*) High-resolution TEM image of Pt/Co_3O_4 catalysts. (*Inset Top*) Illustration of mesoporous-oxide-supported Pt nanoparticle catalysts. (*Inset Bottom*) An illustration showing the potential reaction sites of Pt-nanoparticle-loaded oxide catalysts during CO oxidation. (*E*) Comparison of TOFs at 473 K of CO oxidation over Pt-nanoparticle-loaded oxide and pure mesoporous oxide catalysts. Panels adapted with permission as follows: *A*, *Left*, ref. 56, American Vacuum Society; *A*, *Right*, ref. 58, American Chemical Society; *B*, ref. 59, American Chemical Society; *D* and *E*, ref. 60, American Chemical Society.

When one places metal nanoparticles into a mesoporous oxide support, many oxide-metal interfaces are produced within the mesopores between the metal and the oxide. Studies have found that these oxide-metal interfaces have major effects on catalytic reactions. The isomerization of *n*-hexane on naked oxide only results in the cracking of the *n*-hexane molecules, while mesoporous oxides give rise to 100% selectivity of *n*-hexane isomers of high octane numbers[59] in the presence of platinum (Fig. 5*B*). Fig. 5 C–E show similar effects when platinum is placed on various oxide mesopores. Platinum nanoparticles produce very little CO oxidation within mesoporous silica, but when they are placed on mesoporous cobalt oxide, more than a thousand-fold increase in catalytic turnover for CO oxidation kinetics is found.

Fig. 5*C* (right) shows mesoporous transition metal oxide supported platinum nanoparticles. This is the oxide-metal interface, which produces large, strong metal support effects. There is a charge transfer between the metal and the oxide under reaction conditions. If the oxide is alone, as in the case of *n*-hexane conversion with pure oxides of niobium oxide, titanium oxide, and other oxides, only the cracking of the *n*-hexane molecules is observed. However, if the platinum is in the mesopores, a 100% selectivity to isomerization is produced, which is very high and an important factor in making high-octane gasoline.

Fig. 5*C* (left) shows platinum nanoparticles in contact with microporous oxides when the platinum nanoparticle is much larger and cannot fit into the micropores. In this case, the chemistry that occurs — known as bifunctional catalysis — is the sum total of the chemistry of platinum and the microporous oxide, which act in parallel or consecutively. In the other case, when the mesoporous transition metal oxide can accommodate the 3 nm platinum inside its mesopores, there are oxide-metal interfaces, where charge transfer and acid-base catalysis occur, which are uniquely selective in many circumstances. Similar results are seen when CO oxidation is carried out on platinum supported by silica or another transition metal oxide.[60] The turnover rate on silica is small, equal to pure platinum turnover; however, when cobalt oxide is the mesoporous support, the turnover rate is amplified by a thousand fold (Fig. 5*E*). This finding is indeed a major increase in catalytic activity.

1.6 Hybrid systems: outlook

It is clear that we can heterogenize homogeneous catalysts. However, enzymes[12-16] are also very important catalytic systems, and recent studies have focused on how to synthesize pure enzymes as well as on how to look for similarities between enzymes and all three catalytic systems on the molecular scale. For example, it is known that when enzymes are immobilized on a surface they gain the reusability and ease of separation seen in heterogeneous catalysts, as well as in some cases becoming more stable to wider pH and temperature ranges.[61-63] It is planned to advance previous work by immobilizing enzymes on a solid surface and studying the enzyme-solid interface at

the molecular level, and to develop a molecular understanding of all three types of catalysts under similar conditions of reactions and chemical environments.

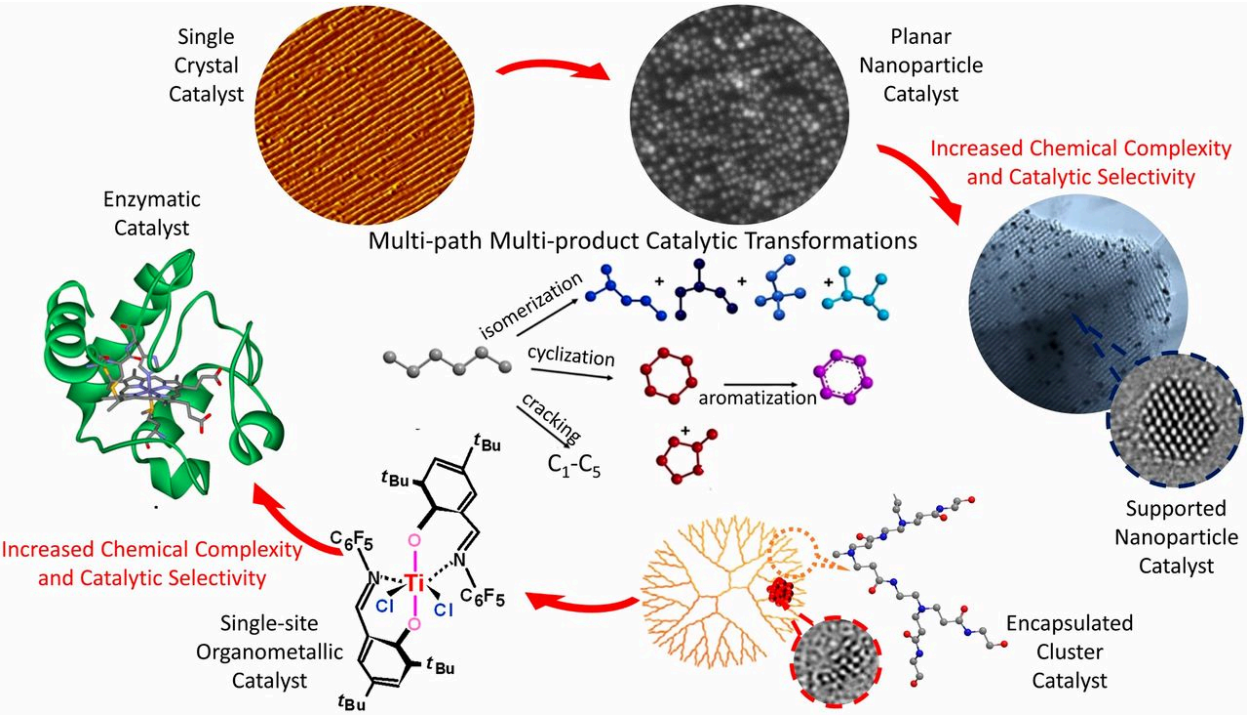

Fig. 6. Schematics showing the evolution of catalyst complexity leading to increased catalytic selectivity for multipath and multiproduct catalytic transformations. Enzymatic catalyst adapted with permission from ref. 14, AAAS.

In our attempt to focus on the chemical correlations between the three catalysis groups — heterogeneous, homogeneous, and enzymatic — the future looks very promising for molecular catalysis science studies. Catalysis of homogeneous, heterogeneous, or enzymatic origin alike involve nano sized materials. These nanocatalysts are comprised of inorganic and/or organic components. Charge, coordination, interatomic distance, bonding, and orientation of catalytically active atoms are molecular factors shared by all three field of catalysis. By controlling the governing catalytic components and molecular factors, catalytic processes of a multichannel and multiproduct nature could be run in all three catalytic platforms to create unique end-products. Fig. 6 illustrates the promise of a molecularly unified catalytic scheme of the future.

1.7 References

1. Silvera Batista, C. A.; Larson, R. G.; Kotov, N. A. Nonadditivity of nanoparticle interactions. *Science* **2015**, *350*.

2. Yin, Y.; Alivisatos, A. P. Colloidal nanocrystal synthesis and the organic-inorganic interface. *Nature* **2005**, *437*, 664-670.
3. Crooks, R. M.; Zhao, M.; Sun, L.; Chechik, V.; Yeung, L. K. Dendrimer-Encapsulated Metal Nanoparticles: Synthesis, Characterization, and Applications to Catalysis. *Acc. Chem. Res.* **2001**, *34*, 181-190.
4. Li, H.; Eddaoudi, M.; O'Keeffe, M.; Yaghi, O. M. Design and synthesis of an exceptionally stable and highly porous metal-organic framework. *Nature* **1999**, *402*, 276-279.
5. Schrinner, M.; Ballauff, M.; Talmon, Y.; Kauffmann, Y.; Thun, J.; Möller, M.; Breu, J. Single Nanocrystals of Platinum Prepared by Partial Dissolution of Au-Pt Nanoalloys. *Science* **2009**, *323*, 617-620.
6. Lee, I.; Morales, R.; Albiter, M. A.; Zaera, F. Synthesis of heterogeneous catalysts with well shaped platinum particles to control reaction selectivity. *Proc. Natl. Acad. Sci. U.S.A.* **2008**, *105*, 15241-15246.
7. Sun, Y.; Xia, Y. Shape-Controlled Synthesis of Gold and Silver Nanoparticles. *Science* **2002**, *298*, 2176-2179.
8. Tao, F.; Grass, M. E.; Zhang, Y.; Butcher, D. R.; Renzas, J. R.; Liu, Z.; Chung, J. Y.; Mun, B. S.; Salmeron, M.; Somorjai, G. A. Reaction-Driven Restructuring of Rh-Pd and Pt-Pd Core-Shell Nanoparticles. *Science* **2008**, *322*, 932-934.
9. Stamenkovic, V. R.; Fowler, B.; Mun, B. S.; Wang, G.; Ross, P. N.; Lucas, C. A.; Marković, N. M. Improved Oxygen Reduction Activity on Pt3Ni(111) via Increased Surface Site Availability. *Science* **2007**, *315*, 493-497.
10. Yang, P.; Zhao, D.; Margolese, D. I.; Chmelka, B. F.; Stucky, G. D. Generalized syntheses of large-pore mesoporous metal oxides with semicrystalline frameworks. *Nature* **1998**, *396*, 152-155.
11. Zhao, D.; Feng, J.; Huo, Q.; Melosh, N.; Fredrickson, G. H.; Chmelka, B. F.; Stucky, G. D. Triblock Copolymer Syntheses of Mesoporous Silica with Periodic 50 to 300 Angstrom Pores. *Science* **1998**, *279*, 548-552.
12. Glowacki, D. R.; Harvey, J. N.; Mulholland, A. J. Taking Ockham's razor to enzyme dynamics and catalysis. *Nat. Chem.* **2012**, *4*, 169-176.
13. Hay, S.; Scrutton, N. S. Good vibrations in enzyme-catalysed reactions. *Nat. Chem.* **2012**, *4*, 161-168.
14. Bhabha, G.; Lee, J.; Ekiert, D. C.; Gam, J.; Wilson, I. A.; Dyson, H. J.; Benkovic, S. J.; Wright, P. E. A Dynamic Knockout Reveals That Conformational Fluctuations Influence the Chemical Step of Enzyme Catalysis. *Science* **2011**, *332*, 234-238.
15. Boehr, D. D.; McElheny, D.; Dyson, H. J.; Wright, P. E. The Dynamic Energy Landscape of Dihydrofolate Reductase Catalysis. *Science* **2006**, *313*, 1638-1642.
16. Nureki, O.; Vassylyev, D. G.; Tateno, M.; Shimada, A.; Nakama, T.; Fukai, S.; Konno, M.; Hendrickson, T. L.; Schimmel, P.; Yokoyama, S. Enzyme Structure with Two Catalytic Sites for Double-Sieve Selection of Substrate. *Science* **1998**, *280*, 578-582.

17. Liao, H.-G.; Zherebetskyy, D.; Xin, H.; Czarnik, C.; Ercius, P.; Elmlund, H.; Pan, M.; Wang, L.-W.; Zheng, H. Facet development during platinum nanocube growth. *Science* **2014**, *345*, 916-919.
18. de Oteyza, D. G.; Gorman, P.; Chen, Y.-C.; Wickenburg, S.; Riss, A.; Mowbray, D. J.; Etkin, G.; Pedramrazi, Z.; Tsai, H.-Z.; Rubio, A.; Crommie, M. F.; Fischer, F. R. Direct Imaging of Covalent Bond Structure in Single-Molecule Chemical Reactions. *Science* **2013**, *340*, 1434-1437.
19. Bao, W.; Melli, M.; Caselli, N.; Riboli, F.; Wiersma, D. S.; Staffaroni, M.; Choo, H.; Ogletree, D. F.; Aloni, S.; Bokor, J.; Cabrini, S.; Intonti, F.; Salmeron, M. B.; Yablonovitch, E.; Schuck, P. J.; Weber-Bargioni, A. Mapping Local Charge Recombination Heterogeneity by Multidimensional Nanospectroscopic Imaging. *Science* **2012**, *338*, 1317-1321.
20. Choi, J. S.; Kim, J.-S.; Byun, I.-S.; Lee, D. H.; Lee, M. J.; Park, B. H.; Lee, C.; Yoon, D.; Cheong, H.; Lee, K. H.; Son, Y.-W.; Park, J. Y.; Salmeron, M. Friction Anisotropy–Driven Domain Imaging on Exfoliated Monolayer Graphene. *Science* **2011**, *333*, 607-610.
21. Umstadter, D.; Chen, S.-Y.; Maksimchuk, A.; Mourou, G.; Wagner, R. Nonlinear Optics in Relativistic Plasmas and Laser Wake Field Acceleration of Electrons. *Science* **1996**, *273*, 472-475.
22. Holinga, G. J.; York, R. L.; Onorato, R. M.; Thompson, C. M.; Webb, N. E.; Yoon, A. P.; Somorjai, G. A. An SFG Study of Interfacial Amino Acids at the Hydrophilic SiO2 and Hydrophobic Deuterated Polystyrene Surfaces. *J. Am. Chem. Soc.* **2011**, *133*, 6243-6253.
23. McCrea, K. R.; Somorjai, G. A. SFG-surface vibrational spectroscopy studies of structure sensitivity and insensitivity in catalytic reactions: cyclohexene dehydrogenation and ethylene hydrogenation on Pt (1 1 1) and Pt (1 0 0) crystal surfaces. *J. Mol. Catal. A: Chemical* **2000**, *163*, 43-53.
24. Shen, Y. Surface properties probed by second-harmonic and sum-frequency generation. *Nature* **1989**, *337*, 519-525.
25. Alayoglu, S.; Krier, J. M.; Michalak, W. D.; Zhu, Z.; Gross, E.; Somorjai, G. A. In Situ Surface and Reaction Probe Studies with Model Nanoparticle Catalysts. *ACS Catal.* **2012**, *2*, 2250-2258.
26. Salmeron, M.; Schlögl, R. Ambient pressure photoelectron spectroscopy: A new tool for surface science and nanotechnology. *Surf. Sci. Rep.* **2008**, *63*, 169-199.
27. Bluhm, H.; Hävecker, M.; Knop-Gericke, A.; Kiskinova, M.; Schlögl, R.; Salmeron, M. In Situ X-Ray Photoelectron Spectroscopy Studies of Gas-Solid Interfaces at Near-Ambient Conditions. *MRS Bulletin* **2007**, *32*, 1022-1030.
28. Velasco-Velez, J.-J.; Wu, C. H.; Pascal, T. A.; Wan, L. F.; Guo, J.; Prendergast, D.; Salmeron, M. The structure of interfacial water on gold electrodes studied by x-ray absorption spectroscopy. *Science* **2014**, *346*, 831-834.

29. Li, Y.; Liu, J. H.-C.; Witham, C. A.; Huang, W.; Marcus, M. A.; Fakra, S. C.; Alayoglu, P.; Zhu, Z.; Thompson, C. M.; Arjun, A.; Lee, K.; Gross, E.; Toste, F. D.; Somorjai, G. A. A Pt-Cluster-Based Heterogeneous Catalyst for Homogeneous Catalytic Reactions: X-ray Absorption Spectroscopy and Reaction Kinetic Studies of Their Activity and Stability against Leaching. *J. Am. Chem. Soc.* **2011**, *133*, 13527-13533.
30. Jiao, F.; Frei, H. Nanostructured Cobalt Oxide Clusters in Mesoporous Silica as Efficient Oxygen-Evolving Catalysts. *Angew. Chem. Int. Ed* **2009**, *48*, 1841-1844.
31. Gross, E.; Shu, X.-Z.; Alayoglu, S.; Bechtel, H. A.; Martin, M. C.; Toste, F. D.; Somorjai, G. A. In Situ IR and X-ray High Spatial-Resolution Microspectroscopy Measurements of Multistep Organic Transformation in Flow Microreactor Catalyzed by Au Nanoclusters. *J. Am. Chem. Soc.* **2014**, *136*, 3624-3629.
32. Zhu, Z.; Melaet, G.; Axnanda, S.; Alayoglu, S.; Liu, Z.; Salmeron, M.; Somorjai, G. A. Structure and Chemical State of the Pt(557) Surface during Hydrogen Oxidation Reaction Studied by in Situ Scanning Tunneling Microscopy and X-ray Photoelectron Spectroscopy. *J. Am. Chem. Soc.* **2013**, *135*, 12560-12563.
33. Tao, F.; Dag, S.; Wang, L.-W.; Liu, Z.; Butcher, D. R.; Bluhm, H.; Salmeron, M.; Somorjai, G. A. Break-Up of Stepped Platinum Catalyst Surfaces by High CO Coverage. *Science* **2010**, *327*, 850-853.
34. Somorjai, G. A.; Li, Y.: *Introduction to Surface Chemistry and Catalysis, 2nd Edition*; Wiley, 2010.
35. Franklin, A. D. Nanomaterials in transistors: From high-performance to thin-film applications. *Science* **2015**, *349*.
36. Song, H.; Kim, F.; Connor, S.; Somorjai, G. A.; Yang, P. Pt Nanocrystals: Shape Control and Langmuir−Blodgett Monolayer Formation. *J. Phys. Chem. B* **2005**, *109*, 188-193.
37. Lee, I.; Delbecq, F.; Morales, R.; Albiter, M. A.; Zaera, F. Tuning selectivity in catalysis by controlling particle shape. *Nat. Mater.* **2009**, *8*, 132-138.
38. Pushkarev, V. V.; An, K.; Alayoglu, S.; Beaumont, S. K.; Somorjai, G. A. Hydrogenation of benzene and toluene over size controlled Pt/SBA-15 catalysts: Elucidation of the Pt particle size effect on reaction kinetics. *J. Catal.* **2012**, *292*, 64-72.
39. Tsung, C.-K.; Kuhn, J. N.; Huang, W.; Aliaga, C.; Hung, L.-I.; Somorjai, G. A.; Yang, P. Sub-10 nm Platinum Nanocrystals with Size and Shape Control: Catalytic Study for Ethylene and Pyrrole Hydrogenation. *J. Am. Chem. Soc.* **2009**, *131*, 5816-5822.
40. Alayoglu, S.; Aliaga, C.; Sprung, C.; Somorjai, G. A. Size and Shape Dependence on Pt Nanoparticles for the Methylcyclopentane/Hydrogen Ring Opening/Ring Enlargement Reaction. *Catal. Lett.* **2011**, *141*, 914-924.
41. Melaet, G.; Lindeman, A.; Somorjai, G. Cobalt Particle Size Effects in the Fischer–Tropsch Synthesis and in the Hydrogenation of CO2 Studied with Nanoparticle Model Catalysts on Silica. *Top. Catal.* **2014**, *57*, 500-507.

42. Buurmans, I. L. C.; Weckhuysen, B. M. Heterogeneities of individual catalyst particles in space and time as monitored by spectroscopy. *Nat. Chem.* **2012**, *4*, 873-886.
43. van Schrojenstein Lantman, E. M.; Deckert-Gaudig, T.; Mank, A. J. G.; Deckert, V.; Weckhuysen, B. M. Catalytic processes monitored at the nanoscale with tip-enhanced Raman spectroscopy. *Nat. Nano* **2012**, *7*, 583-586.
44. de Smit, E.; Swart, I.; Creemer, J. F.; Hoveling, G. H.; Gilles, M. K.; Tyliszczak, T.; Kooyman, P. J.; Zandbergen, H. W.; Morin, C.; Weckhuysen, B. M.; de Groot, F. M. F. Nanoscale chemical imaging of a working catalyst by scanning transmission X-ray microscopy. *Nature* **2008**, *456*, 222-225.
45. Somorjai, G. A.; Frei, H.; Park, J. Y. Advancing the Frontiers in Nanocatalysis, Biointerfaces, and Renewable Energy Conversion by Innovations of Surface Techniques. *J. Am. Chem. Soc.* **2009**, *131*, 16589-16605.
46. Grass, M. E.; Zhang, Y.; Butcher, D. R.; Park, J. Y.; Li, Y.; Bluhm, H.; Bratlie, K. M.; Zhang, T.; Somorjai, G. A. A Reactive Oxide Overlayer on Rhodium Nanoparticles during CO Oxidation and Its Size Dependence Studied by In Situ Ambient-Pressure X-ray Photoelectron Spectroscopy. *Angew. Chem. Int. Ed* **2008**, *47*, 8893-8896.
47. Crooks, R. M.; Zhao, M. Dendrimer-Encapsulated Pt Nanoparticles: Synthesis, Characterization, and Applications to Catalysis. *Adv. Mater.* **1999**, *11*, 217-220.
48. Kleis, J.; Greeley, J.; Romero, N. A.; Morozov, V. A.; Falsig, H.; Larsen, A. H.; Lu, J.; Mortensen, J. J.; Dułak, M.; Thygesen, K. S.; Nørskov, J. K.; Jacobsen, K. W. Finite Size Effects in Chemical Bonding: From Small Clusters to Solids. *Catal. Lett.* **2011**, *141*, 1067-1071.
49. Huang, W.; Kuhn, J. N.; Tsung, C.-K.; Zhang, Y.; Habas, S. E.; Yang, P.; Somorjai, G. A. Dendrimer Templated Synthesis of One Nanometer Rh and Pt Particles Supported on Mesoporous Silica: Catalytic Activity for Ethylene and Pyrrole Hydrogenation. *Nano Lett.* **2008**, *8*, 2027-2034.
50. Witham, C. A.; Huang, W.; Tsung, C.-K.; Kuhn, J. N.; Somorjai, G. A.; Toste, F. D. Converting homogeneous to heterogeneous in electrophilic catalysis using monodisperse metal nanoparticles. *Nat. Chem.* **2010**, *2*, 36-41.
51. Gross, E.; Liu, J. H.-C.; Toste, F. D.; Somorjai, G. A. Control of selectivity in heterogeneous catalysis by tuning nanoparticle properties and reactor residence time. *Nat. Chem.* **2012**, *4*, 947-952.
52. Huang, W.; Liu, J. H.-C.; Alayoglu, P.; Li, Y.; Witham, C. A.; Tsung, C.-K.; Toste, F. D.; Somorjai, G. A. Highly Active Heterogeneous Palladium Nanoparticle Catalysts for Homogeneous Electrophilic Reactions in Solution and the Utilization of a Continuous Flow Reactor. *J. Am. Chem. Soc.* **2010**, *132*, 16771-16773.
53. Gross, E.; Liu, J. H.; Alayoglu, S.; Marcus, M. A.; Fakra, S. C.; Toste, F. D.; Somorjai, G. A. Asymmetric Catalysis at the Mesoscale: Gold Nanoclusters Embedded in Chiral Self-Assembled Monolayer as Heterogeneous Catalyst for Asymmetric Reactions. *J. Am. Chem. Soc.* **2013**, *135*, 3881-3886.

54. Oliver-Meseguer, J.; Cabrero-Antonino, J. R.; Domínguez, I.; Leyva-Pérez, A.; Corma, A. Small Gold Clusters Formed in Solution Give Reaction Turnover Numbers of 107 at Room Temperature. *Science* **2012**, *338*, 1452-1455.
55. Tauster, S. J.; Fung, S. C.; Baker, R. T. K.; Horsley, J. A. Strong Interactions in Supported-Metal Catalysts. *Science* **1981**, *211*, 1121-1125.
56. Park, J. Y.; Somorjai, G. A. Energy conversion from catalytic reaction to hot electron current with metal-semiconductor Schottky nanodiodes. *J. Vac. Sci. Technol. B* **2006**, *24*, 1967-1971.
57. Huang, Y.; Rettner, C. T.; Auerbach, D. J.; Wodtke, A. M. Vibrational Promotion of Electron Transfer. *Science* **2000**, *290*, 111-114.
58. Hervier, A.; Renzas, J. R.; Park, J. Y.; Somorjai, G. A. Hydrogen Oxidation-Driven Hot Electron Flow Detected by Catalytic Nanodiodes. *Nano Lett.* **2009**, *9*, 3930-3933.
59. An, K.; Alayoglu, S.; Musselwhite, N.; Na, K.; Somorjai, G. A. Designed Catalysts from Pt Nanoparticles Supported on Macroporous Oxides for Selective Isomerization of n-Hexane. *J. Am. Chem. Soc.* **2014**, *136*, 6830-6833.
60. An, K.; Alayoglu, S.; Musselwhite, N.; Plamthottam, S.; Melaet, G.; Lindeman, A. E.; Somorjai, G. A. Enhanced CO Oxidation Rates at the Interface of Mesoporous Oxides and Pt Nanoparticles. *J. Am. Chem. Soc.* **2013**, *135*, 16689-16696.
61. Torres-Salas, P.; del Monte-Martinez, A.; Cutiño-Avila, B.; Rodriguez-Colinas, B.; Alcalde, M.; Ballesteros, A. O.; Plou, F. J. Immobilized Biocatalysts: Novel Approaches and Tools for Binding Enzymes to Supports. *Adv. Mater.* **2011**, *23*, 5275-5282.
62. Matosevic, S.; Szita, N.; Baganz, F. Fundamentals and applications of immobilized microfluidic enzymatic reactors. *J. Chem. Technol. Biotechnol.* **2011**, *86*, 325-334.
63. Roessl, U.; Nahálka, J.; Nidetzky, B. Carrier-free immobilized enzymes for biocatalysis. *Biotechnol. Lett.* **2009**, *32*, 341-350.

Chapter 2 - Experimental Section

Abstract

In this chapter, an overview of the variety of experimental techniques utilized in this dissertation will be provided. First, the synthetic chemistry methods used to produce nanoclusters, nanoparticles, and mesoporous supports are discussed. Characterization includes transmission electron microscopy (TEM), X-ray photoelectron spectroscopy (XPS), inductively coupled plasma optical emission spectrometry (ICP-OES), and N_2 physisorption, to investigate the synthesized catalyst's morphology, chemical composition, and surface structures.

2.1 Introduction

The essential components of efficient catalysis can be controlled synthetically, investigated mechanically, and optimized to obtain the maximum catalytic performance, especially turnover rate and product selectivity. The versatile characterization techniques reveal the chemical reasons of unusual catalytic activity and/or selectivity, which in return guide the fabrication of next-generation catalysts focusing on these key chemical features with the aid of nanotechnology. This chapter provides the synthetic and characterization techniques used in this dissertation that grant insight into the workings of a catalytic system.

2.2 Synthetic techniques

2.2.1 Synthesis of dendrimer-encapsulated metal clusters

The synthesis protocols of Rh_n/G4OH (n=15~60), Pd_{40}/G4OH, and Au_{40}/G4OH were reported in our previous works.[1-3] Fourth-generation polyamidoamine (PAMAM) dendrimers with -OH terminal groups (G4OH) were purchased from Dendritech Inc. as 9.75 wt % water solution, which was diluted to a dendrimer stock solution (250 mM) by adding water. For Rh NPs, 6 mL of this stock solution of G4OH was diluted to 52 mL, and mixed with 15–50 mole equivalents of an aqueous solution of 0.01 M $RhCl_3$ in a 100 mL flask. The flask was purged with Ar for 30 min, tightly sealed and left undisturbed for 18 h for complexation. Then a 20-fold excess of iced-cold freshly prepared 0.5 M $NaBH_4$ was injected dropwise into the flask with vigorous magnetic stirring. The solution was stirred for 2 h, followed by dialysis against 2 L of deionized water in cellulose dialysis sacks with a molecular weight cutoff of 12,000. Dialysis occurred over 24 h with the water changed four times. For the synthesis of Pd and Au NPs, K_2PdCl_4 and $HAuCl_4$ were used, respectively. Reduction of $HAuCl_4$ required a solution of 0.5 M $NaBH_4$ and 0.15 M NaOH. Rh_{40}/G3OH and Rh_{40}/G6OH were synthesized with third-generation and sixth generation PAMAM dendrimers, respectively, in the same way. Rh_{40}/G4NH_2 and Rh_{40}/G4SA were synthesized with fourth-generation PAMAM dendrimers with amine and succinamic acid terminal groups, respectively. Synthesis of Rh_{40}/G4NH2 required additional steps: adjusting dendrimer solution pH to 3 by adding HCl before mixing with $RhCl_3$, and to 8 after adding $NaBH_4$.[4]

2.2.2 Colloidal synthesis of metal nanoparticles

The procedures were reported by our group.[5,6] For 2 nm Rh NPs, 40.0 mg of $Rh(acac)_3$, 88.2 mg of sodium citrate, and 111 mg of poly(vinylpyrrolidone) (PVP, 55K) were added to 20 mL of 1,4-butanediol in a 50 mL three-necked flask at room temperature. The mixture was heated to 140 °C in a Glas-Col electromantle (60 W; 50 mL) with a Cole-Parmer temperature controller (Diqi-sense), and was evacuated at this temperature for 20 min under magnetic stirring. The flask was then heated to 220 °C, at

a rate of 10 °C min^{-1}, and maintained at this temperature (±2 °C) for 2 h under Ar. When the reaction was complete, an excess of acetone was poured into the solution at room temperature to form a cloudy black suspension, which was separated by centrifugation at 4200 rpm for 6 min. The black product was collected by discarding the colorless supernatant. The precipitated Rh nanocrystals were washed with acetone once and then redispersed in ethanol. 6.0 nm Rh nanoparticles were synthesized similarly using 40.0 mg of $Rh(acac)_3$, 7.35 mg of sodium citrate, and 111 mg of PVP. 7.1 nm Rh nanoparticles were synthesized similarly using 10.0 mg of $Rh(acac)_3$ and 27.75 mg of PVP without sodium citrate.

2.2.3 Synthesis of gold nanospheres and gold nanorods

The seeded-growth synthesis of Au nanospheres with 40 nm diameter was modified from a published procedure.[7] In a typical synthesis, 9.75 mL of 0.1 M CTAB solution was mixed with 0.25 mL of 0.01 M $HAuCl_4$ solution in a centrifuge tube. 0.60 mL of 0.01 M freshly-prepared, ice-cold solution of $NaBH_4$ was added into the tube, and immediately, the tube was capped and vigorously shaken for 1 minute. The seed solution was kept under gentle stirring for 2 h at room temperature before use. The seed solution was diluted by 10 times. To grow nano-octahedra, 19 mL of water, 4 mL of 0.1 M CTAB, 0.40 mL of 0.01 M of $HAuCl_4$, 1.5 mL of 0.1 M AA, and 120 μL of the diluted seed solution were added into a 50 mL centrifuge tube, and mixed by gentle inversion for 10 s, then then left undisturbed overnight at room temperature. Into the resultant Au nano-octahedron solution, 1.0 mL of 0.01 M $HAuCl_4$ was added, and the solution was kept in 80 °C for 2 h. The as-prepared Au nanospheres solution was centrifuged at 10000 rpm for 10 min. The precipitate was redispersed in the same amount of water for further use. To grow Au nanospheres with 56 nm diameter, everything else was the same except 20 μL of the diluted seed solution was used, and instead of heated with $HAuCl_4$ at 80 °C, the Au nano-octahedron solution was heated with 1.0 mL of H_2O_2 solution at 33 °C for 16 h.

The seeded-growth synthesis of Au nanospheres with 20 nm diameter was adapted from a published procedure.[8] The seed solution was prepared in the same procedure as described above. To grow nanospheres, 2 mL of 0.2 M cetrimonium chloride, 1.5 mL of 0.1 M AA, 10 μL of Au seed were mixed, followed by a one-shot injection of 2 mL of 0.5 mM $HAuCl_4$. The solution was left undisturbed for 15 min at room temperature. The as-prepared Au nanospheres solution was centrifuged at 12000 rpm for 10 min. The precipitate was redispersed in the same amount of water for further use.

The synthesis of Au nanorods with different aspect ratios was modified from a published procedure.[9] The seed solution was prepared in the same way as the seed solution for Au nanospheres. To grow Au nanorods, 40 mL of 0.1 M CTAB, 2.0 mL of 0.01 M $HAuCl_4$, 0.4 mL of 0.01 M $AgNO_3$, 0.8 mL of 1.0 M HCl, 0.32 mL of 0.1 M AA, and 96 μL of the seed solution were added into a 50 mL centrifuge tube. The solution was

mixed by gentle inversion for 10 s and left undisturbed at a 33 °C water bathovernight before use. Into the resultant Au nanorod solution, 1.0 mL of 0.01 M $HAuCl_4$ was added, and the solution was kept in 80 °C for various time duration for nanorods with different aspect ratios. The as-prepared Au rods solution was centrifuged at 10000 rpm for 10 min. The precipitate was redispersed in the same amount of water for further use.

2.2.4 Synthesis of mesoporous silica

Synthesis of mesoporous SBA-15 silica with different pore profiles.

The method developed by Zhao et al was followed.[10] For MP-SBA-15, 4.0 g of Pluronic P123, 30 g of deionized water, and 120 g of 2 M HCl were stirred at 35 °C for 1 h. 8.5 g of tetraethylorthosilicate was added to the solution and allowed to stir for 20 h. The mixture was sealed and aged at 80 °C for 24 h. The mixture was filtered to give a white powder, which was further purified by washing three times with ethanol and deionized water. This purified product was dried in air at room temperature, and then put into a calcination oven that ramped up to 500 °C in 8 h and kept for 6 h. For SP-SBA-15, the 80 °C aging step was skipped, and for LP-SBA-15, the sample was aged at 100 °C for 24 h.

Synthesis of H^+-Al-SBA-15.

The procedure was reported elsewhere.[11] 0.5 g of SBA-15 was combined with 50 mL of dry ethanol containing 0.11 g of $AlCl_3$ with magnetic stirring at room temperature for 12 h. The solid material was then filtered, washed with dry ethanol, and dried at room temperature in air, and calcined in static air at 550 °C for 5 h.

2.2.5 Synthesis of mesoporous zeolites

Mesoporous BEA zeolite and mesoporous silica MCF-17 were synthesized by following the literature reported elsewhere.[12]

For mesoporous BEA zeolite, a cyclic diammonium-type organic molecule was used as the zeolite structure-directing agent (SDA), which was prepared by organic reaction following the literature.[12] In a typical zeolite synthesis, sodium-silicate was used as the silica source and $Al_2(SO_4)_3 \cdot 18H_2O$ was used as the alumina source. The silica and the alumina sources were dissolved in water with NaOH and organic SDA to give molar composition of $30Na_2O$ / $5Al_2O_3$ / $100SiO_2$ / 10SDA / $15H_2SO_4$ / $6000H_2O$. After aging for 1 h at room temperature, the mixture was transferred to a Teflon-coated stainless-steel autoclave and heated at 170 ^oC for 1 d in an oil bath on the magnetic stirrer equipped with heating system. The resultant precipitate was collected by filtration and washed with distilled water three times to remove residual chemicals. Then, the sample was dried in an oven at 120 ^oC and subsequently calcined at 550 ^oC in an air for 4 h to remove organic SDA. The calcined mesoporous BEA zeolite was further ion-exchanged to H^+-form to introduce acidic function on the aluminosilicate framework. In a typical ion-exchange process, the calcined zeolite samples were first ion-exchanged to NH_4^+-form with a 1 M NH_4NO_3 aqueous solution three separate times (NH_4NO_3/Al =

10), and then, subsequently converted to the H^+-form through calcination in air at 550 ^oC for 4 h.

For postdealumation of mesoporous BEA zeolite, 0.5 g of H^+-exchanged mesoporous BEA zeolite was diluted in 20 mL of 1–2 M HCl solutions, and heated for 30–90 min under reflux condition. After treatment, the zeolite was collected by filtration, washed with distilled water three times, and dried in an oven at 120 °C. The resultant mesoporous BEA zeolite was denoted as BEA-*x*, where *x* is the content (%) of Al in the zeolite framework.

2.3 Characterization

2.3.1 Transmission electron microscopy

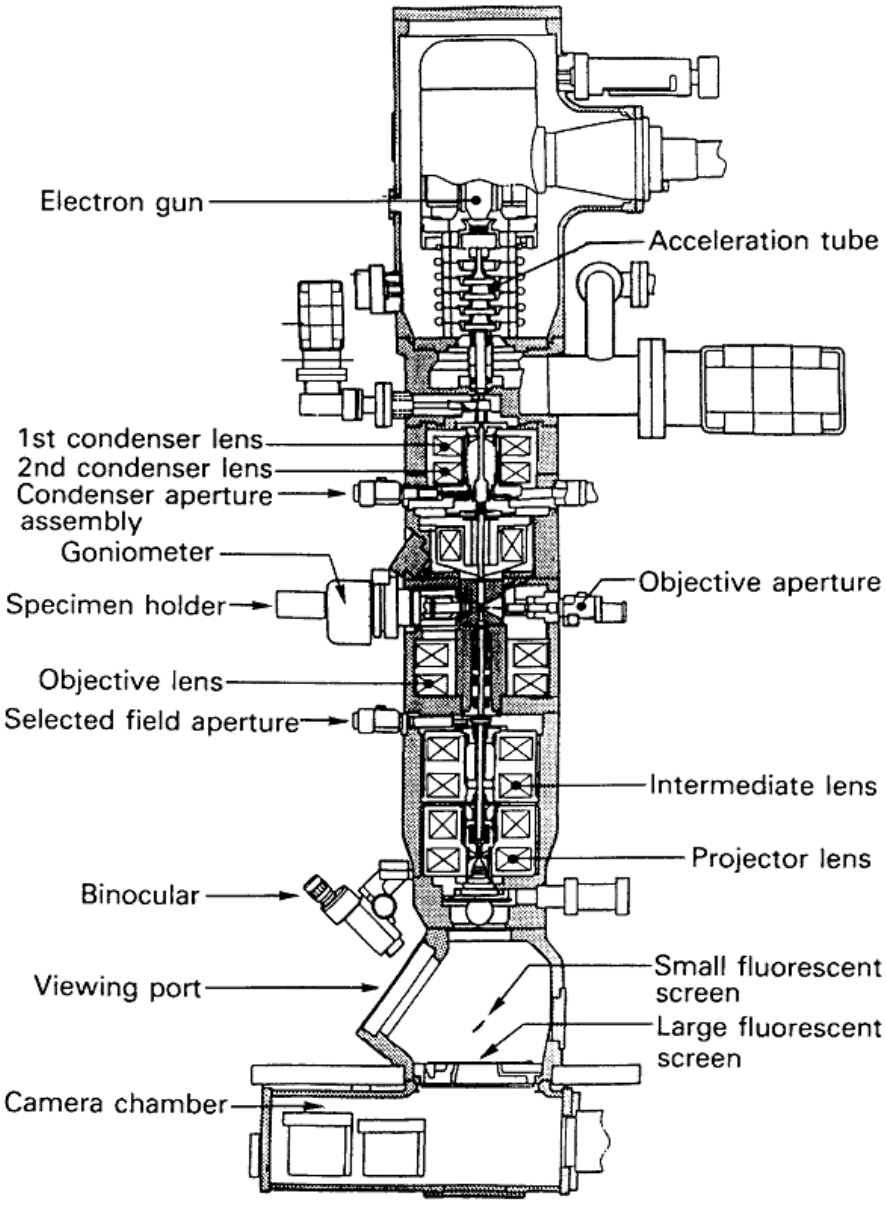

Figure 1. Schematics of a TEM.[13]

Transmission electron microscopy (TEM) is used in this thesis for imaging nanomaterials to determine their size and shapes. In short, a beam of high energy electron is focused onto a thin sample, and the transmitted electrons are magnified and focused onto a charge-coupled device (CCD) camera. Contrast is mainly obtained in the TEM by changes in the amplitude or phase of the incident electron wave. Amplitude contrast arises from differences in mass or thickness, as thicker areas will scatter more electrons than thinner areas within a sample. Likewise, sample areas containing denser materials (more mass) will also scatter more electrons than areas with less dense material. The Z-contrast means that heavier elements (with a large atomic number Z) will scatter electrons more intensely, thus making heavier elements appear darker in bright field TEM images.[14] Phase contrast is caused by interferences between different electron waves travelling through the sample, and often provides "fringes" – spaced contrast oscillations.

2.3.2 X-ray photoelectron spectroscopy

X-ray photoelectron spectroscopy (XPS) is a surface-sensitive spectroscopic technique. XPS spectra are measured by irradiating a material with soft X-rays while simultaneously measuring the kinetic energy and number of electrons that escape from the surface (typically 0 to 10 nm) of the sample material (Figure 2). The energy or wavelength of the irradiated X-ray is known (for Mg K_α X-rays, E_{photon} = 1253.6 eV), and the emitted electrons' kinetic energies are measured, so the electron binding energy of each of the emitted electrons can be calculated based on the conservation of energy: $E_{binding} = E_{photon} - (E_{kinetic} + \phi)$, where $E_{binding}$ is the binding energy (BE) of the electron, E_{photon} is the energy of the X-ray photons being used, $E_{kinetic}$ is the kinetic energy of the electron as measured by the instrument and ϕ is the work function dependent on both the spectrometer and the material.[15]

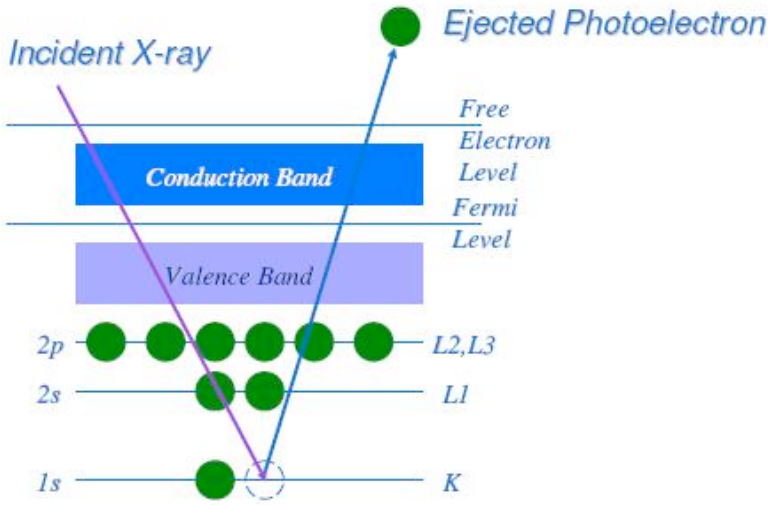

Figure 2. Schematics of the photoelectron ejection in XPS.

2.3.3 Inductively coupled plasma atomic emission spectroscopy (ICP-AES)

ICP-AES, also known as inductively coupled plasma optical emission spectrometry (ICP-OES), is an analytical technique used for the detection of trace metals. It is used to determine the loading of metals or the Si/Al ratios of the supported catalysts in this dissertation. The ICP-AES apparatus (Perkin-Elmer ICP Optima 7000 DV) uses an Ar plasma to excite the ionized sample of interest, generating element-specific emission lines. The intensity of the emission lines is used to quantify the concentration of the element in the sample. In a given analysis, 10-20 mg of a catalyst is dissolved in an acid solution (Aqua Regia and/or HF), diluted with water, and then filtered to remove any remaining particulates. A set of standards of known concentrations are used to first construct a calibration curve of the instrument, and then the sample of interest is run.

2.3.4 X-ray absorption spectroscopy (XAS)

X-ray absorption spectroscopy (XAS) measures the details of how x-rays are absorbed by an atom at energies near and above the core-level binding energies of that atom. The near edge X-ray absorption fine structure (NEXAFS) part of the XAS will provide local geometric and electronic information of the core element of the catalysts, e.g. Au[16,17] and Pt[18], and the extended X-ray absorption fine structure (EXAFS) will offer local structural information around the probed element.

2.4 References

1. Huang, W.; Kuhn, J. N.; Tsung, C.-K.; Zhang, Y.; Habas, S. E.; Yang, P.; Somorjai, G. A. Dendrimer Templated Synthesis of One Nanometer Rh and Pt Particles Supported on Mesoporous Silica: Catalytic Activity for Ethylene and Pyrrole Hydrogenation. *Nano Lett.* **2008**, *8*, 2027-2034.

2. Huang, W.; Liu, J. H.-C.; Alayoglu, P.; Li, Y.; Witham, C. A.; Tsung, C.-K.; Toste, F. D.; Somorjai, G. A. Highly Active Heterogeneous Palladium Nanoparticle Catalysts for Homogeneous Electrophilic Reactions in Solution and the Utilization of a Continuous Flow Reactor. *J. Am. Chem. Soc.* **2010**, *132*, 16771-16773.
3. Gross, E.; Liu Jack, H.-C.; Toste, F. D.; Somorjai, G. A. Control of selectivity in heterogeneous catalysis by tuning nanoparticle properties and reactor residence time. *Nat. Chem.* **2012**, *4*, 947-952.
4. Scott, R. W. J.; Ye, H.; Henriquez, R. R.; Crooks, R. M. Synthesis, Characterization, and Stability of Dendrimer-Encapsulated Palladium Nanoparticles. *Chem. Mater.* **2003**, *15*, 3873-3878.
5. Zhang, Y.; Grass, M. E.; Habas, S. E.; Tao, F.; Zhang, T.; Yang, P.; Somorjai, G. A. One-step Polyol Synthesis and Langmuir−Blodgett Monolayer Formation of Size-tunable Monodisperse Rhodium Nanocrystals with Catalytically Active (111) Surface Structures. *J. Phys. Chem. C* **2007**, *111*, 12243-12253.
6. Grass, M. E.; Zhang, Y.; Butcher, D. R.; Park, J. Y.; Li, Y.; Bluhm, H.; Bratlie, K. M.; Zhang, T.; Somorjai, G. A. A Reactive Oxide Overlayer on Rhodium Nanoparticles during CO Oxidation and Its Size Dependence Studied by In Situ Ambient-Pressure X-ray Photoelectron Spectroscopy. *Angew. Chem. Int. Ed* **2008**, *47*, 8893-8896.
7. Wang, F.; Sun, L.-D.; Feng, W.; Chen, H.; Yeung, M. H.; Wang, J.; Yan, C.-H. Heteroepitaxial Growth of Core–Shell and Core–Multishell Nanocrystals Composed of Palladium and Gold. *Small* **2010**, *6*, 2566-2575.
8. Zheng, Y.; Zhong, X.; Li, Z.; Xia, Y. Successive, Seed-Mediated Growth for the Synthesis of Single-Crystal Gold Nanospheres with Uniform Diameters Controlled in the Range of 5–150 nm. *Particle & Particle Systems Characterization* **2014**, *31*, 266-273.
9. Ni, W.; Kou, X.; Yang, Z.; Wang, J. Tailoring Longitudinal Surface Plasmon Wavelengths, Scattering and Absorption Cross Sections of Gold Nanorods. *ACS Nano* **2008**, *2*, 677-686.
10. Zhao, D.; Feng, J.; Huo, Q.; Melosh, N.; Fredrickson, G. H.; Chmelka, B. F.; Stucky, G. D. Triblock Copolymer Syntheses of Mesoporous Silica with Periodic 50 to 300 Angstrom Pores. *Science* **1998**, *279*, 548-552.
11. Luan, Z.; Hartmann, M.; Zhao, D.; Zhou, W.; Kevan, L. Alumination and Ion Exchange of Mesoporous SBA-15 Molecular Sieves. *Chem. Mater.* **1999**, *11*, 1621-1627.
12. Na, K.; Choi, M.; Ryoo, R. Cyclic diquaternary ammoniums for nanocrystalline BEA, MTW and MFI zeolites with intercrystalline mesoporosity. *J. Mater. Chem.* **2009**, *19*, 6713-6719.
13. Fultz, B.; Howe, J. M.: *Transmission electron microscopy and diffractometry of materials*; Springer Science & Business Media, 2012.
14. Williams, D. B.; Carter, C. B.: The transmission electron microscope. In *Transmission electron microscopy*; Springer, 1996; pp 3-17.

15. Lee, H.-L.; Flynn, N. T. X-ray photoelectron spectroscopy. *Handbook of Applied Solid State Spectroscopy* **2006**, 485-507.
16. Gross, E.; Liu, J. H.; Alayoglu, S.; Marcus, M. A.; Fakra, S. C.; Toste, F. D.; Somorjai, G. A. Asymmetric Catalysis at the Mesoscale: Gold Nanoclusters Embedded in Chiral Self-Assembled Monolayer as Heterogeneous Catalyst for Asymmetric Reactions. *J. Am. Chem. Soc.* **2013**, *135*, 3881-3886.
17. Gross, E.; Shu, X.-Z.; Alayoglu, S.; Bechtel, H. A.; Martin, M. C.; Toste, F. D.; Somorjai, G. A. In Situ IR and X-ray High Spatial-Resolution Microspectroscopy Measurements of Multistep Organic Transformation in Flow Microreactor Catalyzed by Au Nanoclusters. *J. Am. Chem. Soc.* **2014**, *136*, 3624-3629.
18. Li, Y.; Liu, J. H.-C.; Witham, C. A.; Huang, W.; Marcus, M. A.; Fakra, S. C.; Alayoglu, P.; Zhu, Z.; Thompson, C. M.; Arjun, A.; Lee, K.; Gross, E.; Toste, F. D.; Somorjai, G. A. A Pt-Cluster-Based Heterogeneous Catalyst for Homogeneous Catalytic Reactions: X-ray Absorption Spectroscopy and Reaction Kinetic Studies of Their Activity and Stability against Leaching. *J. Am. Chem. Soc.* **2011**, *133*, 13527-13533.

Chapter 3 - Supported Dendrimer-Encapsulated Metal Clusters: Toward Heterogenizing Homogeneous Catalysts

(This chapter covers similar material as in Ye, R.; Zhukhovitskiy, A. V.; Deraedt, C. V.; Toste, F. D.; Somorjai, G. A. *Acc. Chem. Res.* **2017**, *50*, 1894-1901. – reproduced with permission, copyright 2017 American Chemical Society.)

Abstract

In this chapter, metal clusters will be briefly introduced. The synthesis and characterizations of supported dendrimer-encapsulated metal clusters (DEMCs) will be described. The catalysis studies of supported DEMCs in both the batch and flow modes will be presented. Lastly, the current state of heterogenizing homogeneous catalysis will be summarized, and future directions for this area of research will be provided.

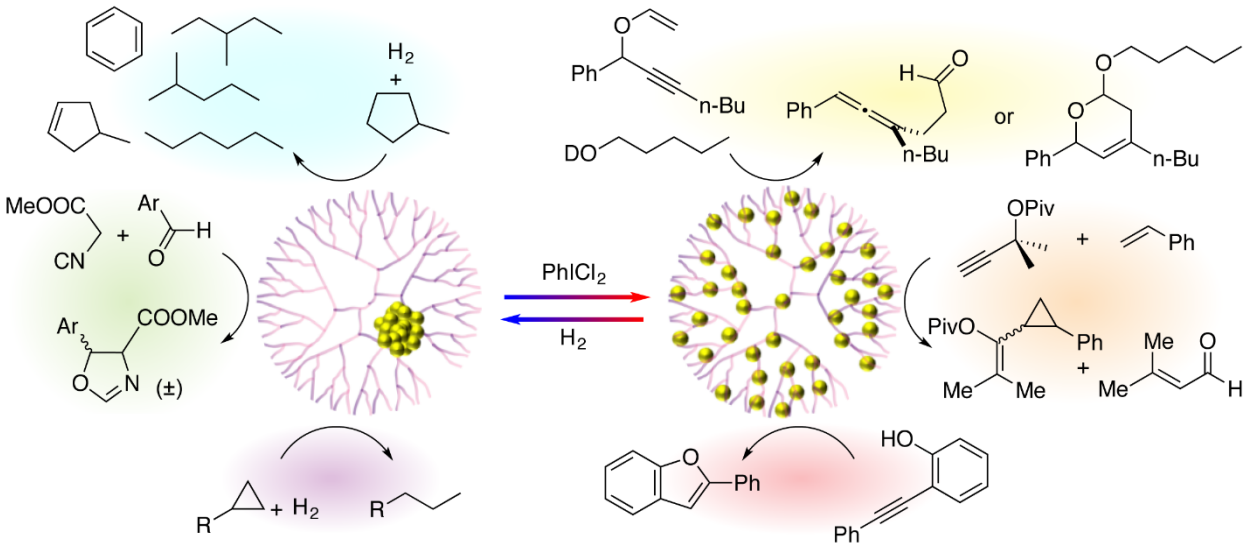

3.1 Introduction

The term “cluster” was applied by Cotton in the 1960s to refer to compounds containing metal–metal bonds.[1] Metal clusters contain countable numbers of atoms: anywhere between two and several hundred thousand (the upper limit is not precisely defined).[2] In the case of ultra-small gold clusters, their diameters range from sub-nanometer to ~2.2 nm (equivalent to ~10–300 atoms, often called nanoclusters).[3] Theoretical work by Nørskov’s group suggests the transition of surface chemical activity of Au clusters from molecular to bulk behavior to be around 560 atoms, corresponding to a diameter of ~2.7 nm.[4] Above this size, the surface properties of two probe adsorbates, O and CO, are indistinguishable from that of an extended surface. Below that critical size, finite-size effects can be observed, and facets become small enough for the charge redistribution upon oxygen adsorption starts reaching the edge of the particle. [4]

Clusters, in general, may have unusual catalytic properties. The high ratio of surface-to-bulk atoms in the clusters facilitates both reactant activation and product desorption, offering new reaction pathways.[5] As the most active catalysts are usually made from precious metals, the use of clusters could also have significant economic impacts by increasing the turnover number and turnover frequency per metal atom. They can act as individual active sites, and minor changes in size and composition – e.g. the addition or removal of a single atom – can have a substantial influence on the activity and selectivity of a reaction.[6] Gates’ group reported that Ir_4 and Ir_6 clusters differ in catalytic activity both from each other and from metallic Ir particles.[7] Anderson’s group observed that the Pd 3d binding energy varied nonmonotonically with cluster size and that the changes correlate with strong size variations in CO oxidation activity.[8]

Control of cluster structural integrity (e.g., size, geometry) during their preparation and throughout a cluster-catalyzed transformation is critical to achieve a desired reactivity profile. However, in the pursuit of cluster stabilization through surface modification with ligands, catalyst activity is often compromised. Judicious ligand design is critical to balance cluster structural integrity and performance as a catalyst. One reliable and modular method to synthesize the metal clusters is through the use of dendrimers.[9-12] Dendrimer-cluster multivalent interactions protect the cluster from aggregation or leaching; meanwhile, the weak nature of individual interactions with surface sites preserves the catalyst activity.[13] Dendrimer-encapsulated metal clusters (DEMCs) generally exhibit high catalytic activity in homogeneous reactions – e.g. Heck, Suzuki, and Sonogashira cross-coupling – often superior to classical homogeneous catalysts.[14,15] The latter are, however, not readily recyclable and are unstable at high temperatures, giving rise under reaction conditions to “cocktails” of catalytically active species: metal complexes, clusters and nanoparticles.[16] Furthermore, these same catalysts displayed mediocre performance in traditionally heterogeneous transformations, e.g. hydrogenation of pyrrole. After applying the supported DEMCs in the hydrogenation of pyrrole,[17] we sought to further develop this platform of active, selective, recyclable,

and air-stable catalysts for academically and/or industrially important transformations. Besides improved thermal stability and enhanced recyclability, supported DEMCs are operational in all solvents even though unsupported DEMCs are commonly soluble only in protic solvents. Comparing to supported cluster catalysts without dendrimer, dendrimers in supported DEMCs allow the tuning of the metal oxidation states, and also ensure the cluster stability against aggregation or leaching. In our laboratories, we have utilized the dendrimer-stabilization approach to prepare clusters and load them into mesoporous supports for heterogeneous catalysis. The clusters discussed in this account are confined within individual dendrimers, while clusters stabilized by multiple dendrimers, which are relatively more vulnerable to leaching, are covered elsewhere.[15] This chapter will focus on the investigations and developments of supported DEMCs on catalytic reactions. The synthesis and characterizations of supported DEMCs will be covered, followed by catalysis studies in the batch and flow modes. After a summary of the current knowledge, future directions will be discussed.

3.2 Synthesis and characterization

DEMCs were synthesized adapting the method developed by Crooks[18]. The synthesis procedure can be applied to Rh, Pd, Pt, and Au with generation 4 OH-terminated polyamidoamine (PAMAM) dendrimer (henceforth referred to as G4OH). Dendrimer generation is the number of branching nodes along a single path from the center of the dendrimer to the periphery (Figure 1).[19] A dendrimer stock solution was mixed with a metal precursor for the complexation between these components. An excess of freshly prepared $NaBH_4$ solution was added dropwise with vigorous stirring. After the metal was reduced, the solution was purified via dialysis in cellulose dialysis tubing against an excess of deionized water. The DEMCs were immobilized onto mesoporous silica, e.g. SBA-15 (SBA stands for Santa Barbara),[20] via sonication. The deposition and anchoring of the DEMCs on the mesoporous support resulted from the hydrogen bonding between the terminal hydroxyl groups of G4OH and the surface of the SiO_2 support.[17] This interaction prevented the detachment of DEMCs from the mesoporous support, even under liquid-phase reaction conditions or at elevated temperatures. The supported DEMCs displayed no detectable leaching, and in this regard functioned as true heterogeneous catalysts. However, the tunable oxidation state of the surface metal atoms in DEMCs rendered these catalysts effective in a variety of transformations (*vide infra*).

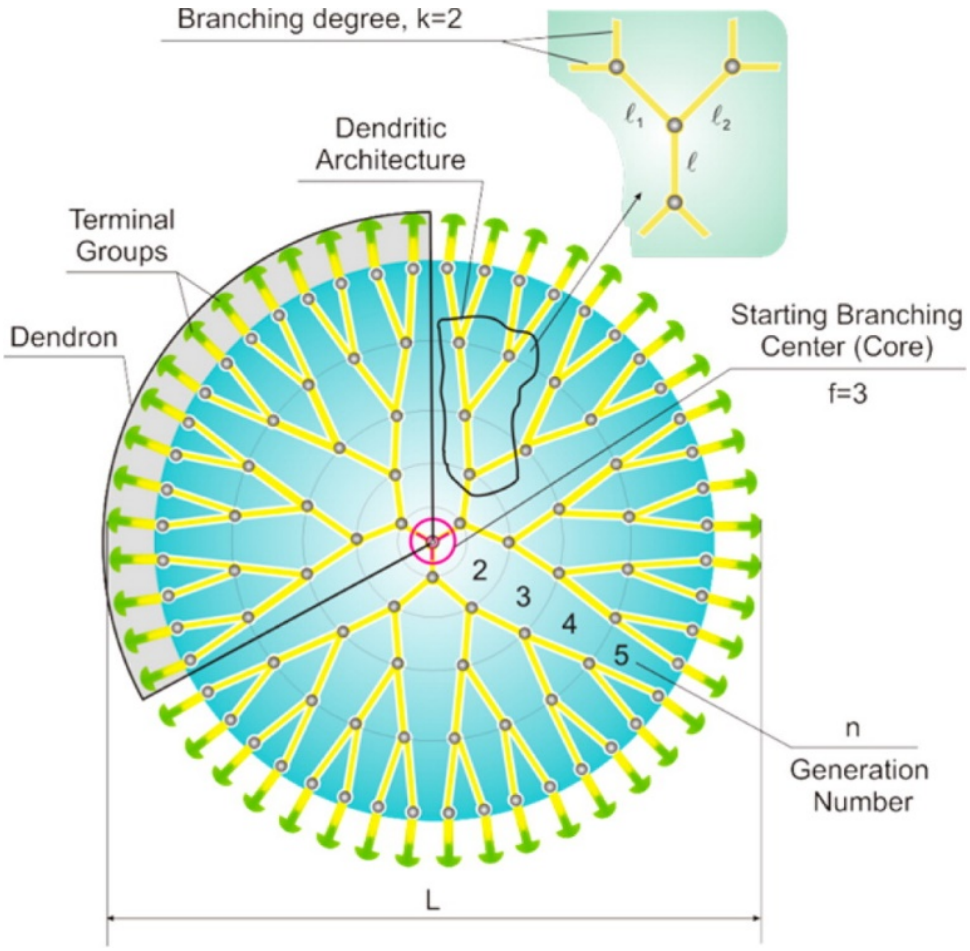

Figure 1. Schematic representation of a classical dendrimer molecule. Adapted with permission from ref 19. Copyright American Chemical Society.

The DEMCs were characterized by various techniques before and after loading, as well as during and after the completion of the catalyzed transformation. Transmission electron microscopy (TEM) offered direct visualization of the morphology of the DEMCs (Figure 2). The DEMCs possessed reproducibly uniform size and shape due to templation and stabilization by the dendrimer. These cluster parameters did not appear to change upon loading onto the SBA-15 support. The sizes of DEMCs ranged from 1 to 2.7 nanometers, depending on the metal and the metal-to-dendrimer molar ratio. These sizes fell within the aforementioned critical size range, in which the clusters exhibited finite-size effects. Inductively coupled plasma optical emission spectrometry (ICP-OES) enabled quantification of the metal content in the supported samples and the extent of metal leaching during the catalytic reactions. X-ray photoelectron spectroscopy (XPS) was utilized to determine the oxidation states of the metal atoms within DEMCs. For the as-synthesized Rh or Pt DEMCs, multiple oxidation states were observed. The oxidized

portion was proposed to arise from incomplete reduction of metal salts during the DEMC synthesis or air exposure of the XPS sample.[17]

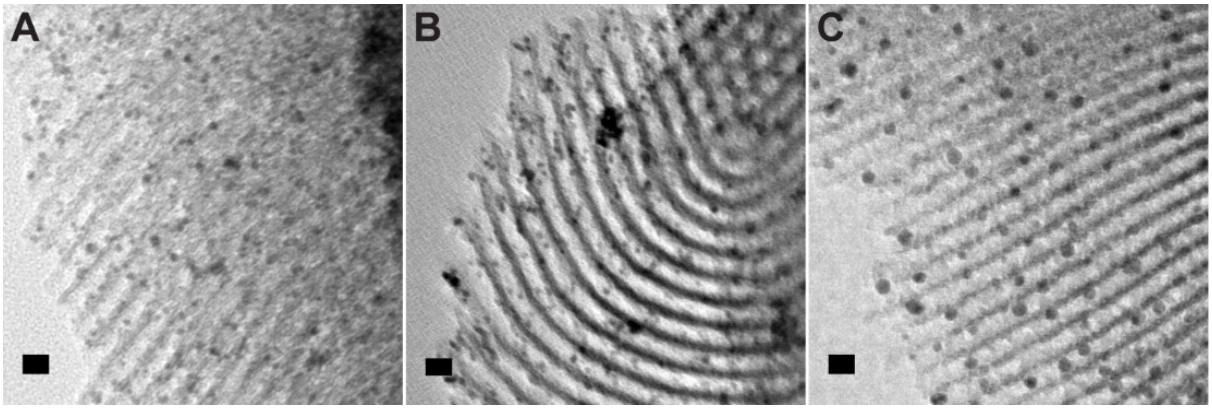

Figure 2. Representative TEM images of DEMCs supported in SBA-15. Rh_{40}/G4OH/SBA-15 (A), Pt_{40}/G4OH/SBA-15 (B), and Au_{40}/G4OH/SBA-15 (C). The scale bars are 10 nm.

The oxidation states and coordination environment of Pt DEMCs were monitored *in situ* via near edge X-ray absorption fine structure (NEXAFS) and extended X-ray absorption fine structure (EXAFS).[21] As evidenced in Figure 3, reduction of Pt via an H_2 treatment led to high Pt–Pt and low Pt–Cl or Pt–O coordination numbers derived from EXAFS data. The addition of $PhICl_2$, a hypervalent iodine oxidant, into the reaction solution generated Pt(II) and Pt(IV), as shown by EXAFS and NEXAFS analysis. The reduction and oxidation cycle could be repeated.[21] These powerful techniques provide valuable molecular insight into catalysts' operation under reaction conditions, even though currently their scan rate is in the order of minutes and thus cannot capture faster transformations.

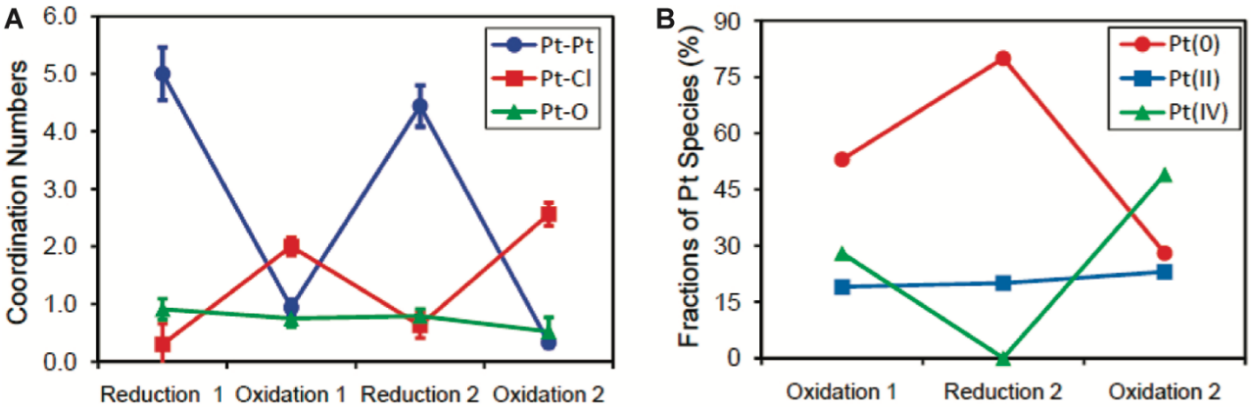

Figure 3. (A) Average coordination numbers of Pt atoms in the supported Pt catalyst after a sequence of hydrogen reduction and $PhICl_2$ oxidation treatments in the toluene derived from EXAFS analysis. (B) The fractions of Pt(0) and Pt(II) and Pt(IV) chloride

species of the Pt catalyst derived from NEXAFS analysis. Reprinted with permission from ref 21. Copyright American Chemical Society.

3.3 Catalysis in batch reactors

One of the first examples of supported DEMCs was reported by Chandler's group.[22] Pt DEMCs were deposited onto a commercial high surface area silica support. A pretreatment of O_2/He at 300 °C followed by H_2 flow at 300 °C was used to remove the dendrimer. No significant change in clusters was observed by TEM. This catalyst was used for the oxidation of CO and the hydrogenation of toluene. Interestingly, the clusters obtained from the DEMCs were more active than a classic Pt/SiO_2 catalyst.[22] Simultaneously, Amiridis and colleagues investigated Pt DEMCs for catalytic CO oxidation.[23] Later on, applications of supported DEMCs included the selective hydrogenation of 3,4-epoxy-1-butene by Williams' group,[24] and the trans-2-butene conversion by Zaera's group.[25]

In our groups, DEMCs supported on SBA-15 were active for a variety of reactions, and unlike particles capped with polyvinylpyrrolidone (PVP) or other agents, calcinations or equivalent manipulations of the DEMCs was unnecessary to uncover the active sites. In addition to permitting the catalyst to be recycled, deposition of the DEMCs on SBA-15 imparted additional thermal stability against aggregation. Furthermore, as PAMAM dendrimers were normally soluble only in protic solvents or solvent mixtures, but DEMCs loaded on SBA-15 were compatible with a wide array of aprotic organic solvents.

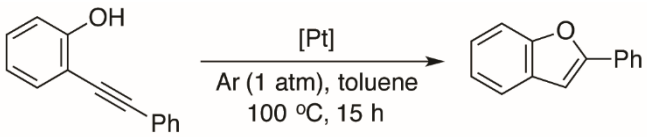

Catalyst	Yield*
Pt_{40}/G4OH/SBA-15 (4 mol%)	10%
Pt_{40}/G4OH/SBA-15 (4 mol%), $PhICl_2$ (12 mol%)	98%
$PtCl_2$ (5 mol%) (2 h)	97%

* Determined by NMR spectroscopy

Figure 4. Hydroalkoxylation reaction with Pt catalysts.

We utilized supported DEMCs for the functionalization of π-bonds, which had previously been the realm of mainly homogeneous catalysts. Our initial studies focused on a hydroalkoxylation reaction, in which an electrophilic Pt catalyst activated an alkyne towards nucleophilic attack by an alcohol functionality (Figure 4). Initial attempts with 1.0 nm Pt_{40}/G4OH/SBA-15 generated only 10% yield of product. (Pt_{40} represents the molar ratio of Pt/G4OH is 40/1 in the synthesis.) This result was most likely due to the presence

of catalytically inactive Pt oxide species on the Pt surface: indeed, XPS revealed that >70% of Pt were Pt(II) in Pt_{40}/G4OH/SBA-15. Crooks and Zhao demonstrated the reduction of Pt(II) in the synthesis of Pt_{40}/G4OH,[18] so the presence of Pt(II) in the supported clusters is likely due to surface oxidation in the loading and drying process. Oxidized Pt sites were not deemed intrinsically inactive – rather the oxide form of Pt was unreactive. Indeed, treatment of H_2-pre-treated Pt_{40}/G4OH/SBA-15 with $PhICl_2$ resulted in 98% yields.[26] In this case, $PhICl_2$, an oxidant, generated Pt chloride rather than oxide surface species and thereby transformed the Pt clusters' surface into a catalytically active one.

Another critical consideration was the nature of the catalytically active species: namely, did the oxidized Pt ions leach out from DEMCs and catalyze the reaction in a homogeneous fashion? We sought to address this question for the DEMC system *in situ* under optimal performance conditions. A three-phase test[27] was used with Wang resin-bound substrate (Figure 5A). Homogeneous $PtCl_2$ provided 26% conversion of resin-bound substrate to product. However, a negligible conversion (<2%) was observed for Pt_{40}/G4OH/SBA-15 oxidized with $PhICl_2$. A filtrate transfer test was conducted with a Pt_{40}/G4OH/mesoporous silica pellet. A solution of starting material, $PhICl_2$, and solvent (toluene) were added to the catalyst pellet in a reactor (step *i* in Figure 5B). After 42% yield was achieved, the reaction solution was transferred to another vessel without the heterogeneous catalyst (step *ii* in Figure 5B). A fresh solution of starting material was subsequently added to the original reaction vessel with the remaining oxidized catalyst pellet (step *ii* in Figure 5B). Both vessels were next subjected to otherwise identical reaction conditions (step *iii* in Figure 5B); product was again generated in the vessel with the catalyst pellet, while in the vessel without it, no further conversion took place, and product yield remained unchanged. Reactivity due to any leached homogeneous species could thus be ruled out; the active catalyst was in fact heterogeneous. Moreover, ICP-OES confirmed that Pt species did not leach from the Pt_{40}/G4OH/SBA-15 catalyst when it was isolated after the reaction, and the concentration of Pt in the supernatant of the reaction solution was below the instrument's detection limit (1 ppm). Finally, the catalyst before and after reaction did not show any appreciable morphology change in TEM images.[26] This observation underscores the stability and recyclability of our supported DEMC catalyst system.

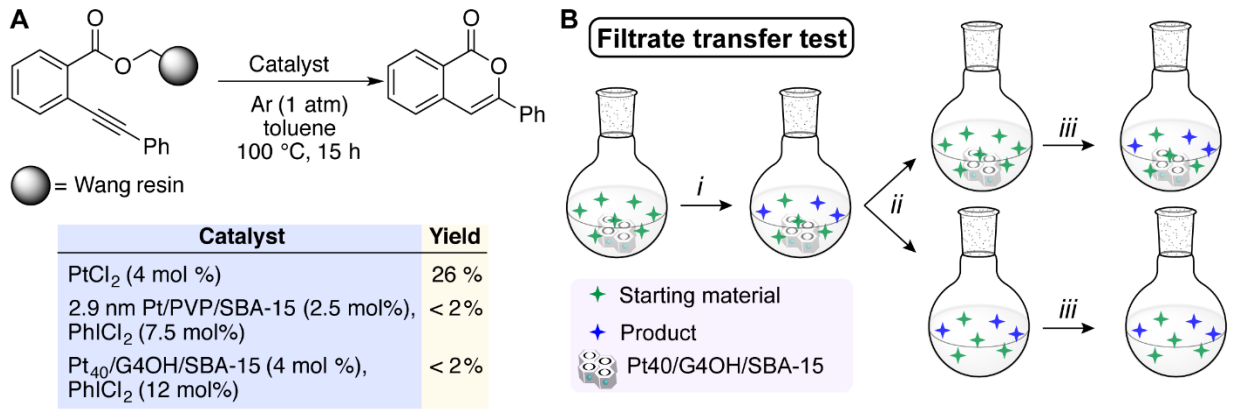

Catalyst	Yield
$PtCl_2$ (4 mol %)	26 %
2.9 nm Pt/PVP/SBA-15 (2.5 mol%), $PhICl_2$ (7.5 mol%)	< 2%
Pt_{40}/G4OH/SBA-15 (4 mol %), $PhICl_2$ (12 mol%)	< 2%

Figure 5. Catalyst heterogeneity tests. (A) A three-phase test to determine the presence of a homogeneous catalyst by leaching or release and capture. Yields were determined by NMR versus internal standard. (B) A filtrate transfer test. (*i*) To the reaction vessel charged with a substrate was added a pellet of Pt_{40}/G4OH/mesoporous silica catalyst, toluene, and $PhICl_2$ oxidant. The mixture was stirred and the yield monitored. (*ii*) When the reaction reached 42% yield, the solution was removed and placed into a new vessel. A fresh solution of starting material was added to the original vessel with the catalyst pellet. (*iii*) Both vessels were then stirred and monitored. The yield was determined by gas chromatography versus internal standard. All transfers and reactions were conducted under Ar at 100 °C. The catalyst pellet was pre-reduced under H_2 atmosphere at 100 °C for 36 h before reaction. Adapted with permission from ref 26. Copyright Nature Publishing Group.

The stability of DEMCs against leaching is a key property of heterogenized homogeneous catalysis. When toluene, a nonpolar solvent, was used in combination with a polar solid phase (the mesoporous SiO_2, the dendrimer, and the metal ions), metal ions formed by $PhICl_2$ oxidation tended to reside inside the dendrimer and their dissociation of from the polar support into the nonpolar solvent was unfavorable, even at a high temperature. However, for a more polar solvent (such as $MeNO_2$), capable of strong coordination with metal ions and strong interaction with the dendrimer, dissociation of the metal ions (or dendrimers carrying the metal ions) became more pronounced, and leached metal ions were detected in the liquid phase.[28]

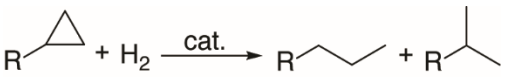

Figure 6. Catalytic ring opening reactions of cyclopropane derivatives.

One of the long-term goals of this ongoing research program is to leverage heterogenized homogeneous catalysis to facilitate a broad spectrum of complex chemical transformations. During the past 10 years, we and others have already

demonstrated that in addition to intramolecular π-bonds activation reactions, DEMCs were excellent catalysts for several other classes of transformations, including C–C bond activation and C–C bond formation. Elucidation of the C–C bond activation mechanism is essential for the selective production of hydrocarbons in the petroleum industry. Ring-opening reactions of cyclopropane derivatives were used as a model to investigate C–C bond activation with supported DEMCs (Figure 6). While homogeneous rhodium catalysts showed little or no activity even at elevated temperatures toward the ring opening of cyclopropylbenzene, Rh_{40}/G4OH/SBA-15 showed a turnover frequency (TOF) of 2.24 h^{-1} at room temperature, and the DEMCs were recyclable. The products of the DEMCs catalyzed reactions were 100% linear, in contrast to homogeneous counterparts that produced the branched products, likely because of different reaction mechanisms. The reaction mechanism with the rhodium DEMCs was investigated. Reactants with electron-donating groups on the three-member ring exhibited a high reaction rate, probably due to a more stable cationic transition state in the rate-limiting step on the rhodium surface. Larger cluster size led to higher TOF and smaller reaction activation energy, probably because the stronger metallic character of the larger clusters favors the hydrogen chemisorption. The capping agent of the clusters affected both the reaction rate and the activation energy, analogous to ancillary ligand effects observed in homogenous catalysts. The study revealed the above mentioned fundamental factors controlling catalytic C–C bond activation activity and selectivity.[29]

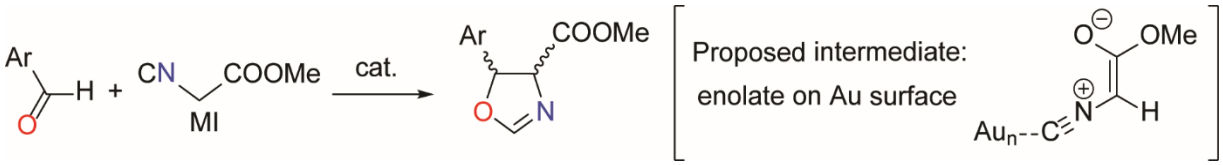

Figure 7. Hayashi-Ito aldol reaction of methyl isocyanoacetate (MI) and benzaldehydes and the proposed intermediate.

The Hayashi-Ito aldol reaction of methyl isocyanoacetate (MI) and benzaldehydes, a classic homogeneous Au(I)-catalyzed reaction, aptly demonstrated the excellent catalytic activity and controlled selectivity of supported DEMCs (Figure 7).[30] Au_{40}/G4OH/SBA-15 showed higher activity and diastereoselectivity toward the *trans* product than DEMCs of Pd, Rh, or Pt, and the homogeneous analogs. Au DEMCs were stable for at least six cycles without apparent deactivation. The activation energy was insensitive to the size of Au DEMCs or the support pore profile. However, larger pore sizes of the support increasingly favored the *trans* product. Our speculation was that the *trans* product was more sterically demanding, so when the pore was small and the space was limited, kinetic control led to an increase in the *cis*:*trans* product ratio. Infrared (IR) spectroscopy suggested a strong interaction between MI and the gold catalyst, implying the formation of an enolate ion intermediate from MI (Figure 7). The Hammett plot of

benzaldehyde with various substituents was linear with a positive slope, indicating an increased electron density on the carbonyl carbon atom in the transition state of the rate-limiting step. These evidences supported our hypothesis that the rate-limiting step involved a nucleophilic attack of the aldehyde by the enolate formed from the deprotonated MI.[30]

3.4 Catalysis in flow reactors

To take full advantage of the heterogeneous nature of the supported DEMCs, we also studied the hydroalkoxylation reaction (shown in Figure 4) in a fixed bed plug flow reactor in a continuous flow mode. In this case, Pd_{40}/G4OH/SBA-15 were used, as they were highly active and could provide a full conversion of reactants to products at room temperature. Separating the catalyst from reaction medium or any further purification of the product was obviated in this operation mode. In addition, the activity of Pd_{40}/SBA-15 at different reaction temperatures could be conveniently measured in a flow reactor, and the apparent activation energy was determined to be 20.0 kcal/mol. In comparison, multiple reactions must be repeated at different temperatures to measure the activation energy in a batch mode. Thus, any operational error in the batch mode would generate inaccuracy in the activation energy. However, all reaction parameters could be controlled precisely and reproduced easily in a flow reactor.[31]

Applications of supported DEMCs in complicated reactions, e.g. a cascade reaction, highlight the scope of our DEMC system. A cascade rearrangement of propargyl pivalate **1** /cyclopropanation of enyne **2** was investigated with $AuCl_3$ and Au DEMCs (Figure 8A–B). The primary product **3** can rearrange under the reaction conditions into two secondary products, **4** and **5**. Homogeneous $AuCl_3$ at room temperature gave a 40% yield of cyclopropane **3**, with a *cis*:*trans* ratio of 3:1, accompanied by a 10% yield of products **4** and **5** (in a 3:2 ratio) formed by the rearrangement of the product *cis*-**3**. However, Au-G4OH/SBA-15 in the batch mode led to a *cis*:*trans* ratio of 12:1 for **3** and only a small amount of the rearrangement products **4** and **5** (1% each). Another advantage of using supported DEMCs in a flow mode is that chemoselectivity was tuned by modifying the residence time of the reactants. Using the same catalyst in a flow reactor with a flow rate of 5 mL/h, an 18% yield of cis-cyclopropane **3** was measured (*cis*:*trans* ratio of 100:0), along with 2% of secondary products **4** and no measurable **5**. Reducing the flow rate to 0.1 mL/h and thereby increasing the residence time, increased the conversion to 72% and an exclusive selectivity for the rearrangement product **4** was obtained. A linear increase in the reactivity coupled with a linear enhancement in the selectivity towards the rearrangement product **4** was observed when the residence time of the reactants was modified continuously.[28] In the cascade reaction above, increasing the flow rate would shorten the residence time of the intermediate to prevent further rearrangements. Conversely, the final rearrangement product was favored by increasing the residence time. Such method

of tuning chemoselectivity would be an advantage untenable in a batch reaction mode as well as in traditional homogeneous catalysis.[28]

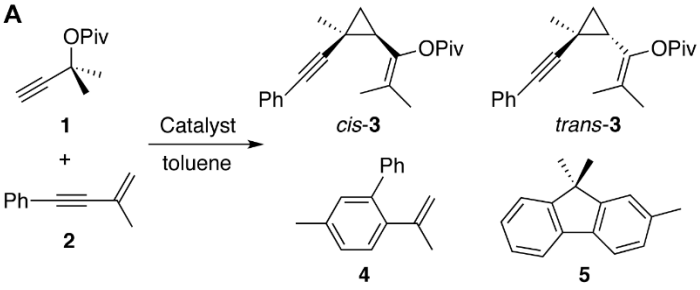

Catalyst	% Conversion	% 3 (cis:trans)	% 4 + 5 (4:5)
$AuCl_3$*	50	40 (3:1)	10 (3:2)
Au-G4OH batch*,†	40	38 (12:1)	2 (1:1)
Au-G4OH flow (5 mL/h)‡	20	18 (100:0)	2 (100:0)
Au-G4OH flow (0.1 mL/h)‡	72	0	72

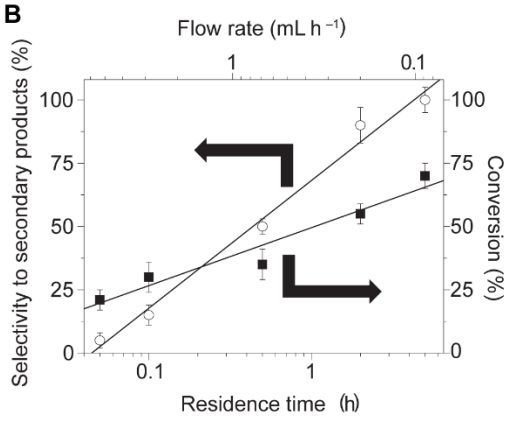

Figure 8. (A) Gold-catalysed cascade cyclopropanation rearrangement in a batch reactor and a flow reactor, respectively. Reaction yield and selectivity were measured by ^{1}H NMR integration. *Reaction run for 20 hours at r.t. with 2 mol% catalyst. †6 mol% oxidizer was added. ‡Total yield and selectivity were measured after four hours of reactant flow at r.t. Reactant and oxidizer concentrations were 0.15 and 0.015 M, respectively. (B) Flow measurements of the conversion and selectivity of the cascade cyclopropanation-rearrangement reaction as a function of reactant residence time. With 2.0 ± 0.3 nm Au-G4OH/SBA-15 as the catalyst, the catalytic conversion (filled squares) and selectivity (open circles) towards the formation of secondary products **4** and **5** at room temperature increased as a function of the residence time of the reactants. The reactant and oxidizer concentrations were 0.15 and 0.015 M, respectively. Error bars represent up to ±6% differences in reproducibility. Adapted with permission from ref 28. Copyright Nature Publishing Group.

Analysis of catalytic organic transformations in flow reactors and detection of short-lived intermediates are essential for optimization of these complex reactions. Spectral mapping of the organic phase and metallic catalyst during the multistep formation of a dihydropyran in a flow microreactor was achieved through micrometer-sized synchrotron-based IR and X-ray beams with a spatial resolution of 15 μm (Figure 9). Au/G4OH/SBA-15 activated the cascade reaction with high yield under continuous flow conditions. *In situ* synchrotron-sourced IR microspectroscopy detected the evolution of the reactant – a substituted propargyl vinyl ether – into the primary product, allenic aldehyde, which was then further isomerized to the acetal, the secondary product. The kinetic evolution of the organic reaction and the essential role of the primary product as an intermediate were analyzed via *in situ* IR microspectroscopy. Direct correlation was obtained between the catalytically active areas along the flow reactor, as

detected by IR, to local high concentrations of the catalytically active species, Au(III), as analyzed by μm-NEXAFS spectroscopy. These measurements indicated that the oxidation state of the catalyst and, as a consequence, its catalytic properties were altered along the flow reactor. Mapping of the gradual evolution of this multistep catalytic process afforded a deeper mechanistic understanding of the kinetic role of the intermediates in this study.[32]

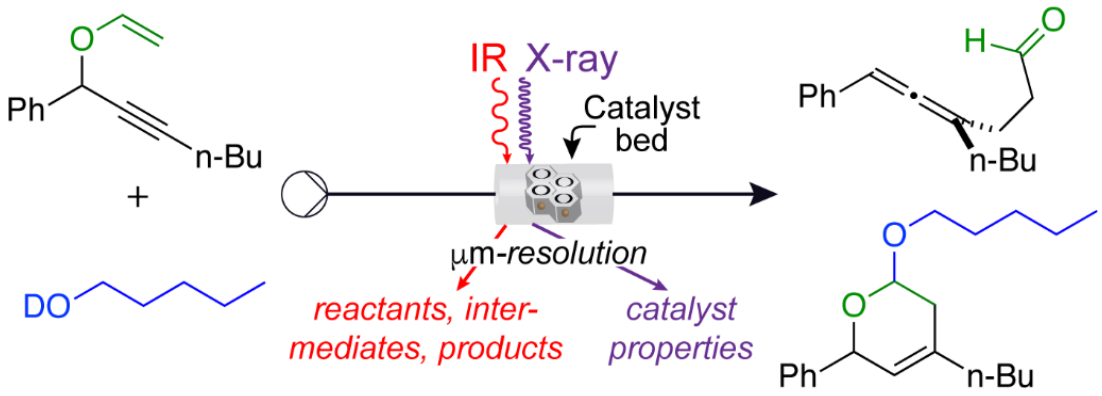

Figure 9. Schematic representation of a cascade reaction catalyzed by Au/G4OH/SBA-15 characterized *in situ* by synchrotron-sourced IR microspectroscopy and μm-NEXAFS spectroscopy.

The DEMCs also worked well in a gas flow reactor at temperatures in the range of 150−250 °C (Scheme 1). Pt DEMCs were highly active for the hydrogenation of the methylcyclopentane (MCP) at 200−225 °C, with TOF up to 334 h^{-1}, higher than other catalysts reported in the literature. The selectivity of 99.6% was achieved for the ring opening isomerization at high conversion (94%). Rh and Pd DEMCs brought different product selectivity. The deactivation of the catalysts began at temperatures above 250 °C, which could be attributed to the decomposition of the dendrimer and agglomeration of the clusters. The broad applications and wide operation conditions of DEMCs in catalysis were demonstrated.[33]

Scheme 1. Methylcyclopentane hydrogenative isomerization catalyzed by supported DEMCs.

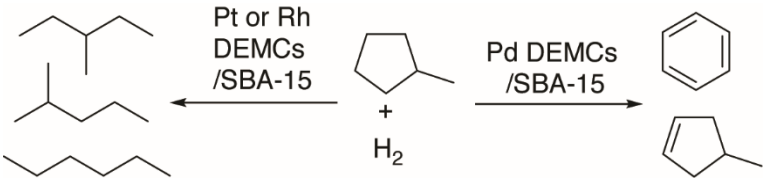

3.5 Conclusions

The reactions that have been studied with supported DEMCs in our groups are summarized in Table 1. Advantages of supported DEMCs as heterogenized homogeneous catalysts include the following: (1) the catalysts have the activity equivalent to homogeneous catalysts, which conventional heterogeneous catalysts lack, (2) the heterogenized homogeneous catalysts are recyclable in contrast to homogeneous catalysts with comparable performance, and (3) enhanced activity or selectivity compared to conventional homogeneous catalysts is enabled by exclusive heterogeneous handles for optimization.

Table 1. A list of transformations studied with supported DEMCs in our groups

reaction type	DEMC metal	reference
hydrogenation and ring opening	Pt or Rh	17, 29
hydroalkoxylation reaction	Pt or Pd	21, 26, 31
Hayashi-Ito aldol reaction	Au	30
cascade cyclopropanation rearrangement	Au	28
cascade dihydropyran formation	Au	32
hydrogenative isomerization	Pt, Pd, or Rh	33

3.6 Outlook

Besides the reactions shown in Table 1, we expect that a board range of transformations will benefit from supported DEMCs as heterogenized homogeneous catalysts. To expand the reaction scope, supported DEMCs more resistant to harsh reaction conditions are desired. In the cases described above, the formation of stable heterogeneous catalysts took advantage of the weak interactions between preformed DEMCs and a support. The fixation of dendrimer onto a support via covalent bonds can also be performed before the synthesis of DEMCs via two strategies. The first strategy is to end-link the dendrimer or dendron (usually contains a single chemically addressable group) to the support (convergent synthesis).[34] The second strategy consists of dendrimer growth, generation-by-generation, at the surface of the support (divergent synthesis). Interestingly, Astruc's group showed that the resultant catalysts synthesized via these two different routes could have different activity.[35] These synthesis methods might offer DEMCs with higher stability against deactivation or leaching in harsh conditions.

We have demonstrated that heterogenized homogeneous catalysis is achieved via DEMCs. However, with the exception of Ag and Cu, the main elements used as the active catalysts were limited to precious metals, i.e. Pt, Au, Pd, and Rh. Catalysis with other elements, particularly the more affordable and abundant first-row transition metals, like Fe, Co, and Ni, has few precedents.[36] These metals are prone to aggregation due to

their ferromagnetism in the metallic state generated during the synthesis of clusters. Furthermore, they are vulnerable to oxidation when exposed to air, which complicates the formation of clusters. These intrinsic detriments account for their limited applications in the heterogenized homogeneous catalysis. It is highly desirable to broaden the cluster catalysis via incorporating earth-abundant metals in DEMCs.

Despite its broad utility, the supported DEMCs catalysts presently lack a modular handle to tune reaction outcomes. Yet, rapid optimization of catalyst performance metrics such as enantio-, diastereo-, regio-, and chemo-selectivity would greatly advance the sophistication and scope of transformations catalyzed by metal clusters. Ancillary ligands, commonly utilized in transition metal catalysis to tune catalyst selectivity, were a logical choice of the desired modular handles to be added to metal clusters.[37] We expect to achieve product enantioselectivity using this strategy.

Rapid developments of characterization tools, especially synchrotron-based instruments,[38] would allow further understanding of structure-property relationship of the metal clusters. This knowledge would facilitate the development of the next-generation clusters catalysts.

3.7 References

1. Bertrand, J. A.; Cotton, F. A.; Dollase, W. A. The Crystal Structure of Cesium Dodecachlorotrirhenate-(III), a Compound with a New Type of Metal Atom Cluster. *Inorg. Chem.* **1963**, *2*, 1166-1171.

2. Mason, M. G. Electronic structure of supported small metal clusters. *Physical Review B* **1983**, *27*, 748-762.

3. Jin, R.; Zeng, C.; Zhou, M.; Chen, Y. Atomically Precise Colloidal Metal Nanoclusters and Nanoparticles: Fundamentals and Opportunities. *Chem. Rev.* **2016**, *116*, 10346-10413.

4. Kleis, J.; Greeley, J.; Romero, N. A.; Morozov, V. A.; Falsig, H.; Larsen, A. H.; Lu, J.; Mortensen, J. J.; Dułak, M.; Thygesen, K. S.; Nørskov, J. K.; Jacobsen, K. W. Finite Size Effects in Chemical Bonding: From Small Clusters to Solids. *Catal. Lett.* **2011**, *141*, 1067-1071.

5. Christopher, P.; Xin, H.; Linic, S. Visible-light-enhanced catalytic oxidation reactions on plasmonic silver nanostructures. *Nat. Chem.* **2011**, *3*, 467-472.

6. Matsubu, J. C.; Zhang, S.; DeRita, L.; Marinkovic, N. S.; Chen, J. G.; Graham, G. W.; Pan, X.; Christopher, P. Adsorbate-mediated strong metal–support interactions in oxide-supported Rh catalysts. *Nat. Chem.* **2017**, *9*, 120-127.

7. Xu, Z.; Xiao, F. S.; Purnell, S. K.; Alexeev, O.; Kawi, S.; Deutsch, S. E.; Gates, B. C. Size-dependent catalytic activity of supported metal clusters. *Nature* **1994**, *372*, 346-348.

8. Porosoff, M. D.; Chen, J. G. Trends in the catalytic reduction of CO2 by hydrogen over supported monometallic and bimetallic catalysts. *J. Catal.* **2013**, *301*, 30-37.
9. Musselwhite, N.; Na, K.; Sabyrov, K.; Alayoglu, S.; Somorjai, G. A. Mesoporous Aluminosilicate Catalysts for the Selective Isomerization of n-Hexane: The Roles of Surface Acidity and Platinum Metal. *J. Am. Chem. Soc.* **2015**, *137*, 10231-10237.
10. Na, K.; Choi, K. M.; Yaghi, O. M.; Somorjai, G. A. Metal Nanocrystals Embedded in Single Nanocrystals of MOFs Give Unusual Selectivity as Heterogeneous Catalysts. *Nano Lett.* **2014**, *14*, 5979-5983.
11. Choi, K. M.; Na, K.; Somorjai, G. A.; Yaghi, O. M. Chemical Environment Control and Enhanced Catalytic Performance of Platinum Nanoparticles Embedded in Nanocrystalline Metal–Organic Frameworks. *J. Am. Chem. Soc.* **2015**, *137*, 7810-7816.
12. Crooks, R. M.; Zhao, M.; Sun, L.; Chechik, V.; Yeung, L. K. Dendrimer-Encapsulated Metal Nanoparticles: Synthesis, Characterization, and Applications to Catalysis. *Acc. Chem. Res.* **2001**, *34*, 181-190.
13. Gomez, M. V.; Guerra, J.; Velders, A. H.; Crooks, R. M. NMR Characterization of Fourth-Generation PAMAM Dendrimers in the Presence and Absence of Palladium Dendrimer-Encapsulated Nanoparticles. *J. Am. Chem. Soc.* **2009**, *131*, 341-350.
14. Lin, S.; Diercks, C. S.; Zhang, Y.-B.; Kornienko, N.; Nichols, E. M.; Zhao, Y.; Paris, A. R.; Kim, D.; Yang, P.; Yaghi, O. M.; Chang, C. J. Covalent organic frameworks comprising cobalt porphyrins for catalytic CO₂ reduction in water. *Science* **2015**, *349*, 1208-1213.
15. Cortright, R. D.; Davda, R. R.; Dumesic, J. A. Hydrogen from catalytic reforming of biomass-derived hydrocarbons in liquid water. *Nature* **2002**, *418*, 964-967.
16. Xia, Y.; Xiong, Y.; Lim, B.; Skrabalak, S. E. Shape-Controlled Synthesis of Metal Nanocrystals: Simple Chemistry Meets Complex Physics? *Angew. Chem. Int. Ed* **2009**, *48*, 60-103.
17. Huang, W.; Kuhn, J. N.; Tsung, C.-K.; Zhang, Y.; Habas, S. E.; Yang, P.; Somorjai, G. A. Dendrimer Templated Synthesis of One Nanometer Rh and Pt Particles Supported on Mesoporous Silica: Catalytic Activity for Ethylene and Pyrrole Hydrogenation. *Nano Lett.* **2008**, *8*, 2027-2034.
18. Crooks, R. M.; Zhao, M. Dendrimer-Encapsulated Pt Nanoparticles: Synthesis, Characterization, and Applications to Catalysis. *Adv. Mater.* **1999**, *11*, 217-220.
19. Rebrov, E. A.; Leshchiner, I. D.; Muzafarov, A. M. Synthesis of Carbosilane Dendrimers with Variable Distance between Branching Nodes. *Macromolecules* **2012**, *45*, 8796-8804.
20. Zhao, D.; Feng, J.; Huo, Q.; Melosh, N.; Fredrickson, G. H.; Chmelka, B. F.; Stucky, G. D. Triblock Copolymer Syntheses of Mesoporous Silica with Periodic 50 to 300 Angstrom Pores. *Science* **1998**, *279*, 548-552.
21. Li, Y.; Liu, J. H.-C.; Witham, C. A.; Huang, W.; Marcus, M. A.; Fakra, S. C.; Alayoglu, P.; Zhu, Z.; Thompson, C. M.; Arjun, A.; Lee, K.; Gross, E.; Toste, F. D.; Somorjai, G. A.

A Pt-Cluster-Based Heterogeneous Catalyst for Homogeneous Catalytic Reactions: X-ray Absorption Spectroscopy and Reaction Kinetic Studies of Their Activity and Stability against Leaching. *J. Am. Chem. Soc.* **2011**, *133*, 13527-13533.
22. Ertl, G. Surface Science and Catalysis—Studies on the Mechanism of Ammonia Synthesis: The P. H. Emmett Award Address. *Catalysis Reviews* **1980**, *21*, 201-223.
23. Spencer, N. D.; Schoonmaker, R. C.; Somorjai, G. A. Iron single crystals as ammonia synthesis catalysts: Effect of surface structure on catalyst activity. *J. Catal.* **1982**, *74*, 129-135.
24. Torres Galvis, H. M.; Bitter, J. H.; Khare, C. B.; Ruitenbeek, M.; Dugulan, A. I.; de Jong, K. P. Supported Iron Nanoparticles as Catalysts for Sustainable Production of Lower Olefins. *Science* **2012**, *335*, 835-838.
25. Studt, F.; Sharafutdinov, I.; Abild-Pedersen, F.; Elkjær, C. F.; Hummelshøj, J. S.; Dahl, S.; Chorkendorff, I.; Nørskov, J. K. Discovery of a Ni-Ga catalyst for carbon dioxide reduction to methanol. *Nat. Chem.* **2014**, *6*, 320-324.
26. Witham, C. A.; Huang, W.; Tsung, C.-K.; Kuhn, J. N.; Somorjai, G. A.; Toste, F. D. Converting homogeneous to heterogeneous in electrophilic catalysis using monodisperse metal nanoparticles. *Nat. Chem.* **2010**, *2*, 36-41.
27. Schlögl, R.: Ammonia Synthesis. In *Handbook of Heterogeneous Catalysis*; Wiley-VCH Verlag GmbH & Co. KGaA, 2008.
28. Gross, E.; Liu, J. H.-C.; Toste, F. D.; Somorjai, G. A. Control of selectivity in heterogeneous catalysis by tuning nanoparticle properties and reactor residence time. *Nat. Chem.* **2012**, *4*, 947-952.
29. Ye, R.; Yuan, B.; Zhao, J.; Ralston, W. T.; Wu, C.-Y.; Unel Barin, E.; Toste, F. D.; Somorjai, G. A. Metal Nanoparticles Catalyzed Selective Carbon–Carbon Bond Activation in the Liquid Phase. *J. Am. Chem. Soc.* **2016**, *138*, 8533-8537.
30. Ye, R.; Zhao, J.; Yuan, B.; Liu, W.-C.; Rodrigues De Araujo, J.; Faucher, F. F.; Chang, M.; Deraedt, C. V.; Toste, F. D.; Somorjai, G. A. New Insights into Aldol Reactions of Methyl Isocyanoacetate Catalyzed by Heterogenized Homogeneous Catalysts. *Nano Lett.* **2017**, *17*, 584-589.
31. Huang, W.; Liu, J. H.-C.; Alayoglu, P.; Li, Y.; Witham, C. A.; Tsung, C.-K.; Toste, F. D.; Somorjai, G. A. Highly Active Heterogeneous Palladium Nanoparticle Catalysts for Homogeneous Electrophilic Reactions in Solution and the Utilization of a Continuous Flow Reactor. *J. Am. Chem. Soc.* **2010**, *132*, 16771-16773.
32. Gross, E.; Shu, X.-Z.; Alayoglu, S.; Bechtel, H. A.; Martin, M. C.; Toste, F. D.; Somorjai, G. A. In Situ IR and X-ray High Spatial-Resolution Microspectroscopy Measurements of Multistep Organic Transformation in Flow Microreactor Catalyzed by Au Nanoclusters. *J. Am. Chem. Soc.* **2014**, *136*, 3624-3629.
33. Deraedt, C.; Melaet, G.; Ralston, W. T.; Ye, R.; Somorjai, G. A. Platinum and Other Transition Metal Nanoclusters (Pd, Rh) Stabilized by PAMAM Dendrimer as Excellent

Heterogeneous Catalysts: Application to the Methylcyclopentane (MCP) Hydrogenative Isomerization. *Nano Lett.* **2017**, *17*, 1853-1862.
34. Chen, P.-C.; Liu, X.; Hedrick, J. L.; Xie, Z.; Wang, S.; Lin, Q.-Y.; Hersam, M. C.; Dravid, V. P.; Mirkin, C. A. Polyelemental nanoparticle libraries. *Science* **2016**, *352*, 1565-1569.
35. Ciriminna, R.; Falletta, E.; Della Pina, C.; Teles, J. H.; Pagliaro, M. Industrial Applications of Gold Catalysis. *Angew. Chem. Int. Ed* **2016**, *55*, 14210-14217.
36. Wang, H.; Rempel, G. L. Bimetallic Dendrimer-encapsulated Nanoparticle Catalysts. *Polym. Rev. (Philadelphia, PA, U. S.)* **2016**, *56*, 486-511.
37. Puntes, V. F.; Krishnan, K. M.; Alivisatos, A. P. Colloidal Nanocrystal Shape and Size Control: The Case of Cobalt. *Science* **2001**, *291*, 2115-2117.
38. Wu, C.-Y.; Wolf, W. J.; Levartovsky, Y.; Bechtel, H. A.; Martin, M. C.; Toste, F. D.; Gross, E. High-spatial-resolution mapping of catalytic reactions on single particles. *Nature* **2017**, *541*, 511-515.

Chapter 4 - Metal Nanoparticles Catalyzed Selective Carbon–Carbon Bond Activation in the Liquid Phase

(This chapter covers similar material as in Ye, R.; Yuan, B.; Zhao, J.; Ralston, W. T.; Wu, C.-Y.; Unel Barin, E.; Toste, F. D.; Somorjai, G. A. *J. Am. Chem. Soc.* **2016,** *138*, 8533-8537.– reproduced with permission, copyright 2016 American Chemical Society.)

Abstract

Understanding the C–C bond activation mechanism is essential for developing the selective production of hydrocarbons in the petroleum industry and for selective polymer decomposition. In this work, ring-opening reactions of cyclopropane derivatives under hydrogen catalyzed by metal nanoparticles (NPs) in the liquid phase were studied. 40-atom rhodium (Rh) NPs, encapsulated by dendrimer molecules and supported in mesoporous silica, catalyzed the ring opening of cyclopropylbenzene at room temperature under hydrogen in benzene, and the turnover frequency (TOF) was higher than other metals or the Rh homogeneous catalyst counterparts. Comparison of reactants with various substitution groups showed that electron donation on the three-membered ring boosted the TOF of ring opening. The linear products formed with 100% selectivity for ring opening of all reactants catalyzed by the Rh NP. Surface Rh(0) acted as the active site in the NP. The capping agent played an important role in the ring-opening reaction kinetics. Larger particle size tended to show higher TOF and smaller reaction activation energy for Rh NPs encapsulated in either dendrimer or poly(vinylpyrrolidone). The generation/size of dendrimer and surface group also affected the reaction rate and activation energy.

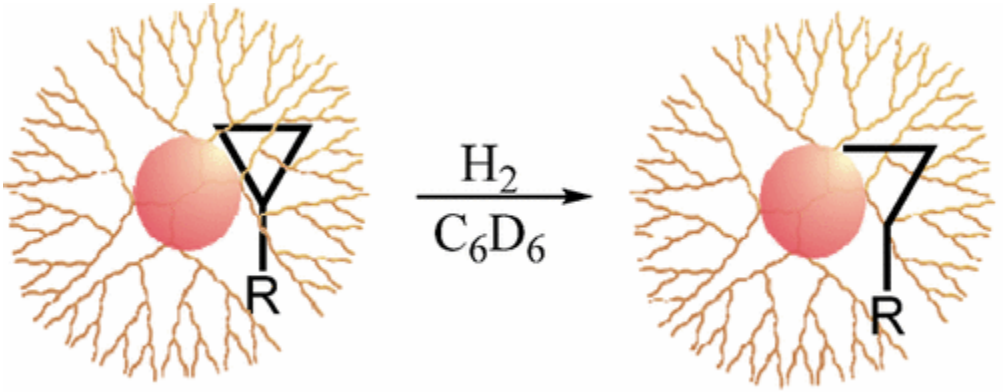

Bond lengths were not drawn to scale.

4.1 Introduction

Carbon−carbon (C−C) bond activation in the gas phase plays an important role in the chemical industry. Cracking and reforming reactions in crude oil refineries practice C−C bond activation on a large scale daily.[1] Polyethylene and polypropylene are currently the mostly widely used plastics, but their decomposition requires thermal C−C bond activation.[2] Due to thermodynamic and kinetic considerations, selective C−C bond activation is challenging.[3-6] Currently, these reactions are operated at high temperatures in industry (above 600 K). Undifferentiated thermal activation of C−C bond leads to multiple product formation simultaneously, requiring further product separation.

To overcome the low reactivity of C−C bonds, a practical strategy is to exploit the ring strain of (three- or four-membered) cyclic compounds as a driving force, thereby allowing the study of the factors controlling catalyst activity and selectivity. Early work[7,8] showed that catalytic cyclopropane hydrogenation (ring opening) by metal single crystal or powder catalysts in the gas phase was often accompanied by hydrogenolysis, forming smaller molecules. It was posited that the reaction mechanism was metal-dependent, proceeding through different intermediates including a monoadsorbed radical,[9] 1,3-diadsorbed species on Ni catalysts[10] or metallocycle intermediate on Pt.[11]

In order to improve the product selectivity, efforts have been made to study C−C bond activation reactions using metal complexes of Rh,[12-16] Pt,[17] Pd,[18] Cu,[19] and other metals[20,21] in solution under relatively mild conditions. For example, Bart and Chirik[14] recently reported examples of ring opening of cyclopropane derivatives catalyzed by organometallic Rh catalysts in the liquid phase and proposed the rhodium−metallocycle as the intermediate.

In this work, the advantages of both types of catalysis on the ring-opening reaction are combined: the high activity of heterogeneous catalysts and the high selectivity of homogeneous catalysts. We investigated the effect of different variables on the metal nanoparticles (NPs) catalyzed C−C bond activation in the liquid phase. Rh NPs catalyzed the ring opening of cyclopropylbenzene (**1**) at room temperature under an atmospheric pressure of H_2. The turnover frequency (TOF) of the reaction was correlated with reactant and metal NP properties, and the factors governing the catalytic activity and selectivity were analyzed.

4.2 Results and discussion

4.2.1 Catalyst screening

The catalytic ring opening of **1** in the presence of H_2 was used as a model reaction to study the C−C bond activation reaction under mild conditions. The TOF of several potential catalysts for ring-opening reactions under atmospheric pressure of hydrogen in C_6D_6 was explored at 20 and 80 °C (Table 1). TOF of metal NPs was calculated by the number of molecules reacted in unit time (an hour) divided by the number of undercoordinated metal atoms, which was estimated from simple hard-sphere

counting models.[22] 40-atom NPs of Rh, Pd, and Au encapsulated by fourth-generation polyamidoamine (PAMAM) dendrimer with hydroxyl terminal groups (G4OH) were synthesized and loaded into mesoporous silica SBA-15[23-26] (Entry 1-3 in Table 1). Among these three catalysts, Rh_{40}/G4OH/SBA-15 offered the highest TOF at room temperature. Pd NPs were less active catalysts than Rh NPs at room temperature, but were more active at elevated temperature. The Au NPs showed very low activity as catalysts for this reaction. Rh(I) complexes such as the Wilkinson's catalyst $(PPh_3)_3RhCl$ and $[Rh(CO)_2Cl]_2$ had lower TOF compared to the Rh NPs. $(PPh_3)_3RhCl$ at 80 °C was the only case in Table 1 where the branch product cumene formed along with the linear product propylbenzene (branch:linear ratio about 1:2). Rh(III) compounds $RhCl_3$ or $Rh(acac)_3$ failed to catalyze the reaction. Oxidizing Rh in Rh_{40}/G4OH/SBA-15 by adding an organic oxidizer $PhICl_2$ completely inhibited the activity of the catalyst (entry 6 in Table 1). Pure mesoporous SBA-15 could not catalyze the reaction, which could be considered as the blank reaction. On the other hand, solid acids, such as H^+-Al-SBA-15 (acidified mesoporous silica SBA-15) and H^+-MFI (acidified mesoporous MFI zeolite), catalyzed the rearrangement of **1** to form only (*E*)-prop-1-en-1-ylbenzene at 80 °C without formation of propylbenzene, but they were inactive at room temperature. Rh_{40}/G4OH/SBA-15 also catalyzed the reaction in other solvents (toluene, dichloromethane and methanol) with similar TOF to that in benzene.

Table 1. Catalytic ring opening of cyclopropylbenzene (1) with various catalysts under 1 atm of H_2 in C_6D_6

Entry	Catalyst	TOF (h^{-1})[a] at 20 °C	TOF (h^{-1})[a] at 80 °C
1	Rh_{40}/G4OH/SBA-15	2.24	11.4
2	Pd_{40}/G4OH/SBA-15	1.70	22.1
3	Au_{40}/G4OH/SBA-15	0	0.20
4	$(PPh_3)_3RhCl$	0.10	0.38[b]
5	$[Rh(CO)_2Cl]_2$	0	0.10
6	Rh_{40}/G4OH/SBA-15 + $PhICl_2$	0	0

[a] Numbers of active sites for TOF calculation are estimated from simple hard-sphere counting models. [b] This is the sum TOF for the formation of linear and branch products.

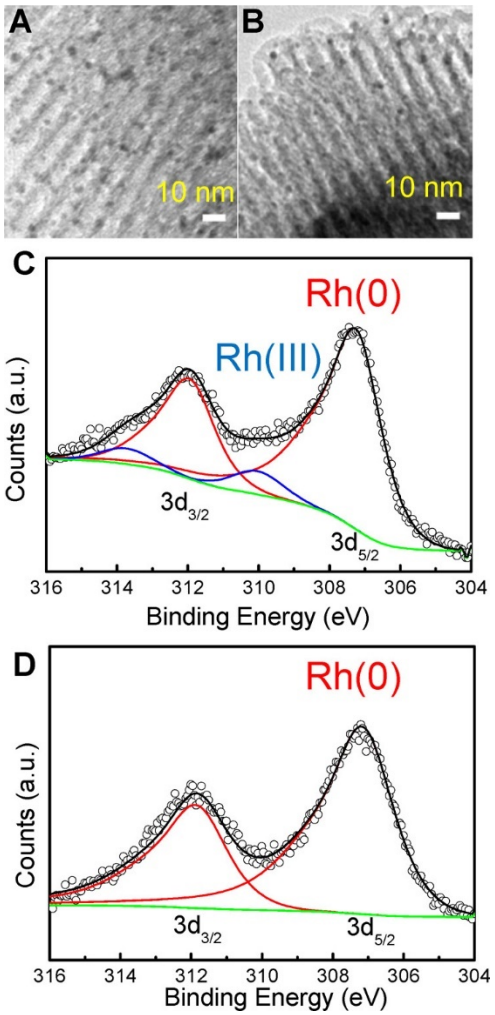

Figure 1. Characterization of Rh_{40}/G4OH/SBA-15. TEM images of the sample before (A) and after (B) three cycles of reactions. The scale bars are 10 nm. (C) and (D) Corresponding XPS spectra. XPS spectra are not normalized.

4.2.2 Characterization of Rh_{40}/G4OH/SBA-15

TEM images of Rh_{40}/G4OH/SBA-15 before and after three cycles of reactions with **1** are shown in Figure 1A, B, respectively. The size of Rh NPs was 1.6 ± 0.2 nm by averaging over 100 particles. The NPs were stable after three cycles of reactions. No leaching was observed, as confirmed by the inductively coupled plasma optical emission spectrometry of the filtrate of the reaction mixture. Hydrogenolysis was not observable during the reaction, which was confirmed by the absence of small gas molecules in the headspace (the gas above the product solution) GC analysis. The mass balance (total amount of product and unreacted reactant after the reaction matched the amount of reactant before the reaction) provides additional support for the lack of hydrogenolysis.

The rate of ring opening of **1** in the second and third cycle of the recycled catalyst was 97% and 96% of that in the first cycle, respectively. The as-synthesized Rh_{40}/G4OH/SBA-15 sample contained surface rhodium oxide species, according to the XPS spectrum (Figure 1C). The oxidation state of Rh after the reaction was purely 0, as shown by the 307.3 eV binding energy[24] in the XPS spectrum (Figure 1D). To explore the effects of these rhodium oxides on the kinetics of the ring opening reaction, a set of control experiments with different pretreatment conditions were performed. Keeping all other variables the same, one catalyst was mixed with H_2 at 100 °C for 24 h, one was mixed with Ar at 100 °C for 24 h, and the other without pretreatment. When these three catalysts were used in the reaction at 20 °C, they exhibited the same reaction rate/TOF on the ring opening of **1**. This implies that the reduction of the surface rhodium oxides to metallic rhodium was a fast process under reaction conditions.

Scheme 1. Reactants for ring opening reactions catalyzed by Rh_{40}/G4OH/SBA-15 and the TOF under specified reaction condition.

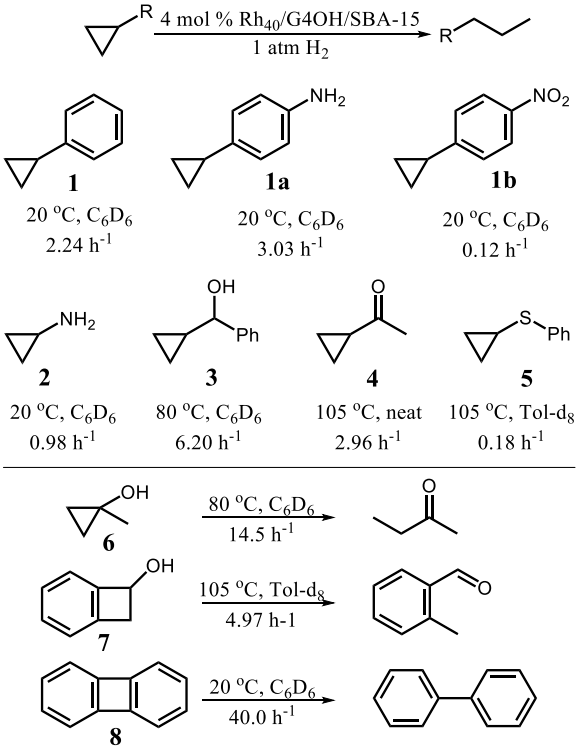

4.2.3 Applications on other cyclic compounds

Reactants that underwent the ring-opening reaction catalyzed by Rh_{40}/G4OH/SBA-15 are listed in Scheme 1 along with the TOF values under the specified conditions. Under the same reaction condition, the more electron-rich **1a**

reacted faster than **1**, but reaction of electron-deficient **1b** was notably slower. It should be noted that a small amount of **1b** was reduced to **1a** during the reaction process, and the TOF reported for **1b** does not discount this pathway. Thus, the real TOF of **1b** ring-opening reaction is even smaller. The observation that ring opening was accelerated by electron-donating and decelerated by electron-withdrawing groups on the phenyl ring of the reactant is consistent with a hypothesis that a cationic intermediate is involved in the rate-limiting step of the reaction. This hypothesis held for molecules without phenyl rings. Rings attached to electron-donating groups opened quickly at a low temperature, while those attached to electron-withdrawing groups required higher temperatures to exhibit an observable reaction rate of C−C bond scission.

The TOF values in Scheme 1 were measured at various temperatures, which was a compromise of the low reaction rate at a low temperature and reactant/solvent boiling at a high temperature. Reactants **6** and **7**, rings attached to a hydroxyl group, underwent the ring-opening reaction with the hydroxyl group transformed to a carbonyl group. The formation of a C=O bond, which was not further hydrogenated under the reaction condition, provided an additional driving force for the ring-opening reaction. Thus, the TOF of **6** was high, and the typically inert four-membered ring in **7** was activated. In another example of four-membered ring C−C bond activation, biphenylene (**8**) was transformed to biphenyl at room temperature, a reaction for which homogeneous catalysts typically required elevated temperatures.[17]

The products from reactants **1**−**5** in Scheme 1 were entirely the linear/proximal ones. In contrast, Bart and Chirik[14] reported that the branch/distal products were favored by homogeneous Rh catalysts, unless a reactant with the ability to chelate with the Rh catalyst was used. The unique selectivity toward linear products by NPs in this work is likely attributed to a different reaction mechanism between the reported homogeneous catalysts and NP catalysts employed in this work.

4.2.4 Kinetics study of the ring opening reaction of 1

The size of dendrimer encapsulated NPs was tuned by modifying the Rh:G4OH ratio during the NP synthesis. Rh_{15}G4OH, Rh_{40}G4OH, and Rh_{50}G4OH were synthesized to explore the size effects of Rh NPs on the catalytic performance. However, synthesis of even larger sizes of G4OH-encapsulated NPs was limited to 4.5 nm in diameter by the size of G4OH. Figure 2A displays the temperature dependence of the ring opening TOF of **1** catalyzed by Rh NPs between 293 and 333 K in C_6D_6 under 1 atm of H_2. TOF increased as temperature increased for the same catalyst as expected. Further control experiments (data not reflected in the figure) with faster stirring rates gave the same TOF, suggesting that the reactions were not limited by diffusion under these reaction conditions. The apparent activation energy of ring opening catalyzed by each catalyst was determined from the slopes of the linear fit plots and plotted in Figure 2C. Keeping

everything else constant, increasing the size of Rh NPs from 0.8 to 2.1 nm increased the TOF from 2.4 to 13.4 h^{-1} (at 333 K) and decreased the reaction activation energy from 29.8 to 17.7 kJ/mol. The trend that larger particle size offered higher TOF has been previously observed in the catalytic hydrogenation of allyl alcohol[27] and alkynol[28] and dehydrogenation of ammonia borane.[29] The same size dependence of TOF and activation energy held for the hydrogenation of styrene, an example of C−C π-bond hydrogenation.

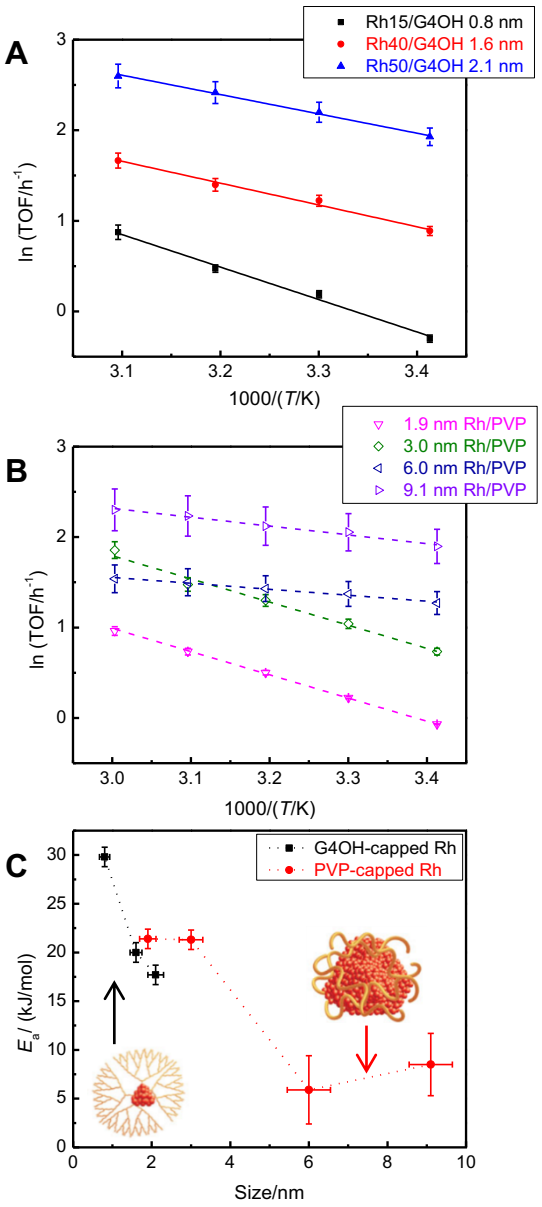

Figure 2. Arrhenius plots of ring-opening of **1** in C_6D_6 under H_2, catalyzed by Rh NPs of various sizes encapsulated in (A) G4OH and (B) PVP. (C) Plots of particle size and

calculated ring opening activation energy catalyzed by Rh NPs. The cartoons of dendrimer encapsulated NPs and PVP-capped NPs were shown in the bottom left and top right, respectively.

On the basis of these observations, we hypothesized that the increased abundance of Rh−Rh bond on the surface of larger Rh NPs led to their higher catalytic activity. We tested the hypothesis with Rh NPs of various sizes encapsulated in polyvinylpyrrolidone (PVP). The Arrhenius plots of ring opening of **1** catalyzed by Rh/PVP NPs were shown in Figure 2B. The size effects of PVP capped NPs were the same as G4OH capped NPs. Here, the large Rh/PVP NPs (6.0 and 9.1 nm) had only a small percentage of undercoordinated surface atoms. With comparable amount of Rh loading, reactions catalyzed by large NPs had lower yield, due to scarcity of surface Rh atom, leading to a relatively large measurement error of TOF by NMR.

As shown in Figure 2C, comparing 2 nm Rh NPs capped by G4OH and PVP, the former had greater TOF. There were several possible reasons for this observation: (1) steric effect, the capping agent might block a portion of undercoordinated Rh atoms due to steric hindrance ; (2) electronic effect, the interaction of the capping agent might tune the electronic structure of the Rh atoms, and thus affected the energetics of the reaction process.

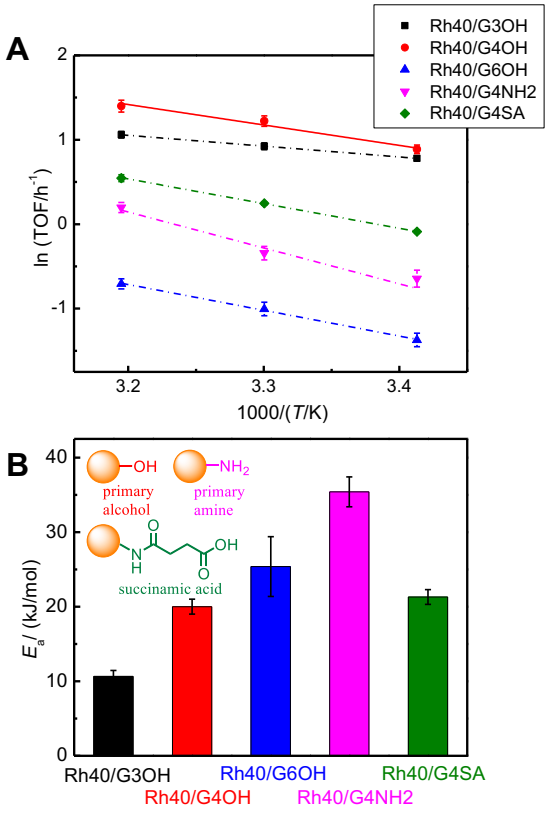

Figure 3. (A) Arrhenius plots of ring opening of **1** in C_6D_6 under H_2, catalyzed by Rh NPs with different generation number of dendrimer (G3OH, G4OH, and G6OH), and G4 dendrimer with surface groups of primary amine ($G4NH_2$) or succinamic acid (G4SA). (B) Calculated ring-opening activation energy catalyzed by the corresponding Rh NPs. Inset shows the structure of dendrimer surface groups used.

In order to elucidate the effects of the capping agent, Rh NPs encapsulated in different dendrimers were synthesized. Third-generation G3OH and sixth-generation G6OH were used in order to vary the size of the dendrimer without changing its chemical properties. The impact of the chemical properties of the dendrimer support was studied by replacing the terminal hydroxyl group in G4OH with primary amine and succinamic acid (SA) groups by using $G4NH_2$ and G4SA, respectively. Rh NPs were synthesized with these dendrimers, keeping the same amount of Rh and the Rh:dendrimer ratio as 40:1. TEM images of these Rh NPs indicated that the sizes were constant within error. Arrhenius plots of ring opening of **1** catalyzed by these NPs are given in Figure 3A, and the corresponding activation energy in Figure 3B. Modifying the dendrimer generation from G3OH to G6OH, the rate of ring opening tended to decrease and the corresponding activation energy generally increased, likely due to the steric effect. $G4NH_2$ and G4OH had similar size but distinct Lewis and Brønsted basicity, so the lower activity of $Rh_{40}/G4NH_2$ might result from an electronic effect. Both G4OH and G4SA have 64 surface groups, but −SA is much bulkier than −OH as shown in Figure 3B. Rh_{40}/G4SA showed smaller TOF than Rh_{40}/G4OH, mainly caused by the steric effects.

4.3 Experimental section

4.3.1 Chemicals.

Unless otherwise noted, all commercial materials were used without purification and used as received. Thin-layer chromatography (TLC) analysis of reaction mixtures was performed using Merck silica gel 60 F254 TLC plates, and visualized under UV or by staining with ceric ammonium molybdate or $KMnO_4$ dip. Flash column chromatography was carried out on Merck Silica Gel 60 Å, 230 × 400 mesh. All glassware was dried at 100 °C for 8 h before use.

Rhodium(III) chloride hydrate ($RhCl_3 \cdot xH_2O$, ⩾99.9% trace metals basis), Rhodium(III) acetylacetonate ($Rh(acac)_3$, 97%), Tris(triphenylphosphine)rhodium(I) chloride (99.9% trace metals basis), Di-μ-chloro-tetracarbonyldirhodium(I) ($[Rh(CO)_2Cl]_2$, 97%), Potassium palladium(II) chloride (K_2PdCl_4,98%), Sodium borohydride ($NaBH_4$, 98%), poly(vinylpyrrolidone) (PVP, 55K), 1,4-butanediol (99%), sodium citrate (>99.0%), Pluronic P123, tetraethylorthosilicate (TEOS, 99.999%), cyclopropylbenzene (97%), mesitylene (98%), cyclopropylamine (**2**, 98%), α-cyclopropylbenzyl alcohol (**3**, 99%), 1-methylcyclopropanol (**6**), biphenylene (**8**, 99%), cyclopropylboronic acid, 1-bromo-4-nitrobenzene (99%), tricyclohexyl phosphine, potassium phosphate tribasic

(⩾98%), palladium(II) acetate (98%), platinum(IV) oxide, and aluminum chloride were purchased from Sigma-Aldrich. All PAMAM dendrimers, G3OH, G4OH, G6OH, G4NH_2, and G4SA were purchased from Dendritech Inc. as water solutions. Cyclopropyl methyl ketone (**4**, 99%), cyclopropyl phenyl sulfide (**5**, 98+%) were purchased from Alfa Aesar. Hydrogen tetrachloroaurate(III) hydrate (99.9985%-Au) were purchased from STREM. Benzene-d_6 and Toluene-d_8 were purchased from Cambridge Isotope Laboratories, Inc. Other chemicals used include 1-Hydroxybenzocyclobutene (**7**, 98%, Astatech Inc.), hydrochloric acid (HCl, Fisher Chemical), anhydrous solvents ethanol, tetrahydrofuran, ethyl acetate, toluene, and acetonitrile.

4.3.2 Representative procedure for catalytic reactions.

To a dry 10 mL Schlenk flask, equipped with a stir bar, was added cyclopropylbenzene (8.9 mg, 0.075 mmol), Rh_{40}/G4OH/SBA-15 (50 mg, 0.003 mmol, 4 mol%), mesitylene (2.3 μL, internal standard, Aldrich) and benzene-d_6 (1 mL). The reaction mixture was degassed, placed under 1 atm of H_2 and heated with stirring at the desired temperature for 2 hours. The mixture was then cooled to room temperature and the solid catalyst filtered using a polytetrafluoroethylene syringe filter. The filtrate was transferred to a NMR tube for analysis. The conversions were controlled to be low (typically between 5-20%) to allow assessment of the initial rates.

4.4 Conclusions

The ring opening reactions of cyclopropane derivatives catalyzed by metal NPs under hydrogen were investigated. Rh_{40}/G4OH/SBA-15 showed a TOF of 2.24 h^{-1}, which was higher than the homogeneous counterparts, toward the ring opening of cyclopropylbenzene at room temperature. This catalyst was stable and could be recycled at least three times. The reaction was accelerated by electron-donating groups on the three-membered ring, while electron-accepting groups decreased the TOF. In contrast to ring-opening reactions catalyzed by homogeneous rhodium catalysts, the products of the NP catalyzed reactions were 100% linear. The apparent activation energy of the reaction was affected by the catalyst properties. For Rh NPs encapsulated in G4OH and PVP, larger particle size tends to show higher TOF and smaller reaction activation energy. For dendrimer encapsulated Rh NPs, both the dendrimer surface group and the dendrimer generation played a role in the reaction rate and activation energy of ring opening. The study sheds light on the fundamental factors controlling C−C bond activation activity and selectivity.

4.5 Reference

1. Gary, J. H.; Handwerk, G. E.; Kaiser, M. J.: *Petroleum refining: technology and economics*; CRC press, 2007.

2. Beyler, C. L.; Hirschler, M. M. Thermal decomposition of polymers. *SFPE handbook of fire protection engineering* **2002**, *2*, 110-131.

3. Jun, C.-H. Transition metal-catalyzed carbon-carbon bond activation. *Chem. Soc. Rev.* **2004**, *33*, 610-618.
4. Ruhland, K. Transition-Metal-Mediated Cleavage and Activation of C–C Single Bonds. *Eur. J. Org. Chem.* **2012**, *2012*, 2683-2706.
5. Souillart, L.; Cramer, N. Catalytic C–C Bond Activations via Oxidative Addition to Transition Metals. *Chem. Rev.* **2015**, *115*, 9410-9464.
6. Rybtchinski, B.; Milstein, D. Metal Insertion into C−C Bonds in Solution. *Angew. Chem. Int. Ed* **1999**, *38*, 870-883.
7. Bond, G. C.: Hydrogenation of Small Alicyclic Rings. In *Metal-Catalysed Reactions of Hydrocarbons*; Springer US: Boston, MA, 2005; pp 473-500.
8. Kahn, D. R.; Petersen, E. E.; Somorjai, G. A. The hydrogenolysis of cyclopropane on a platinum stepped single crystal at atmospheric pressure. *J. Catal.* **1974**, *34*, 294-306.
9. Newham, J. The Catalytic Hydrogenolysis of Small Carbon Rings. *Chem. Rev.* **1963**, *63*, 123-137.
10. Sridhar, T. S.; Ruthven, D. M. The kinetics and mechanism of the catalytic hydrogenation of cyclopropane. *J. Catal.* **1972**, *24*, 153-160.
11. Capitano, A. T.; Gabelnick, A. M.; Gland, J. L. Catalytic Cyclopropane Hydrogenation on Platinum(111) Using In Situ Soft X-ray Methods. *J. Phys. Chem. B* **2000**, *104*, 3337-3342.
12. Gozin, M.; Weisman, A.; Ben-David, Y.; Milstein, D. Activation of a carbon-carbon bond in solution by transition-metal insertion. *Nature* **1993**, *364*, 699-701.
13. Murakami, M.; Takahashi, K.; Amii, H.; Ito, Y. Rhodium(I)-Catalyzed Successive Double Cleavage of Carbon−Carbon Bonds of Strained Spiro Cyclobutanones. *J. Am. Chem. Soc.* **1997**, *119*, 9307-9308.
14. Bart, S. C.; Chirik, P. J. Selective, Catalytic Carbon−Carbon Bond Activation and Functionalization Promoted by Late Transition Metal Catalysts. *J. Am. Chem. Soc.* **2003**, *125*, 886-887.
15. Ishida, N.; Sawano, S.; Masuda, Y.; Murakami, M. Rhodium-Catalyzed Ring Opening of Benzocyclobutenols with Site-Selectivity Complementary to Thermal Ring Opening. *J. Am. Chem. Soc.* **2012**, *134*, 17502-17504.
16. Shaw, M. H.; Melikhova, E. Y.; Kloer, D. P.; Whittingham, W. G.; Bower, J. F. Directing Group Enhanced Carbonylative Ring Expansions of Amino-Substituted Cyclopropanes: Rhodium-Catalyzed Multicomponent Synthesis of N-Heterobicyclic Enones. *J. Am. Chem. Soc.* **2013**, *135*, 4992-4995.
17. Edelbach, B. L.; Vicic, D. A.; Lachicotte, R. J.; Jones, W. D. Catalytic Hydrogenolysis of Biphenylene with Platinum, Palladium, and Nickel Phosphine Complexes. *Organometallics* **1998**, *17*, 4784-4794.
18. Trost, B. M.; Morris, P. J.; Sprague, S. J. Palladium-Catalyzed Diastereo- and Enantioselective Formal [3 + 2]-Cycloadditions of Substituted Vinylcyclopropanes. *J. Am. Chem. Soc.* **2012**, *134*, 17823-17831.

19. Tang, C.; Jiao, N. Copper-Catalyzed Aerobic Oxidative C C Bond Cleavage for C N Bond Formation: From Ketones to Amides. *Angew. Chem. Int. Ed* **2014**, *53*, 6528-6532.
20. Ogoshi, S.; Nagata, M.; Kurosawa, H. Formation of Nickeladihydropyran by Oxidative Addition of Cyclopropyl Ketone. Key Intermediate in Nickel-Catalyzed Cycloaddition. *J. Am. Chem. Soc.* **2006**, *128*, 5350-5351.
21. Dieskau, A. P.; Holzwarth, M. S.; Plietker, B. Fe-Catalyzed Allylic C–C-Bond Activation: Vinylcyclopropanes As Versatile a1,a3,d5-Synthons in Traceless Allylic Substitutions and [3 + 2]-Cycloadditions. *J. Am. Chem. Soc.* **2012**, *134*, 5048-5051.
22. McClure, S. M.; Lundwall, M. J.; Goodman, D. W. Planar oxide supported rhodium nanoparticles as model catalysts. *Proc. Natl. Acad. Sci. U. S. A.* **2011**, *108*, 931-936.
23. Crooks, R. M.; Zhao, M. Dendrimer-Encapsulated Pt Nanoparticles: Synthesis, Characterization, and Applications to Catalysis. *Adv. Mater.* **1999**, *11*, 217-220.
24. Huang, W.; Kuhn, J. N.; Tsung, C.-K.; Zhang, Y.; Habas, S. E.; Yang, P.; Somorjai, G. A. Dendrimer Templated Synthesis of One Nanometer Rh and Pt Particles Supported on Mesoporous Silica: Catalytic Activity for Ethylene and Pyrrole Hydrogenation. *Nano Lett.* **2008**, *8*, 2027-2034.
25. Witham, C. A.; Huang, W.; Tsung, C.-K.; Kuhn, J. N.; Somorjai, G. A.; Toste, F. D. Converting homogeneous to heterogeneous in electrophilic catalysis using monodisperse metal nanoparticles. *Nat. Chem.* **2010**, *2*, 36-41.
26. Gross, E.; Liu, J. H.-C.; Toste, F. D.; Somorjai, G. A. Control of selectivity in heterogeneous catalysis by tuning nanoparticle properties and reactor residence time. *Nat. Chem.* **2012**, *4*, 947-952.
27. Wilson, O. M.; Knecht, M. R.; Garcia-Martinez, J. C.; Crooks, R. M. Effect of Pd Nanoparticle Size on the Catalytic Hydrogenation of Allyl Alcohol. *J. Am. Chem. Soc.* **2006**, *128*, 4510-4511.
28. Crespo-Quesada, M.; Yarulin, A.; Jin, M.; Xia, Y.; Kiwi-Minsker, L. Structure Sensitivity of Alkynol Hydrogenation on Shape- and Size-Controlled Palladium Nanocrystals: Which Sites Are Most Active and Selective? *J. Am. Chem. Soc.* **2011**, *133*, 12787-12794.
29. Chen, W.; Ji, J.; Feng, X.; Duan, X.; Qian, G.; Li, P.; Zhou, X.; Chen, D.; Yuan, W. Mechanistic Insight into Size-Dependent Activity and Durability in Pt/CNT Catalyzed Hydrolytic Dehydrogenation of Ammonia Borane. *J. Am. Chem. Soc.* **2014**, *136*, 16736-16739.

Chapter 5 - New Insights into Aldol Reactions of Methyl Isocyanoacetate Catalyzed by Heterogenized Homogeneous Catalysts

(This chapter covers similar material as in Ye, R.; Zhao, J.; Yuan, B.; Liu, W.-C.; Rodrigues De Araujo, J.; Faucher, F. F.; Chang, M.; Deraedt, C. V.; Toste, F. D.; Somorjai, G. A. *Nano. Lett.* **2017**, *17*, 584-589. – reproduced with permission, copyright 2017 American Chemical Society.)

Abstract

The Hayashi–Ito aldol reaction of methyl isocyanoacetate (MI) and benzaldehydes, a classic homogeneous Au(I)-catalyzed reaction, was studied with heterogenized homogeneous catalysts. Among dendrimer encapsulated nanoparticles (NPs) of Au, Pd, Rh, or Pt loaded in mesoporous supports and the homogeneous analogues, the Au NPs led to the highest yield and highest diastereoselectivity of products in toluene at room temperature. The Au catalyst was stable and was recycled for at least six runs without substantial deactivation. Moreover, larger pore sizes of the support and the use of a hydrophobic solvent led to a high selectivity for the trans diastereomer of the product. The activation energy is sensitive to neither the size of Au NPs nor the support. A linear Hammett plot was obtained with a positive slope, suggesting an increased electron density on the carbonyl carbon atom in the rate-limiting step. IR studies revealed a strong interaction between MI and the gold catalyst, supporting the proposed mechanism, in which rate-limiting step involves an electrophilic attack of the aldehyde on the enolate formed from the deprotonated MI.

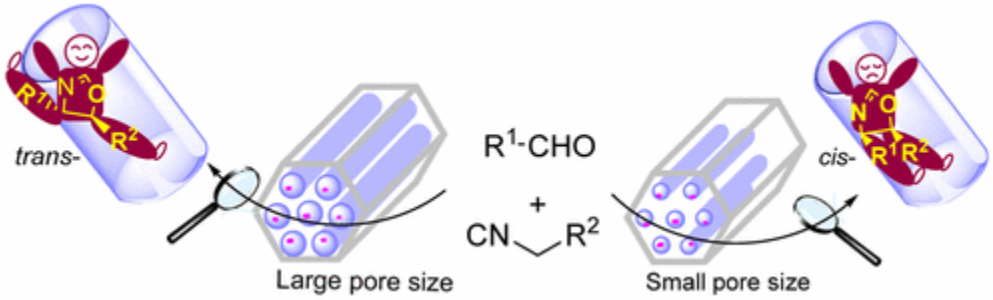

5.1 Introduction

Heterogeneous catalysis offers the benefit of easy separation of the catalyst from reaction mixtures.[1] For reactions reaching nearly 100% conversion, the filtration of the catalyst is the only necessary work-up, besides solvent removal (if any). In addition, heterogeneous catalysts can be applied to flow reactions,[2] and easily recycled.[3] These economically and ecologically beneficial aspects of heterogeneous catalysts are in agreement with the concepts of green chemistry. However, optimizing the product selectivity in traditional heterogeneous catalysts remains an important challenge.[4] Improvements in supported metal catalysts have predominantly focused on engineering the metal sites.[5-12] The solid support is also an important consideration in the design of a heterogeneous catalyst.[13] Strong metal-support interactions (SMSI), where the support greatly affects the *activity* of active sites,[14] are a good example of this phenomenon. However, the effects of the support properties on the product *selectivity* have not been thoroughly studied.[15-17]

The last two decades have seen numerous advances in gold catalysis.[16-23] Since the first publication by Ito et al., the aldol reaction of methyl isocyanoacetate (MI) and aldehydes forming 2-oxazolines has stood as a milestone in catalytic asymmetric synthesis.[24] Later, this reaction was widely studied with gold-based[25,26] and other[27] homogeneous catalysts in order to explore its synthetic scope, reaction mechanism and the effect of the ligand structure on selectivity. For example, Togni and Pastor[28] provided valuable insights into the reaction mechanism, the rate-determining step and the enantiodeterming transition states of Au(I)-complex-catalyzed aldol reaction through NMR, kinetic isotope, and linear free energy studies. Recently, van Koten et al.[29] immobilized Pd(II) complexes with pincer ligands[30] on mesoporous silica SBA-15 as a heterogenized homogeneous catalyst for the aldol reaction of MI and benzaldehyde in the presence of a base. Even though good activity and recycling results were achieved, the *trans* product selectivity was limited to 84%. Herein, we describe bridging the advantages of heterogeneous and homogeneous catalysts using dendrimer-supported heterogenized homogeneous catalyst developed in our group.[31-36] Additionally, the reaction mechanism of the aldol reaction was investigated, providing insights into the factors that affect the product selectivity in the heterogeneous reaction.

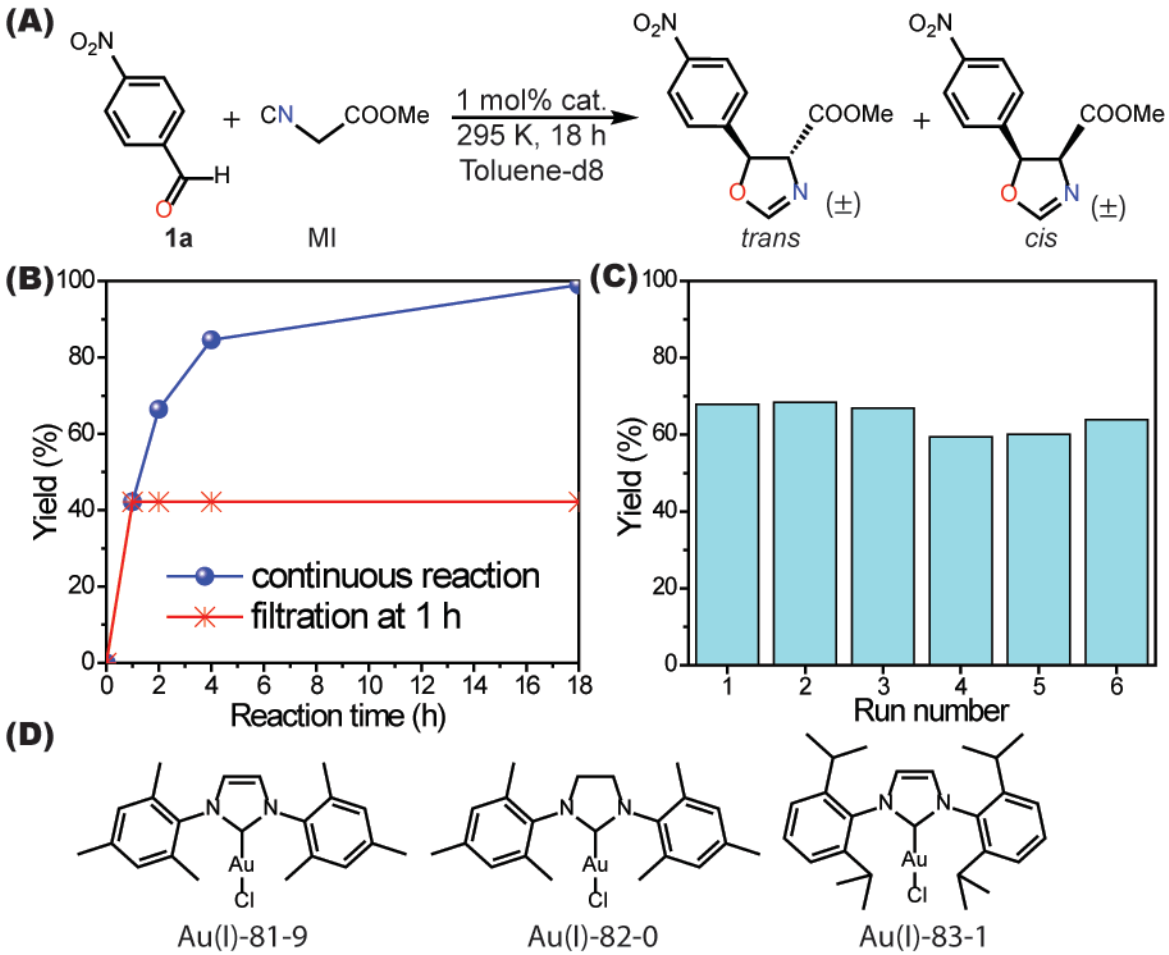

Figure 1. (A) A scheme of the aldol reaction. (B) The kinetics of the aldol reaction: 1 mol% catalyst, 22 °C in toluene. (C) Recycle tests with the same batch of Au_{40}/G4OH/MP-SBA-15 for six runs: 1 mol% catalyst in chloroform, 22 °C, 2 h per run. (D) Structures of Au(I)-complexes used in this study. The codes originate from their corresponding CAS numbers.

5.2 Experiments and discussions

5.2.1 Catalyst screening

NPs of Au, Pd, Rh, or Pt encapsulated in fourth generation polyamidoamine with hydroxyl terminal groups (G4OH) were prepared, purified, and loaded into mesoporous silica MP-SBA-15 (MP denotes medium-sized pores, *vide infra*), following published protocols.[37-41] The typical loading amount was 0.05 mmol of metal per gram of a supported metal catalyst. In a typical reaction test, 0.05 mmol of 4-nitrobenzaldehyde (**1a**), 0.075 mmol of MI, and 10 mg of a catalyst (containing ca. 0.5 μmol of metal, determined by ICP-OES) were mixed with a solvent in a reaction tube with magnetic stirring. For 18-h reaction time at room temperature using toluene as the solvent (Figure

1A), the Au_{40}/G4OH/MP-SBA-15 catalyzed reaction provided the desired oxazoline in >99% yield and 97/3 of *trans*/*cis* ratio, based on ^{1}H NMR. In contrast, the use of the Pd, Rh, and Pt counterparts as catalysts under identical conditions gave low yields and poor product selectivity (Table 1). These observations highlight the critical role of the gold catalysts and rule out G4OH or MP-SBA-15 as the sole catalysts for the reaction. It is also worth noting that **1a** was a challenging substrate for the optimized homogeneous Au(I) catalyst, providing the corresponding oxazoline in only 80% yield with a *trans*/*cis* ratio of 83/17.[25] Three commercially available Au(I) complexes (Figure 1D) were used as catalysts under the same reaction condition; however, these catalysts showed lower activity and selectivity than the optimized Au(I) catalyst. The yield and selectivity of the aldol reaction under similar conditions catalyzed by transition metal ion complex catalysts of Pd, Pt, and Rh are highly dependent on the ligand structures (Table 1).[42-55] However, the Au_{40}/G4OH/MP-SBA-15 catalyst offers the highest activity and selectivity, along with easy recyclability. Intrigued, we proceeded to further investigate the reaction by heterogenized gold catalysts.

Table 1. Comparison of yields and *trans/cis* selectivity for aldol reactions with selected transition metal catalysts.

entry	catalyst	yield (%)	*trans/cis*	ref.
1[a]	Au_{40}/G4OH/MP-SBA-15	99.9	97/3	this work
2[a]	Pd_{40}/G4OH/MP-SBA-15	42.7	81/19	this work
3[a]	Pt_{40}/G4OH/MP-SBA-15	5.1	73/27	this work
4[a]	Rh_{40}/G4OH/MP-SBA-15	1.8	87/13	this work
5[a]	Au(I)-81-9	61.6	68/32	this work
6[a]	Au(I)-82-0	79.1	68/32	this work
7[a]	Au(I)-83-1	57.4	70/30	this work
8	Au(I) complex	80	83/17	25
9[b]	Pd complexes	75-95	56/44-94/6	27
10[b]	Pt complexes	70-96	56/44-94/6	27
11[b]	Rh complexes	95-98	89/11-92/8	27

[a]The reactions were carried out with 0.05 mmol of **1a**, 0.075 mmol of MI, 1 mol% catalyst in toluene at 22 °C for 18 h. Yield and product selectivity were determined by ^{1}H NMR (same below). [b]Bases (*i*-Pr_2NEt or Et_3N) were used. See ref. 12 for detailed reaction conditions.

5.2.2 Kinetics study

The reaction kinetics were probed, and first order kinetics was found on both reactants (Figure 1B). When the reaction mixture was filtered after an hour, the starting materials in the filtrate showed no change over time, suggesting that the reaction was

catalyzed by heterogeneous gold, and that no catalyst leaching into the supernatant had occurred (Figure 1B). In fact, a blank run revealed that in the absence of a catalyst or a base, the aldol reaction did not proceed at room temperature. Furthermore, Au^{3+}/G4OH/MP-SBA-15, which contained Au(III) ions from $HAuCl_4$, was synthesized according to a published procedure.[35] Under the same reaction condition, this Au(III) catalyst gave the product in only 3% yield, demonstrating that Au(III) has very low activity compared to the heterogeneous Au catalysts.

5.2.3 Recycling test

A recycling test using the same batch of a catalyst was carried out. The product solution was separated via centrifugation after each run, and a fresh reactant solution was mixed with the catalyst immediately. The catalyst did not show a decrease in activity after six reaction runs (Figure 1C), providing evidence for the stability and recyclability of the catalyst.

5.2.4 Size effect study

To study the effect of size of the NPs on the catalytic reaction, Au_{20}/G4OH, Au_{40}/G4OH, and Au_{60}/G4OH were synthesized. Though the NPs described in this study are denoted as such, they are not perfectly uniform in size: the subscript refers to the $HAuCl_4$/G4OH molar ratios used in the synthesis, not to the exact number of atoms in each NP. The size distribution of these NPs was obtained from the TEM images (Figure 2). Concurrently, SP-SBA-15 and LP-SBA-15 were prepared to probe the effect of the pore profile of the support.[37-41] SP and LP denote small pore and large pore, respectively. The nitrogen physisorption isotherms (Figure 3) were obtained, and the Barrett-Joyner-Halenda (BJH) model was used to calculate the pore size distribution. The results were summarized in Table 2.

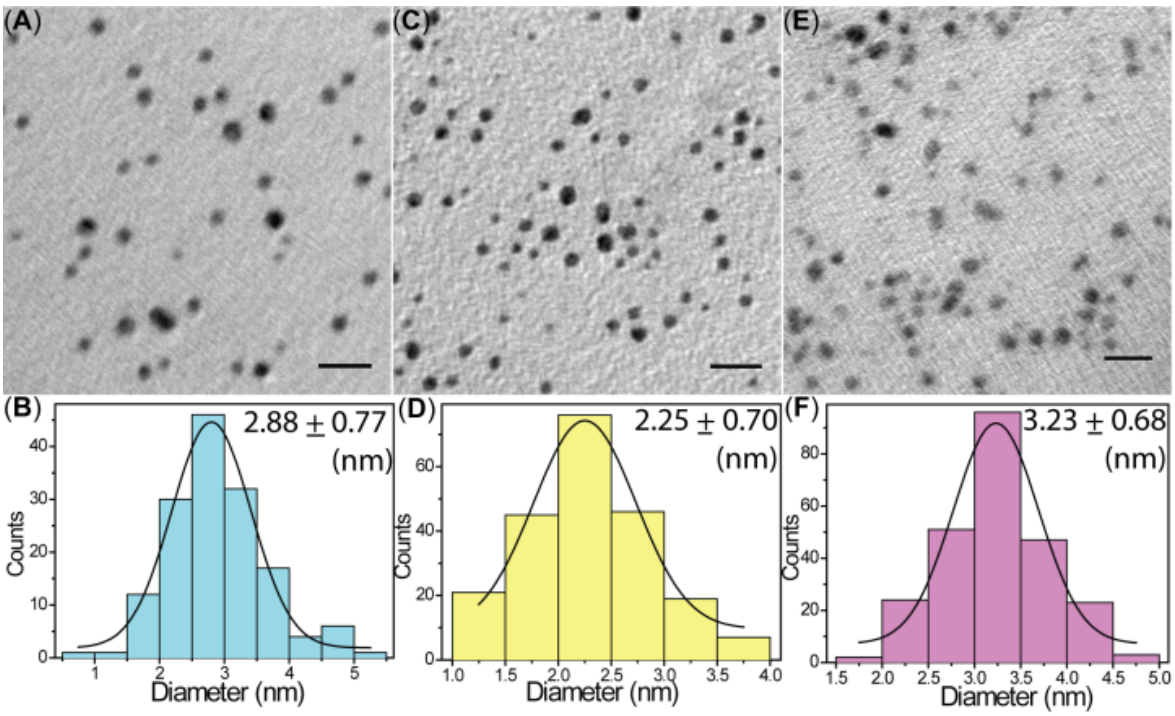

Figure 2. TEM images and corresponding particle size distribution statistics of Au_{40}/G4OH (A), (B); Au_{20}/G4OH (C), (D); Au_{60}/G4OH (E), (F). Scale bars are 10 nm.

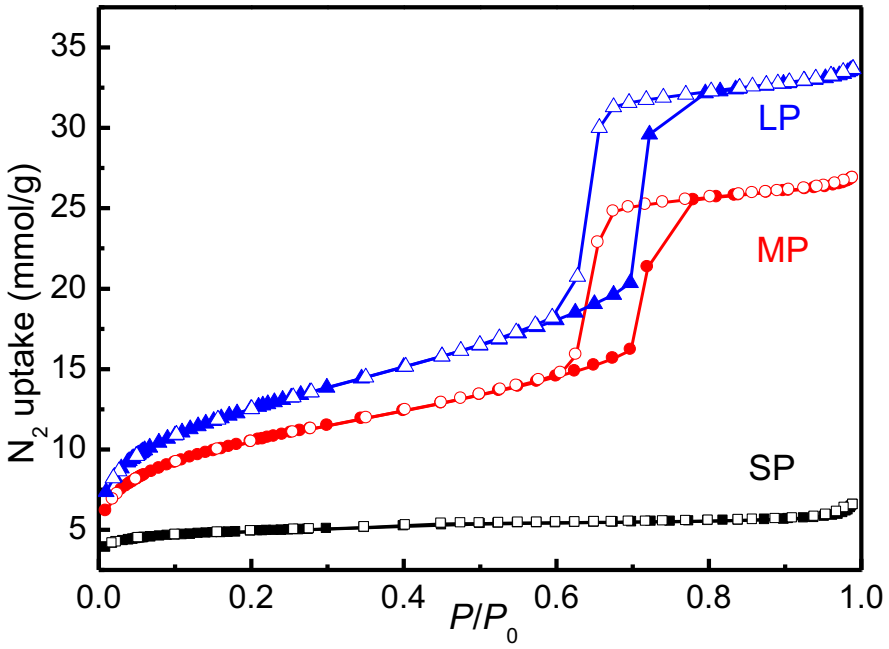

Figure 3. N_2 adsorption-desorption isotherms of solid supports at 77 K with adsorption and desorption points represented by closed and open symbols, respectively.

Table 2. Physisorption characterizations of the solid supports.[a]

material	$S_{BET}/m^2 \cdot g^{-1}$	D_{pore}/nm	$V_{pore}/cm^3 \cdot g^{-1}$
SP-SBA-15	342	4.5	0.22
MP-SBA-15	799	5.8	0.93
LP-SBA-15	966	8.0	1.16

[a]Parameters: S_{BET}: the BET surface area. D_{pore}: average pore diameter calculated from the adsorption branch of the N_2 isotherm by the BJH model. V_{pore}: total pore volume, determined at $p/p_0 = 0.984$.

Au NPs with different sizes were loaded into SBA-15 supports with various pore sizes, respectively. As a result, nine supported catalysts were prepared and used to catalyze the aldol reaction, under the same conditions as shown in Figure 1A, and the *trans*/*cis* selectivity results have been summarized in Table 3. In general, *trans* selectivity was higher in catalysts with larger pores, probably due to the lower free energy of the *trans* product. However, in the confined space of the catalysts with smaller pores, the ratio of the *cis* product was relatively high, likely because of its smaller kinetic diameter. The solvent was another important factor for the *trans*/*cis* ratio of the product. A series of solvents were tested (Table 4). In general, hydrophobic solvents favored the *trans* product strongly, while hydrophilic solvents led to a relatively high ratio of the *cis* product.

Table 3. Ratios of *trans/cis* products from catalysts with various sizes of NPs and pore diameters.[a]

support	Au_{20}/G4OH	Au_{40}/G4OH	Au_{60}/G4OH
SP-SBA-15	80/20	78/22	79/21
MP-SBA-15	93/7	97/3	96/4
LP-SBA-15	100/0	96/4	95/5

[a]All reactions were carried out with 0.05 mmol of **1a**, 0.075 mmol of MI, 1 mol% catalyst in toluene at 22 °C for 24 h. The yield was over 90% in each case.

Table 4. Solvent effects on the aldol reaction.[a]

entry	solvent	yield (%)	*trans/cis*
1	Toluene-d8	99.9	97/3
2	Benzene-d6	99.9	91/9
3	$CDCl_3$	99.9	88/12
4	$CDCl_2CDCl_2$	96.8	83/17
5	DMSO-d6	99.9	79/21

6	Acetone-d6	99.1	65/35
7	CD_3CN	99.9	59/41

[a]All reactions were carried out with 0.05 mmol of **1a**, 0.075 mmol of MI, 1 mol% catalyst in the corresponding solvent at 22 °C for 18 h.

5.2.5 Substituent effect study

A Hammett study was used to probe the rate limiting step of the Au_{40}/G4OH/MP-SBA-15 catalyzed aldol reaction.[28,56] The reaction rates of benzaldehydes with different substitution groups were compared (see Table S1). The rate data were fitted with σ, σ^+, and σ^-, respectively. The σ series fit generally well, except for **8** and **9**, much better than that of σ^+ or σ^- (larger R^2 values, plots not shown here), with the slope ρ = 0.64, as shown in Figure 4B. The deviation of **8** and **9** might be caused by the oxygen's interaction with electrophiles, further lowering the reactivity of these two compounds. The slope was smaller than that obtained for the reaction catalyzed by the homogeneous the Au(I)-complex (ρ = 1.4), indicating that the reaction was less sensitive to the electronic effect on the surface of the Au NP than on the Au(I)-complex. However, the positive slope suggested the increased electron density on the carbonyl carbon atom in the rate-limiting step, which was similar in these two types of catalysts, i.e. they involved electrophilic attack of the aldehyde on the MI (*vide infra*).[28]

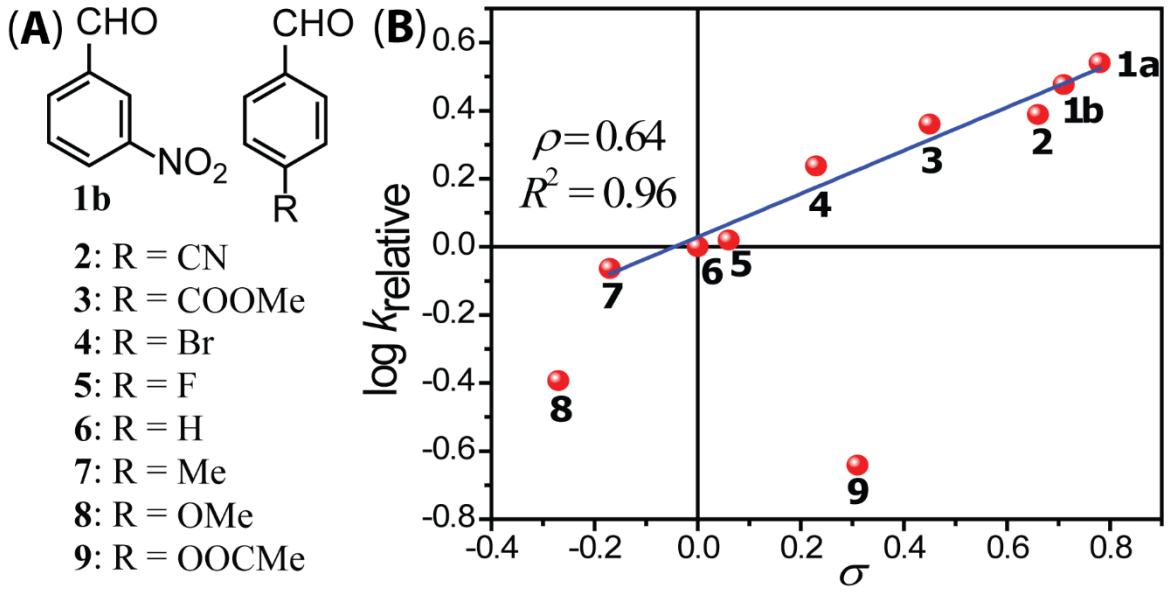

Figure 4. (A) Structures and abbreviations of aldehydes used in this study. (B) A Hammett plot of the reaction of substituted benzaldehydes with MI. The linear fit (blue line) did not include **8** and **9**.

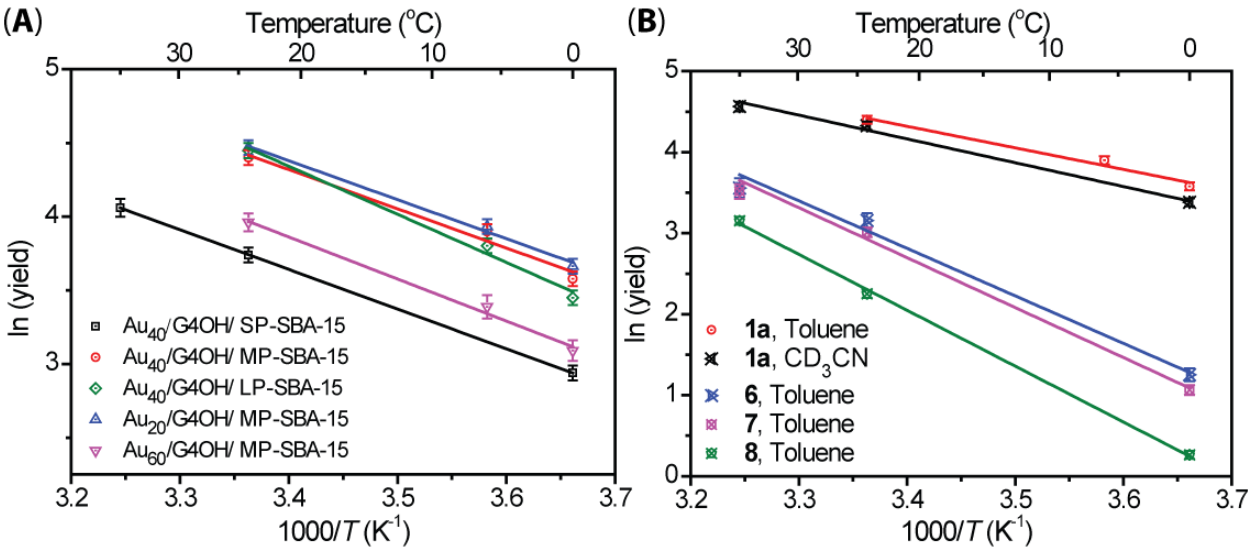

Figure 5. Arrhenius plots of selected cases, focusing on (A) different catalysts, and (B) solvents and reactants. The reaction conditions and the corresponding calculated activation energies are given in Table 5.

5.2.6 Activation energy study

The Arrhenius plots were obtained for selected cases, as shown in Figure 5, and the calculated activation energies were listed in Table 4. For catalysts with different sizes of Au NPs or pore profile of the support, the activation energies were very similar (entries 1-5, Table 5). Changing the solvent from toluene to acetonitrile using the same catalyst gave distinct *trans/cis* product ratio (entries 1 and 7, Table 4), however, overall reaction rates and activation energies were very close (Figure 5B). On the contrary, benzaldehydes with various substituents showed substantial variations in reactivity for the same catalyst. Namely, electron-donating groups increased the activation energy (Table 5).

Table 5. Calculated activation energies of selected cases.[a]

entry	catalyst	reactant	E_a (kJ/mol)
1	Au_{20}/G4OH/MP-SBA-15	**1a**	23.2
2	Au_{40}/G4OH/SP-SBA-15	**1a**	22.4
3	Au_{40}/G4OH/MP-SBA-15	**1a**	23.3
4	Au_{40}/G4OH/LP-SBA-15	**1a**	28.6
5	Au_{60}/G4OH/MP-SBA-15	**1a**	23.9
6	Au_{40}/G4OH/MP-SBA-15	**1a**[b]	24.2
7	Au_{40}/G4OH/MP-SBA-15	**6**	47.5
8	Au_{40}/G4OH/MP-SBA-15	**7**	50.1

9	Au_{40}/G4OH/MP-SBA-15	**8**	57.4

[a]All reactions were carried out with 0.05 mmol of aldehydes, 0.075 mmol of MI, 1 mol% catalyst in toluene (except entry 6) at 0-35 °C for 2 h. [b]Solvent: CD_3CN.

5.2.7 IR study

A series of FT-IR experiments was carried out to elucidate the reaction mechanism. For the pure MI, the stretching vibration frequency of the CN group was 2163 cm^{-1}; for the C=O group it was 1763 cm^{-1}. A fresh solution of Au_{60}/G4OH was concentrated by rotary evaporation to dryness, redispersed in methanol, and used in the IR study, to avoid the strong IR absorption by SBA-15. However, after addition of MI to the Au_{60}/G4OH in methanol, the gold NPs precipitated. The precipitate was transferred onto the IR window for study. The observed CN stretching resonance was split into two bands, the major one at 2223 cm^{-1}, and the minor one at 2159 cm^{-1}. In addition, the C=O stretching peak shifted to 1753 cm^{-1}. These shifts could be explained by the formation of the enolate formed via proton abstraction from the MI, where the blue shift of the CN stretching was caused by the delocalized π-electron conjugation. 2 μL of MI was added to the Au_{60}/G4OH in methanol before a portion of the mixture was used for data collection, and such a procedure was repeated several times. The CN stretching peak at 2163 cm^{-1} grew gradually until it had a larger intensity than the 2223 cm^{-1} peak, because the surface of the Au NPs was gradually saturated with bound MI molecules. To the best of our knowledge, there are few precedents[27] in the literature for this phenomenon, observed by IR spectroscopy of the cyano group stretching vibration. On the contrary, mixing **1a** and Au_{60}/G4OH in methanol did not cause apparent peak shifts of **1a**, as shown in Figure 6C. These observations supported our proposal that the reaction mechanism on the Au surface was likely the same on the Au(I) complex. The tertiary amine groups on the G4OH might serve as the base to accept the proton from MI. The proposed intermediate structure is shown in Figure 6D.

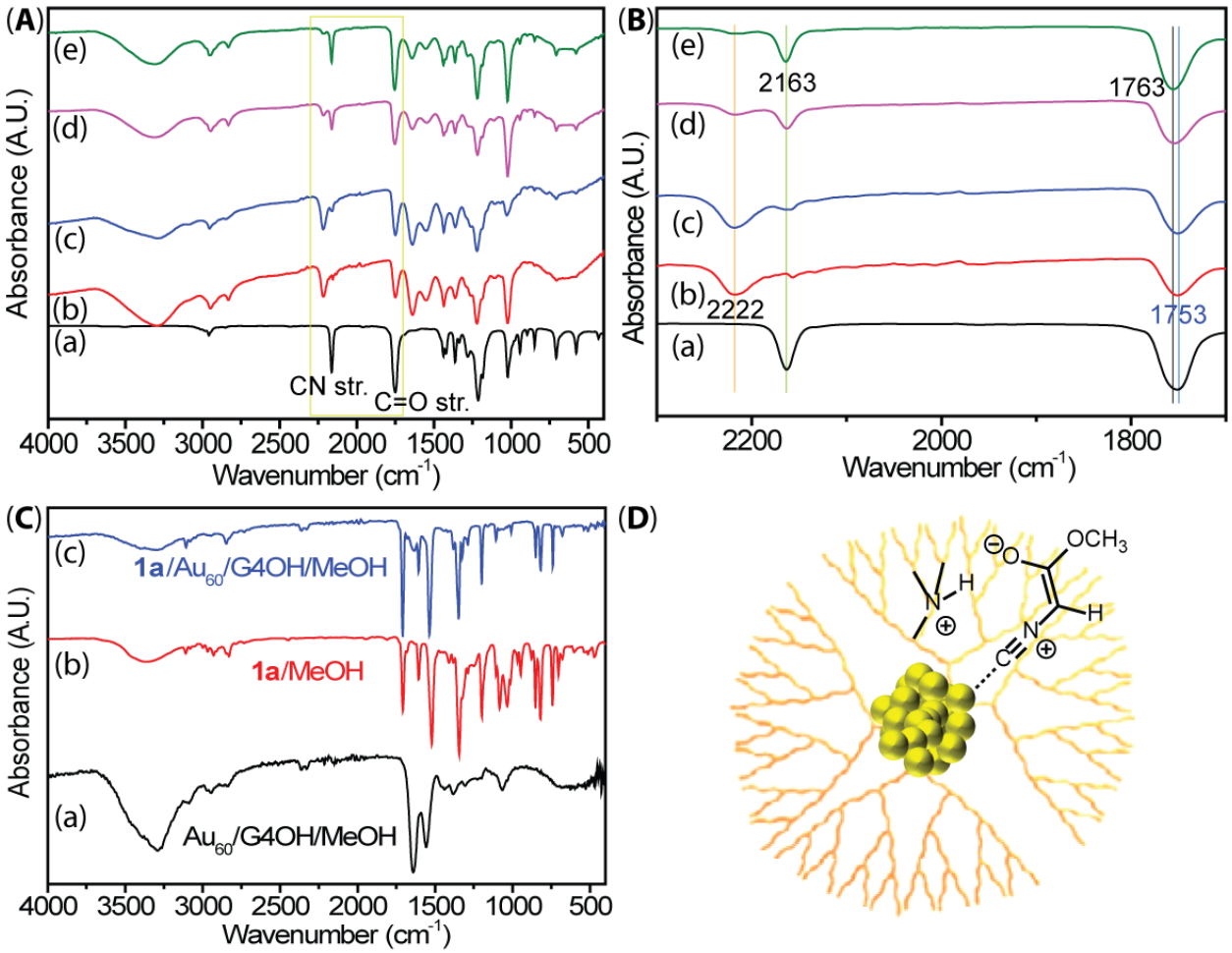

Figure 6. (A) Full FT-IR spectra and (B) zoom-in view of (a) pure MI, and (b)-(e) increasing amount of MI in a Au_{60}/G4OH-methanol suspension. (C) Full FT-IR spectra of (a) G4OH/MeOH, (b) **1a**/MeOH, and (c) **1a**/G4OH/MeOH. (D) The proposed intermediate structure: the deprotonated MI forms an enolate on the gold surface, and the tertiary amines in the dendrimer function as the Brønsted base to accept the proton from MI.

5.3 Conclusions

The current work provides a firm basis for the development of efficient heterogenized homogeneous catalysts with high stereoselectivity in aldol reactions. We established that larger pore sizes of the support and the use of a hydrophobic solvent leads to a high selectivity for the *trans* product in the conversion of aldehydes and MI to 2-oxazolines. The reaction mechanism on the Au surface was found to be analogous to the homogeneous Au(I) catalyzed transformation. The rate-limiting step involves electrophilic attack of the aldehyde on the enolate formed from the deprotonated MI,

which was supported by the Hammett study and IR study. Furthermore, the use of a heterogenized homogenous gold catalyst at room temperature in a hydrophobic solvent did not cause any observable leaching or catalyst deactivation. Thus, the high selectivity of our catalyst in the studied aldol reaction adds to the benefits of simple post-reaction work-up and catalyst recyclability, which will lead to a green version of this chemistry.

5.4 References

1. Wight, A.; Davis, M. Design and preparation of organic-inorganic hybrid catalysts. *Chem. Rev.* **2002**, *102*, 3589-3614.
2. Noël, T.; Buchwald, S. L. Cross-coupling in flow. *Chem. Soc. Rev.* **2011**, *40*, 5010-5029.
3. Astruc, D.; Lu, F.; Aranzaes, J. R. Nanoparticles as recyclable catalysts: The frontier between homogeneous and heterogeneous catalysis. *Angew. Chem. Int. Ed* **2005**, *44*, 7852-7872.
4. Ye, R.; Hurlburt, T. J.; Sabyrov, K.; Alayoglu, S.; Somorjai, G. A. Molecular catalysis science: Perspective on unifying the fields of catalysis. *Proc. Natl. Acad. Sci. U. S. A.* **2016**, *113*, 5159-5166.
5. Iglesia, E.; Reyes, S. C.; Madon, R. J.; Soled, S. L. Selectivity control and catalyst design in the Fischer-Tropsch synthesis: sites, pellets, and reactors. *Adv. Catal.* **1993**, *39*, 221-302.
6. Chen, J. G. Carbide and nitride overlayers on early transition metal surfaces: preparation, characterization, and reactivities. *Chem. Rev.* **1996**, *96*, 1477-1498.
7. Bell, A. T. The impact of nanoscience on heterogeneous catalysis. *Science* **2003**, *299*, 1688-1691.
8. Zhou, K.; Wang, X.; Sun, X.; Peng, Q.; Li, Y. Enhanced catalytic activity of ceria nanorods from well-defined reactive crystal planes. *J. Catal.* **2005**, *229*, 206-212.
9. Lee, I.; Delbecq, F.; Morales, R.; Albiter, M. A.; Zaera, F. Tuning selectivity in catalysis by controlling particle shape. *Nat. Mater.* **2009**, *8*, 132-138.
10. Xia, Y.; Xiong, Y.; Lim, B.; Skrabalak, S. E. Shape‐Controlled Synthesis of Metal Nanocrystals: Simple Chemistry Meets Complex Physics? *Angew. Chem. Int. Ed* **2009**, *48*, 60-103.
11. Xin, H. L.; Alayoglu, S.; Tao, R.; Genc, A.; Wang, C.-M.; Kovarik, L.; Stach, E. A.; Wang, L.-W.; Salmeron, M.; Somorjai, G. A. Revealing the atomic restructuring of Pt–Co nanoparticles. *Nano Lett.* **2014**, *14*, 3203-3207.
12. Niu, Z.; Becknell, N.; Yu, Y.; Kim, D.; Chen, C.; Kornienko, N.; Somorjai, G. A.; Yang, P. Anisotropic phase segregation and migration of Pt in nanocrystals en route to nanoframe catalysts. *Nat. Mater.* **2016**.
13. Davis, M. E. Ordered porous materials for emerging applications. *Nature* **2002**, *417*, 813-821.
14. Tauster, S. J. Strong metal-support interactions. *Acc. Chem. Res.* **1987**, *20*, 389-394.

15. Jones, C. W.; Tsuji, K.; Davis, M. E. Organic-functionalized molecular sieves as shape-selective catalysts. *Nature* **1998**, *393*, 52-54.
16. Gross, E.; Liu, J. H.; Alayoglu, S.; Marcus, M. A.; Fakra, S. C.; Toste, F. D.; Somorjai, G. A. Asymmetric Catalysis at the Mesoscale: Gold Nanoclusters Embedded in Chiral Self-Assembled Monolayer as Heterogeneous Catalyst for Asymmetric Reactions. *J. Am. Chem. Soc.* **2013**, *135*, 3881-3886.
17. Hopkinson, M. N.; Richter, C.; Schedler, M.; Glorius, F. An overview of N-heterocyclic carbenes. *Nature* **2014**, *510*, 485-496.
18. Levartovsky, Y.; Gross, E. Using operando Microspectroscopy to Uncover the Correlations Between the Electronic Properties of Dendrimer-Encapsulated Metallic Nanoparticles and their Catalytic Reactivity in π-Bond Activation Reactions. *Top. Catal.* **2016**, *59*, 1700-1711.
19. Gorin, D. J.; Toste, F. D. Relativistic effects in homogeneous gold catalysis. *Nature* **2007**, *446*, 395-403.
20. Min, B. K.; Friend, C. M. Heterogeneous gold-based catalysis for green chemistry: low-temperature CO oxidation and propene oxidation. *Chem. Rev.* **2007**, *107*, 2709-2724.
21. Melaimi, M.; Soleilhavoup, M.; Bertrand, G. Stable Cyclic Carbenes and Related Species beyond Diaminocarbenes. *Angew. Chem. Int. Ed* **2010**, *49*, 8810-8849.
22. Zhukhovitskiy, A. V.; Mavros, M. G.; Van Voorhis, T.; Johnson, J. A. Addressable Carbene Anchors for Gold Surfaces. *J. Am. Chem. Soc.* **2013**, *135*, 7418-7421.
23. Ye, R.; Zhao, J.; Yuan, B.; Liu, W.-C.; Rodrigues De Araujo, J.; Faucher, F. F.; Chang, M.; Deraedt, C. V.; Toste, F. D.; Somorjai, G. A. New Insights into Aldol Reactions of Methyl Isocyanoacetate Catalyzed by Heterogenized Homogeneous Catalysts. *Nano Lett.* **2017**, *17*, 584-589.
24. Ito, Y.; Sawamura, M.; Hayashi, T. Catalytic asymmetric aldol reaction: reaction of aldehydes with isocyanoacetate catalyzed by a chiral ferrocenylphosphine-gold(I) complex. *J. Am. Chem. Soc.* **1986**, *108*, 6405-6406.
25. Hubbert, C.; Hashmi, A. S. K.: Gold-Catalyzed Aldol and Related Reactions. In *Modern Gold Catalyzed Synthesis*; Wiley-VCH Verlag GmbH & Co. KGaA, 2012; pp 237-261.
26. Trost, B. M.; Brindle, C. S. The direct catalytic asymmetric aldol reaction. *Chem. Soc. Rev.* **2010**, *39*, 1600-1632.
27. Gulevich, A. V.; Zhdanko, A. G.; Orru, R. V. A.; Nenajdenko, V. G. Isocyanoacetate Derivatives: Synthesis, Reactivity, and Application. *Chem. Rev.* **2010**, *110*, 5235-5331.
28. Togni, A.; Pastor, S. D. Chiral cooperativity: the nature of the diastereoselective and enantioselective step in the gold(I)-catalyzed aldol reaction utilizing chiral ferrocenylamine ligands. *J. Org. Chem.* **1990**, *55*, 1649-1664.
29. Mehendale, N. C.; Sietsma, J. R. A.; de Jong, K. P.; van Walree, C. A.; Gebbink, R. J. M. K.; van Koten, G. PCP- and SCS-Pincer Palladium Complexes Immobilized on

Mesoporous Silica: Application in C C Bond Formation Reactions. *Adv. Synth. Catal.* **2007**, *349*, 2619-2630.
30. Van der Boom, M. E.; Milstein, D. Cyclometalated phosphine-based pincer complexes: mechanistic insight in catalysis, coordination, and bond activation. *Chem. Rev.* **2003**, *103*, 1759-1792.
31. Coperet, C.; Chabanas, M.; Saint-Arroman, R. P.; Basset, J. M. Homogeneous and heterogeneous catalysis: Bridging the gap through surface organometallic chemistry. *Angew. Chem. Int. Ed* **2003**, *42*, 156-181.
32. de Almeida, M. P.; Carabineiro, S. A. C. The Best of Two Worlds from the Gold Catalysis Universe: Making Homogeneous Heterogeneous. *Chemcatchem* **2012**, *4*, 18-29.
33. Warner, M. C.; Bäckvall, J.-E. Mechanistic aspects on cyclopentadienylruthenium complexes in catalytic racemization of alcohols. *Acc. Chem. Res.* **2013**, *46*, 2545-2555.
34. Witham, C. A.; Huang, W.; Tsung, C.-K.; Kuhn, J. N.; Somorjai, G. A.; Toste, F. D. Converting homogeneous to heterogeneous in electrophilic catalysis using monodisperse metal nanoparticles. *Nat. Chem.* **2010**, *2*, 36-41.
35. Gross, E.; Liu, J. H.-C.; Toste, F. D.; Somorjai, G. A. Control of selectivity in heterogeneous catalysis by tuning nanoparticle properties and reactor residence time. *Nat. Chem.* **2012**, *4*, 947-952.
36. Ye, R.; Yuan, B.; Zhao, J.; Ralston, W. T.; Wu, C.-Y.; Unel Barin, E.; Toste, F. D.; Somorjai, G. A. Metal Nanoparticles Catalyzed Selective Carbon–Carbon Bond Activation in the Liquid Phase. *J. Am. Chem. Soc.* **2016**, *138*, 8533-8537.
37. Zhao, D.; Feng, J.; Huo, Q.; Melosh, N.; Fredrickson, G. H.; Chmelka, B. F.; Stucky, G. D. Triblock Copolymer Syntheses of Mesoporous Silica with Periodic 50 to 300 Angstrom Pores. *Science* **1998**, *279*, 548-552.
38. Crooks, R. M.; Zhao, M. Dendrimer-Encapsulated Pt Nanoparticles: Synthesis, Characterization, and Applications to Catalysis. *Adv. Mater.* **1999**, *11*, 217-220.
39. Crooks, R. M.; Zhao, M.; Sun, L.; Chechik, V.; Yeung, L. K. Dendrimer-Encapsulated Metal Nanoparticles: Synthesis, Characterization, and Applications to Catalysis. *Acc. Chem. Res.* **2001**, *34*, 181-190.
40. Kim, Y. G.; Oh, S. K.; Crooks, R. M. Preparation and characterization of 1-2 nm dendrimer-encapsulated gold nanoparticles having very narrow size distributions. *Chem. Mater.* **2004**, *16*, 167-172.
41. Huang, W.; Kuhn, J. N.; Tsung, C.-K.; Zhang, Y.; Habas, S. E.; Yang, P.; Somorjai, G. A. Dendrimer Templated Synthesis of One Nanometer Rh and Pt Particles Supported on Mesoporous Silica: Catalytic Activity for Ethylene and Pyrrole Hydrogenation. *Nano Lett.* **2008**, *8*, 2027-2034.
42. Linic, S.; Aslam, U.; Boerigter, C.; Morabito, M. Photochemical transformations on plasmonic metal nanoparticles. *Nat. Mater.* **2015**, *14*, 567-576.

43. Brus, L. Plasmon-driven chemical synthesis: Growing gold nanoprisms with light. *Nat. Mater.* **2016**, *15*, 824-825.
44. Moskovits, M. The case for plasmon-derived hot carrier devices. *Nat Nano* **2015**, *10*, 6-8.
45. Zhu, H.; Chen, X.; Zheng, Z.; Ke, X.; Jaatinen, E.; Zhao, J.; Guo, C.; Xie, T.; Wang, D. Mechanism of supported gold nanoparticles as photocatalysts under ultraviolet and visible light irradiation. *Chem. Commun.* **2009**, 7524-7526.
46. Liu, L.; Li, P.; Adisak, B.; Ouyang, S.; Umezawa, N.; Ye, J.; Kodiyath, R.; Tanabe, T.; Ramesh, G. V.; Ueda, S.; Abe, H. Gold photosensitized SrTiO3 for visible-light water oxidation induced by Au interband transitions. *Journal of Materials Chemistry A* **2014**, *2*, 9875-9882.
47. Hou, W.; Hung, W. H.; Pavaskar, P.; Goeppert, A.; Aykol, M.; Cronin, S. B. Photocatalytic Conversion of CO2 to Hydrocarbon Fuels via Plasmon-Enhanced Absorption and Metallic Interband Transitions. *ACS Catal.* **2011**, *1*, 929-936.
48. Bernardi, M.; Mustafa, J.; Neaton, J. B.; Louie, S. G. Theory and computation of hot carriers generated by surface plasmon polaritons in noble metals. *Nat. Commun.* **2015**, *6*, 7044.
49. Zou, R.; Guo, X.; Yang, J.; Li, D.; Peng, F.; Zhang, L.; Wang, H.; Yu, H. Selective etching of gold nanorods by ferric chloride at room temperature. *CrystEngComm* **2009**, *11*, 2797-2803.
50. Keblinski, P.; Cahill, D. G.; Bodapati, A.; Sullivan, C. R.; Taton, T. A. Limits of localized heating by electromagnetically excited nanoparticles. *J. Appl. Phys.* **2006**, *100*, 054305.
51. Nguyen, S. C.; Zhang, Q.; Manthiram, K.; Ye, X.; Lomont, J. P.; Harris, C. B.; Weller, H.; Alivisatos, A. P. Study of Heat Transfer Dynamics from Gold Nanorods to the Environment via Time-Resolved Infrared Spectroscopy. *ACS Nano* **2016**, *10*, 2144-2151.
52. Khurgin, J. B. How to deal with the loss in plasmonics and metamaterials. *Nat Nano* **2015**, *10*, 2-6.
53. Wang, J.; Ando, R. A.; Camargo, P. H. C. Controlling the Selectivity of the Surface Plasmon Resonance Mediated Oxidation of p-Aminothiophenol on Au Nanoparticles by Charge Transfer from UV-excited TiO2. *Angew. Chem. Int. Ed* **2015**, *54*, 6909-6912.
54. Wang, C.; Astruc, D. Nanogold plasmonic photocatalysis for organic synthesis and clean energy conversion. *Chem. Soc. Rev.* **2014**, *43*, 7188-7216.
55. Wang, F.; Li, C.; Chen, H.; Jiang, R.; Sun, L.-D.; Li, Q.; Wang, J.; Yu, J. C.; Yan, C.-H. Plasmonic Harvesting of Light Energy for Suzuki Coupling Reactions. *J. Am. Chem. Soc.* **2013**, *135*, 5588-5601.
56. Hansch, C.; Leo, A.; Taft, R. W. A survey of Hammett substituent constants and resonance and field parameters. *Chem. Rev.* **1991**, *91*, 165-195.

Chapter 6 - Platinum and Other Transition Metal Nanoclusters (Pd, Rh) Stabilized by PAMAM Dendrimer as Excellent Heterogeneous Catalysts: Application to the Methylcyclopentane (MCP) Hydrogenative Isomerization

(This chapter covers similar material as in Deraedt, C.; Melaet, G.; Ralston, W. T.; Ye, R.; Somorjai, G. A. *Nano. Lett.* **2017**, *17*, 1853-1862. – reproduced with permission, copyright 2017 American Chemical Society.)

Abstract

Pt, Rh, and Pd nanoclusters stabilized by PAMAM dendrimer are used for the first time in a gas flow reactor at high temperature (150–250 °C). Pt nanoclusters show a very high activity for the hydrogenation of the methylcyclopentane (MCP) at 200–225 °C with turnover freqency (TOF) up to 334 h^{-1} and selectivity up to 99.6% for the ring opening isomerization at very high conversion (94%). Rh nanoclusters show different selectivity for the reaction, that is, ring opening isomerization at 175 °C and cracking at higher temperature whereas Pd nanoclusters perform ring enlargement plus dehydrogenation, while maintaining a high activity. The difference in these results as compared to unsupported/uncapped nanoparticles, demonstrates the crucial role of dendrimer. The tunability of the selectivity of the reaction as well as the very high activity of the metal nanoclusters stabilized by dendrimer under heterogeneous conditions open a new application for dendrimer catalysts.

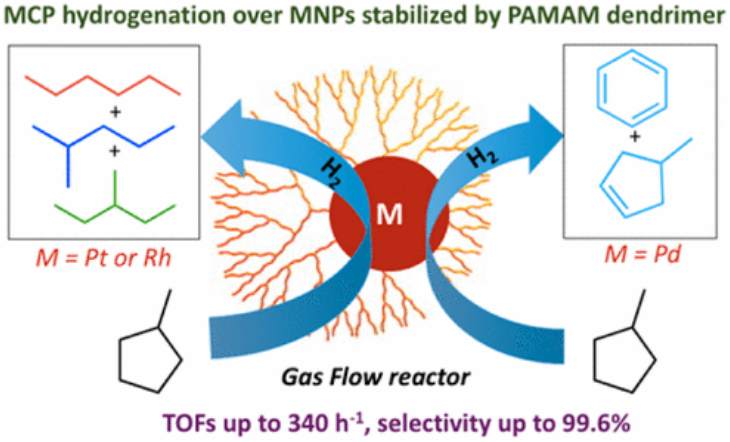

6.1 Introduction

Since the syntheses of the first dendrimers in the 1980s by Vogtle,[1,2] Denkewalter,[3] Tomalia,[4] Newkome,[5] and Frechet,[6] the treelike polymers have been used in various scientific fields such as drug delivery, gene delivery, sensors, support of catalyst, or as stabilizing agent for metallic nanoparticle/cluster (MNP), due to their well-controlled three-dimension cauliflower shape. Crooks has developed syntheses of very small well-defined metallic clusters stabilized by polyamidoamine dendrimers, that is, PAMAM (from generations 2 G2 to generation 6 G6).[7,8] As an example, the PAMAM dendrimer of generation 4 with 64 hydroxyl termini (PAMAM-G4OH) is able to stabilize MNPs of controlled size between 0.8 nm (20 atoms) to 1.2 nm (60 atoms) where M = Pd, Pt, Au or Rh. These MNPs have been employed in catalysis because of their high surface to volume ratio but predominantly in homogeneous applications. Nanoparticle stabilized by dendrimers have been used in homogeneously catalyzed reactions such as C—C cross coupling (Suzuki, Heck, Sonogashira, Stille),[9-11] hydrogenation of double bonds,[8,12] selective hydrogenation of triple bonds,[13,14] nitrophenol/methyl blue/methyl orange hydrogenation,[15-17] and alcohol oxidations.[18] Most of these reactions are carried out in liquid phase and can be catalyzed by both homogeneous or heterogeneous catalysts.

Eight years ago our research group studied ways to heterogenize homogeneous nanoparticles stabilized by PAMAM on a silica mesoporous support (SBA-15).[19] These heterogeneous catalysts were employed in homogeneous type reactions such as alkene hydrogenation or cyclization reactions via π-bond activation in liquid flask batch reactor and also in a liquid flow reactor.[19-21] Zaera et al. have used PtNPs stabilized by PAMAM impregnated/supported on SiO_2 for isomerization of trans-2-butene.[22] In the same way, Astruc et al. impregnated their preformed PdNPs stabilized by their homemade dendrimers on a magnetic support, enhancing the recyclability and the robustness of their catalyst as well as activity.[18] Recently, we have demonstrated that heterogeneous RhNPs stabilized by PAMAM supported on SBA-15 was able to break a C—C sp3 bond of a strained three-membered ring in the presence of 1 atm hydrogen gas in liquid phase.[23] In this paper, we demonstrate the utility and the very high activity of nanoparticle catalysts stabilized by dendrimer in a gas-phase flow mode heterogeneous reaction at high temperature. To the best of our knowledge, this use of dendrimer stabilized catalyst in such heterogeneous conditions (reagents in gas flow reactor, under hydrogen, at high temperature) has not been reported in the literature.

As a model heterogeneous reaction, we decided to study the hydrogenative isomerization of methylcyclopentane (MCP) in gas phase under continuous flow processes at different temperatures from 125 to 275 °C. This reaction is an interesting example of a multipathway heterogeneous reaction leading to various final products (Scheme 1).[24-37] The hydrogenolysis of MCP gives rise to three isomers (ring opening, pathway A), the n-hexane, the 2-methylcyplentane (2-MP), and the

3-methylcyclopentane (3-MP).[24-26] C1 – C5 hydrocarbons can be formed by cracking reactions (pathway B), and dehydrogenation leads to the methylcyclopentene (pathway D). Finally, cyclohexane and benzene (pathway C) are obtained from ring enlargement and ring enlargement/dehydrogenation. The selective ring-opening of naphthenic molecules to alkanes is a potential solution for significantly improving cetane number (CN) of light-cycle oils or the octane number of gasoline after hydrogenation of aromatics. In this reaction, the preferential pathway, A, corresponds to the selective hydrogenolysis of one endocyclic C—C bond. In this work, the hydrogenative isomerization of the MCP was investigated in the presence of PtNPs, PdNPs, RhNPs, AuNPs, and CuNPs all stabilized by PAMAM-G4OH and supported on SBA-15. While Au and Cu catalysts present no activity for the reaction, Pt, Rh, and Pd catalysts show three different but complementary selectivity up to 99.6% for ring opening isomerization in the case of Pt with high turnover frequency (TOF) up to 334 h^{-1} at 225 °C. The PAMAM-G4OH stabilized Pt catalyst offers high selectivity with the highest activity for MCP hydrogenenolysis of any previously reported catalyst in this low-temperature range (200–225 °C). We believe that this exceptional behavior can be attributed to the local environment provided by the dendrimer. The investigation in the Pt cluster size from 1.2 to 1.6 or 1.9 nm shows a sleazy increase in the activity.

Scheme 1. Methyl Cyclopentane Multipath Reaction

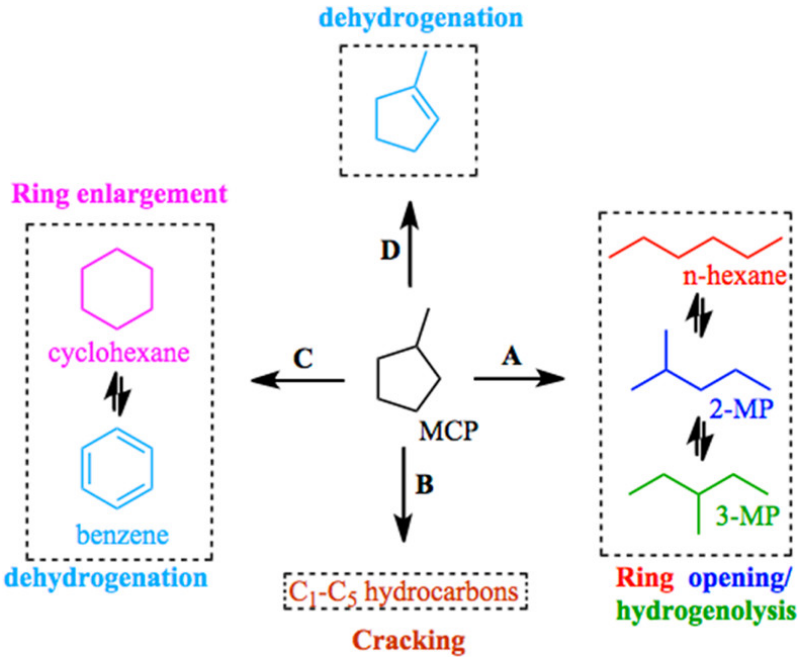

6.2 Experimental and discussion

6.2.1 Syntheses of the catalysts

The catalysts studied in the hydrogenative isomerization of MCP were synthesized in two steps. The first step consists in synthesizing the homogeneous MNPs (M = Pt, Pd, Rh, Au, and Cu) stabilized by the fourth generation G4OH PAMAM dendrimer in water solution by following Crooks' method.[8,19] This step is also composed of two steps, the complexation of the metallic ions to the tertiary amines of the dendrimer and the reduction of these metallic ions to the NPs (see Scheme 2). Briefly, the PtNPs were synthesized using a flask containing 1.25 μmol of PAMAM G4OH dissolved in 5 mL of deionized water. Subsequently, a 0.05 mmol of H_2PtCl_4 dissolved in 5 mL of deionized water was added to the dendrimer solution in order to achieve a ratio 40/1 of Pt atoms for one dendrimer. The solution was degassed with argon during 30–45 min and then allowed to stir slowly for 3 days at room temperature. This time length is necessary to ensure the complete complexation of Pt(II) by the tertiary amine of the dendrimer. A partial complexation of Pt(II) would lead to a polydispersed size of nanoparticle after the reduction step. After 3 days of complexation, fresh sodium borohydride $NaBH_4$ (10 equiv per Pt) dissolved in 2 mL of 5 °C deionized water was added dropwise to the Pt(II)/PAMAM-G4OH solution with a fast stirring. This leads to an instantaneous change of color from yellow/brown to dark black. The solution was allowed to stir 6 more hours before proceeding to the purification/washing step, that is, dialysis. The size and the distribution of the PtNPs were checked by TEM. The average sizes measured from the TEM image were 1.6 ± 0.2 nm for Pt40G4OH (Figure 1), 1.2 nm ± 0.3 nm for Pt20G4OH, and 1.9 ± 0.2 nm for Pt50G4OH. The synthesis slightly differs when the metal is changed. At this stage, the catalyst is ready for homogeneous catalysis.

Scheme 2. Synthesis of Heterogeneous Nanoparticles Stabilized by G4OH PAMAM Dendrimer and Supported on SBA-15[19]

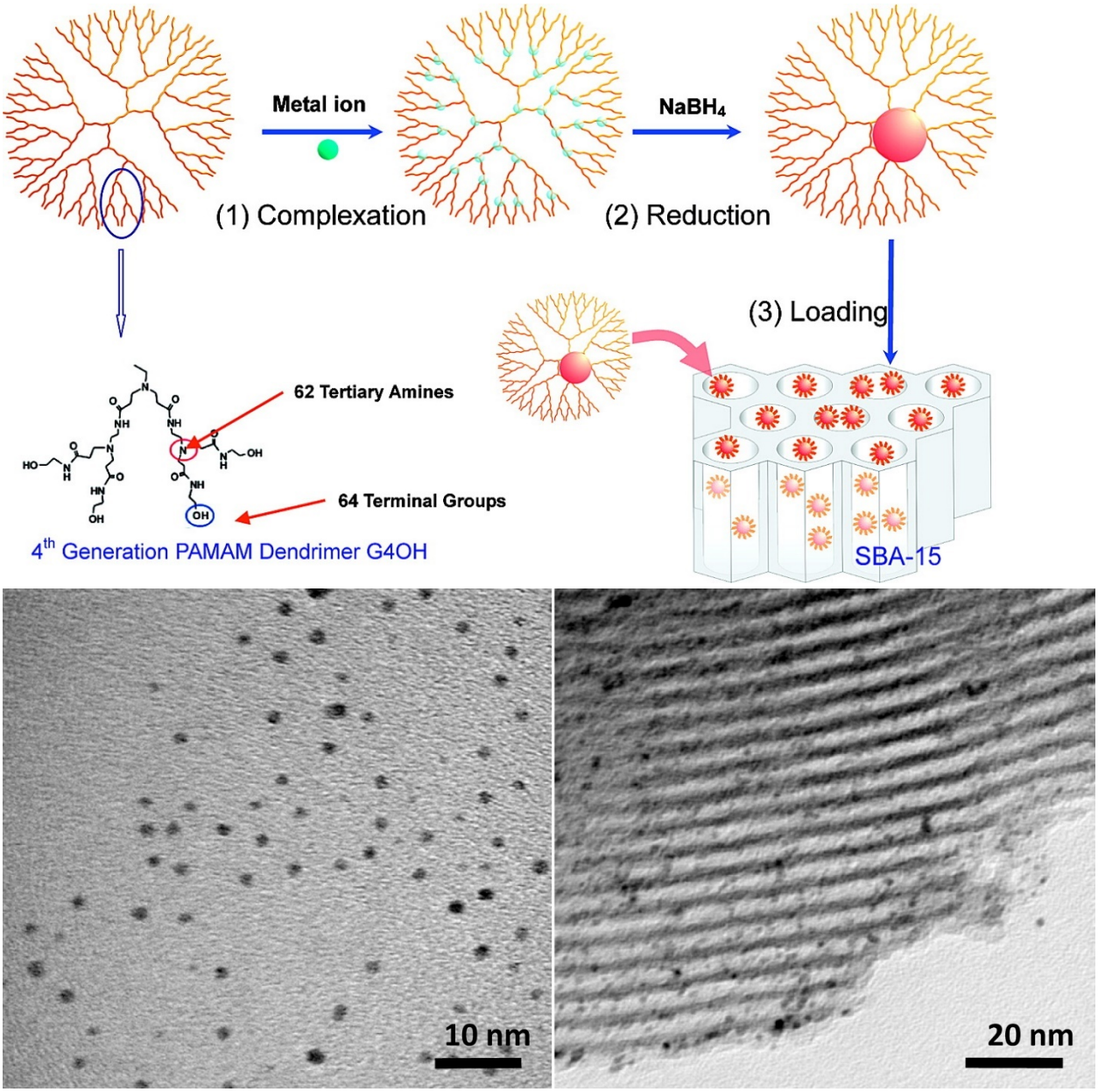

Figure 1. TEM images of platinum nanoparticle stabilized by G4OH dendrimer unsupported (left) and supported (1.5 wt %) on SBA-15 (right).

The final supported catalyst (second step) is obtained by mixing a mesoporous SBA-15 support with the nanoparticle water solution in an ultrasonic bath for 3 h at room temperature in order to achieve 1.5 wt % Pt loading for example. The catalyst was centrifugated and then dried in an oven at 80 °C for 2–3 days. The success of the impregnation was proved by inductively coupled plasma–optical emission spectroscopy (ICP-OES) and transmission electron microscopy (TEM). ICP-OES revealed that the loading was 100% successful. TEM images, revealed that the size of the MNPs remain

unchanged after the loading. Using this technique, we were able to produce MNPs-supported with 0.0077 mol % of Pt, Rh, Pd, Cu, and Au. Moreover, the Pt catalysts were characterized by X-ray absorption fine structure EXAFS and by ethylene hydrogenation test. Ethylene hydrogenation was used to determine the number of active sites of all our Pt NP catalysts.[38] The samples were tested before and after their use in the MCP reaction. Ethylene hydrogenation on Pt is a structure insensitive reaction with a well-known TOF at 25 °C, that is, 10.7 h^{-1}.

6.2.2 PtNPs as catalysts in the hydrogenative isomerization of MCP

PtNPs, RhNPs, PdNPs, AuNPs, and CuNPs were used in the hydrogenative isomerization of MCP and show interestingly different behaviors. The first catalyst tested was the Pt catalyst; it is well-known that PtNPs are generally good catalysts for the hydrogenative isomerization of the MCP, following the pathway A (Scheme 1). PtNPs-G4OH/SBA-15 catalyst (1.5 wt %) named Pt/SBA-15 here after, was tested at different temperatures from 125 to 275 °C (step = 25 °C). The catalytic testing was performed using a home-built plug-flow reactor. The reactant (MCP) flow was introduced in the system with a syringe pump at a flow rate of 0.005 mL·min^{-1} (0.020 mL·min^{-1} in the gas phase). A total gas flow of 40.02 mL·min^{-1} was used (10 mL·min^{-1} of He and 30 mL·$min^{-1}$of H_2). The catalyst (200 mg) was pretreated 1 h at 150 °C under the 40 mL·min^{-1} gas flow without MCP.

The reaction started at 150 °C and 7% of the starting MCP was consumed. As expected, the main products synthesized were the isomers 2-MP and 3-MP. Interestingly, 99.6% of ring opening isomers and only 0.4% of cracking were observed at this temperature, which is one of the highest ring opening isomer selectivity observed for this reaction (see Tables 1 and 2). By increasing the temperature, the conversion of MCP increases to 94% at 225 and 250 °C, leading to TOFs up to 229 h^{-1} (at such high conversion the TOF number might be underestimated as the activity of the catalyst is most likely limited by mass transfer). This is the first report of Pt catalyst with high conversion and high TOF at such low temperature, demonstrating the exceptional behavior of PtNPs stabilized by dendrimers supported on SBA-15. No MCP conversion was observed in the presence of SBA-15 alone at those temperatures, highlighting the role of the Pt here.

Table 1. MCP conversion over Pt/SBA-15, and temperature dependence of TOF[a]

Temperature (°C)	TOF (h^{-1})	Conversion (%)
125	0.0	0
150	22.9	7
175	48.7	20
200	189	77.4
225	229	94

250	228	93.5
275	194	79.6

[a]TOF was calculated as molecules consumed per hour per platinum atom at the surface of the nanoparticle (Pt active sites). The Pt atoms at the surface correspond to 71.25% of the total number of Pt by a simple hard sphere counting model of a 1.6 nm nanoparticle.

Table 2. Selectivity between pathway A (RO/I), B (cracking), C (E/DH), and D (DH) with Pt/SBA-15

Temperature (°C)	Cracking (%)	RO/I (%)	DH (%)	E + DH (%)
125	0.001	0	0	0
150	0.4	99.6	0	0
175	0.6	99.4	0	0
200	0.3	99.6	0	0.1
225	2.2	96.9	0	0.9
250	9.5	86.1	0	4.4
275	16	74.7	0.009	9.3

At 225 °C, the ring opening isomer selectivity is 96.9%, benzene (pathway C) is obtained at 0.87%, and 2.2% of cracking products are detected. This is also the highest degree of isomer selectivity reported at high conversion.

The activity of the catalyst at 250 °C decreases slightly in time. At 275 °C we observed a more drastic deactivation. The MCP conversion felt off to 79.6% and the selectivity over cracking increases up to 16% (traces of methylcyclopentene were observed). The reason for this deactivation was investigated and discussed later.

The formation of the ring enlargement/dehydrogenation product, that is, benzene, is observed at 200 °C in a very small concentration, 0.1%, and increases with temperature increase. We have not detected the production of cyclohexane on Pt/SBA-15. A complete description of the product selectivity for each temperature is given in Table 2.

The selectivity over the ring opening isomerization (Figure 2) leads mainly to 2-MP. This can be explained by the fact that the C—C in β-position of the branched CH_3 of MCP is easier to break and also two breaking positions lead to this product (see Scheme 3).[39,40] The second main isomer is the 3-MP, obtained from a C—C breaking bond in γ-position of the branched CH_3, which requires a similar energy as for the C—C in beta position, but only one position leads to this product. Hexane is only obtained at 175 °C and in lower proportion because C—C bond in α-position is more difficult to break.[41] By increasing the temperature, the hexane formation selectivity increases at the expense of the 2-MP.

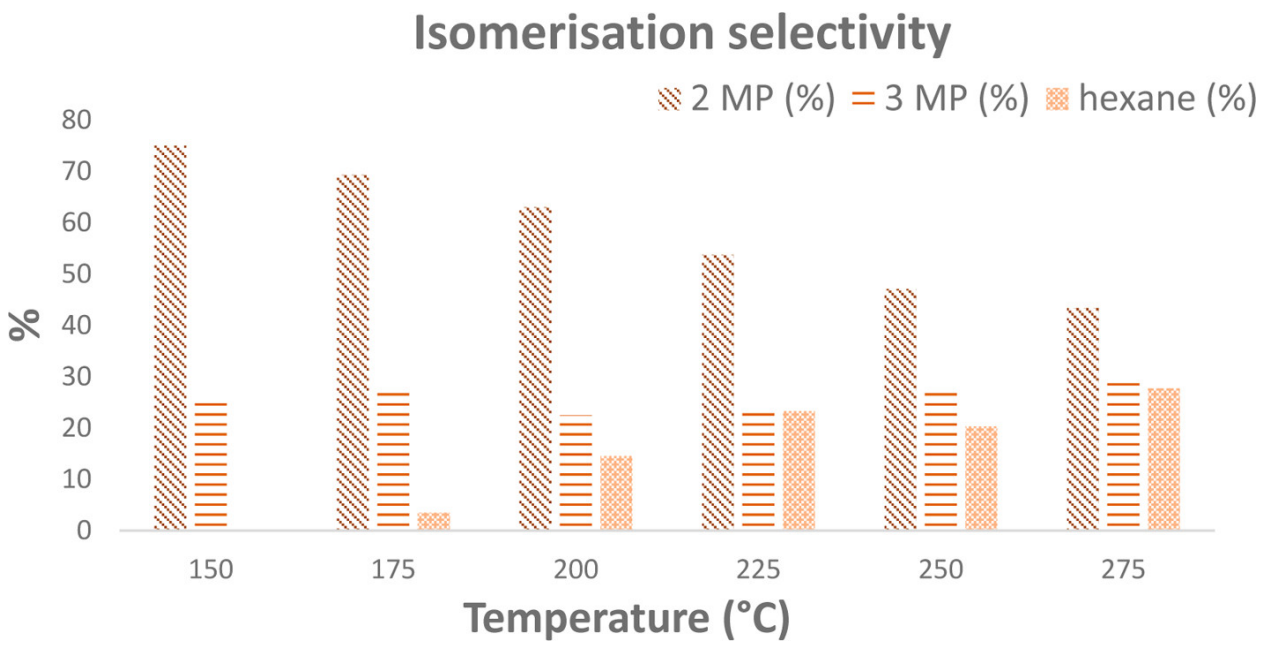

Figure 2. Isomerization selectivity with Pt/SBA-15 at different temperatures.

Scheme 3. Three different products formed during the hydrogenative isomerisation of MCP

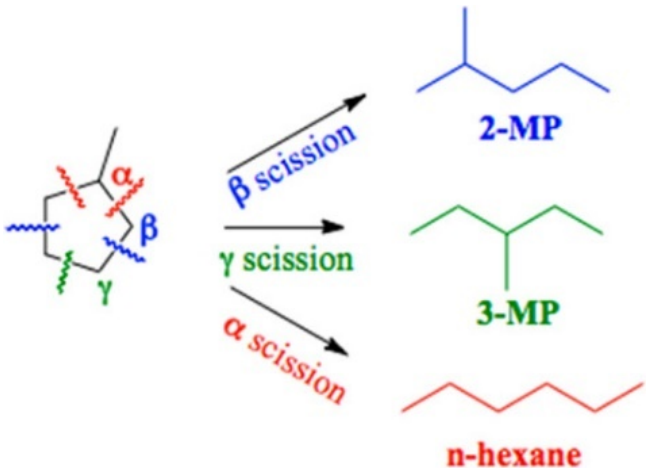

It has been reported that the selectivity to ring isomers is dependent on the size of PtNPs. In the case of uncapped PtNPs, larger size usually leads to 2:1 to 3:1 selectivity in 2-MP to 3-MP, whereas small NPs lead to a random selectivity in those isomers. In the present work, we report a 3:1 isomer ratio on small NPs demonstrating the influence of the dendrimer on the reaction pathway.

As stated, we observe that Pt/SBA-15 loses its activity after reacting at 275 °C. The TEM images of Pt/SBA-15 post-mortem show the sintering of the nanoparticles. We

believe that 275 °C leads to the destruction of the dendrimer that frees the NPs allowing them to diffuse and sinter. We also observed a slow deactivation in time for our Pt/SBA-15 when kept at 250 °C for long time. We were able to link this slow deactivation to the formation of coke (carbonaceous deposit) covering the surface of the catalyst. ICP-OES revealed that no Pt leaching occurs during the reaction, as the percentage of Pt before and after the reaction remains unchanged. Additionally, TEM shows that the size of PtNPs remained unchanged after reaction at 250 °C, evidencing no sintering. To further confirm the loss of active sites, we performed ethylene hydrogenation of the used catalyst, which reveals that the number of active sites decreases by almost a factor of 2 (only 56% of the active sites remained) after 4 h of reaction at 250 °C.

6.2.3 Size dependence of PtNPs on the hydrogenation of MCP

As explained in the introduction, the interest of using the PAMAM dendrimer as a stabilizing agent is its template role allowing the formation of well-controlled small nanoparticles. By using different ratio of Pt/PAMAM, the theoretical size can be tuned from 0.8 nm (ratio 20/1) to 1.6 nm (ratio 50/1). In our case, we synthesized Pt20NPs stabilized by G4OH (ratio 20/1 Pt/dendrimer used during the synthesis) with an average size of 1.2 ± 0.3 nm and then supported on SBA-15, Pt20/SBA-15, and also Pt50NPs stabilized by G4OH with an average size of 1.9 ± 0.2 nm also supported on SBA-15, Pt50/SBA-15. We synthesized again Pt40NPs supported on SBA-15 with a different loading, Pt40/SBA-15 (different name for distinguishing it from Pt/SBA-15 previously introduced) in order to reach the same loading in all Pt catalysts (that is, 1.2 wt %). We conducted extended X-ray absorption fine structure (EXAFS) analyses of Pt L3 edge to obtain information on the structure of our Pt catalysts in air, during a pretreatment with H_2, and under reaction conditions. Fourier transformations of k3-weighted EXAFS for three catalysts under air are shown in Figure 3. In the R space data of the EXAFS, we observe a prominent peak at 1.7 Å from the Pt—O as well as a bigger peak at 2.6 Å, which we determine to be the Pt—Pt. This indicates that our catalysts are partially oxidized before the hydrogen pretreatment. The peak around 2.1 Å can be attributed to Pt—X (with X = O or N) with O coming either from the silica support or from the dendrimer or N coming from the amine and amides groups of the dendrimer.[41] The intensity of the Pt—O at 1.7 Å for Pt20/SBA-15 is higher than Pt40/SBA-15 and Pt50/SBA-15. From these data, we conclude that the smaller the particle, the more oxidized it is. Once exposed to hydrogen pretreatment at 150 °C, the peak at 1.7 Å, that is, Pt—O contribution, disappeared (reduction by a factor of 4–6) for the three samples, showing evidence of the Pt reduction. In fact, after reduction the EXAFS spectra of the three catalysts are similar to the spectrum of Pt foil[8] with a main component at 2.6 Å (Pt—Pt) and a smaller one at 2.1 Å coming from the support/stabilizer, as said previously (see Figure 4 for Pt50/SBA-15). Interestingly even the smaller nanoparticles seem completely reduced under hydrogen pretreatment.

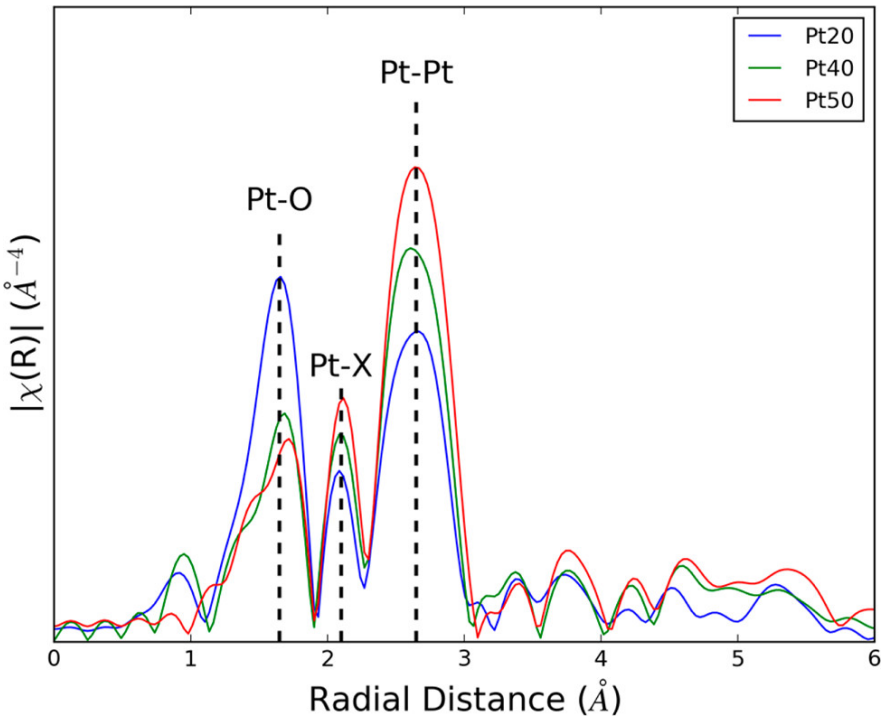

Figure 3. EXAFS of Pt20/SBA-15, Pt40/SBA-15, and Pt50/SBA-15 under air at room temperature.

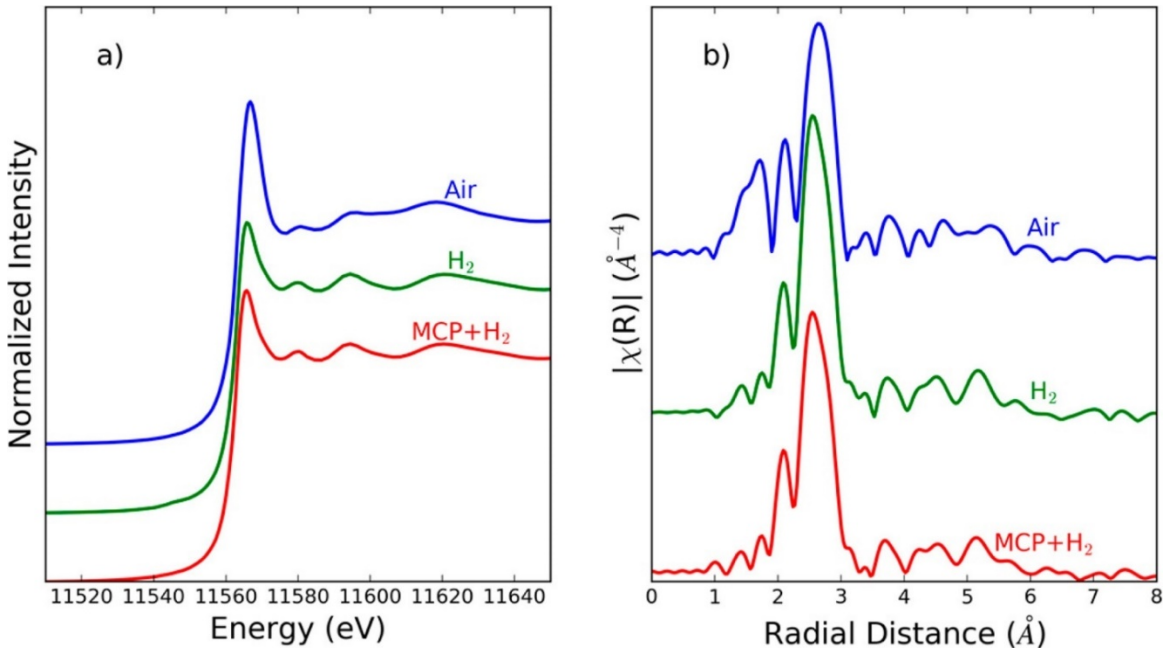

Figure 4. (a) Near edge X-ray absorption fine structure of Pt50/SBA-15 under air, H_2 at 150 °C, and MCP conditions at 175 °C. (b) Fourrier transform of EXAFS of Pt50/SBA-15 under air, H_2, and MCP conditions in the R-space.

In situ measurements of the EXAFS under reaction conditions highlight the fact that all the catalyst remain reduced.

The summary of the catalytic screening for each catalyst are presented in Table 3. No difference in selectivity was observed between the three catalysts as they all produce isomers above 98%. In terms of activity, we observe a slight increase in the TOFs as the size of the nanoparticle increases, reaching a TOF of 334 h^{-1} for Pt50/SBA-15. This is typical of the MCP hydrogenation as observed in previous work[29] but no other significant differences between sizes are observed.

Table 3. Catalytic activities of Pt20/SBA-15, Pt40/SBA-15, and Pt50/SBA-15[a]

Catalyst (temp. °C)	MCP conversion (product formation)	TOF (h^{-1})	Cracking (%)	RO/I (%)	DH (%)	E + DH (%)
Pt20/SBA-15 (200)	32.2% (30.5%)	83.5	1.6	98.3	0	0.1
Pt20/SBA-15 (225)	83.5% (73%)	217	0.9	98.6	0	0.5
Pt50/SBA-15 (200)	44.2% (40.2%)	151	0.2	99.6	0	0.2
Pt50/SBA-15 (225)	98% (86.4%)	334	1.3	98.3	0	0.4
Pt40/SBA-15 (200)	57.2% (54.3%)	174	0.2	99.7	0	0.1
Pt40/SBA-15 (225)	93% (83%)	283	1.4	98.2	0	0.4

[a]TOF was calculated as molecules consumed per hour per platinum atom at the surface of the nanoparticle. The Pt atoms at the surface correspond to 83.66%, 71.25%, and 63.65% of the total number of Pt (simple hard sphere counting model of a 1.2, 1.6 and 1.9 nm nanoparticles) for catalysts Pt20/SBA-15, Pt40/SBA-1,5 and Pt50/SBA-15, respectively (whereas the ethylene hydrogenation test reveals that the percentage of active sites per nanoparticle were 84.5%, 74%, and 65% respectively).

6.2.4 A Comparison of PtNPs, RhNPs, PdNPs, AuNPs, and CuNPs in the hydrogenative isomerization of MCP

We have observed an improvement of both selectivity and activity of Pt-based catalyst due to the presence of PAMAM. In order to confirm this effect to be general, we have tested other metallic nanoparticle catalysts (Rh, Pd, Au, and Cu). Rh/SBA-15 (that is, Rh40NP-G4OH/SBA-15), Pd/SBA-15 (that is, Pd40NP-G4OH/SBA-15), Au/SBA-15 (that is, Au40NP-G4OH/SBA-15), and Cu/SBA-15 (that is, Cu16NP-G4OH/SBA-15), were synthesized following a similar procedure to the one used for Pt/SBA-15. Characteristics of these five catalysts are reported in Table 4.

Table 4. Characteristics of the catalysts used for the hydrogenation of MCP

catalyst	Metal loading (wt %)	MNPs[b] size (nm)	% of metal active sites[d]	Number of active sites available (atom)[d]
Pt/SBA-15	1.5[a]	1.6	71.3	6.6×10^{18}
Rh/SBA-15	0.8[a]	1.6	73.2	6.8×10^{18}
Pd/SBA-15	0.82[a]	1.6	72.2	6.7×10^{18}
Au/SBA-15	1.51[a]	1.8	66.0	6.1×10^{18}
Cu/SBA-15	0.9[a]	ND[c]	ND	ND
Pt20/SBA-15	1.2	1.2	83.7	6.2×10^{18}
Pt40/SBA-15	1.2	1.6	71.3	5.3×10^{18}
Pt50/SBA-15	1.2	1.9	63.7	4.7×10^{18}

[a]This wt % corresponds to 0.0077 mol %, confirmed by ICP analysis. [b]The size was measured by TEM on the unsupported nanoparticles as it is tricky to measure the size of supported nanoparticle. ND = not determined. [c]The CuNP is too air sensitive to claim a real size by TEM. [d]The % of metal active sites were calculated from the simple hard sphere counting model of a 1.2, 1.6, 1.8, and 1.9 nm nanoparticles.

Rh/SBA-15 and Pd/SBA-15 have demonstrated similar changes in their performance for MCP hydrogenation whereas no reaction was observed with Au/SBA-15 and Cu/SBA-15 as gold and copper are not effective catalysts for C—C bond cleavage. Rh/SBA-15, composed of RhNPs of 1.6 ± 0.2 nm, is known to be a good C—C bond breaking catalysts under homogeneous conditions and is known to perform cracking in heterogeneous reactions. Few publications have reported that a Rh catalyst can achieve ring opening isomerization of MCP efficiently, for example, 89.5% of selectivity as reported by Paàl.[33] Rh/SBA-15 exhibits a higher activity than Pt/SBA-15 at 175 °C (45% vs 20%), and a ring opening selectivity of 82.2% (cracking products 17.2%, and 0.6% for benzene) see Figure 5a. By increasing the temperature, an inversion of the selectivity is observed and much more cracking is observed (45.4% at 200 °C and 74% at 225 °C). The MCP conversion increased by 10% at 225 °C and no reaction is observed at 250 °C. We believe again that it is due to coke formation from intense cracking. The selectivity between the three-ring opening isomers are roughly the same as for Pt/SBA-15 (Figure 5b). To the best of our knowledge, it is the first report of a highly active Rh catalyst at low temperature (see Table 5 and 6 for TOF comparison), moreover at those low temperature isomers, are favored against cracking. Those results indicate once more the importance of the dendrimer as a capping agent.

Table 5. Comparison of TOFs between catalysts Pt/SBA-15, Rh/SBA-15, and Pd/SBA-15 at different temperatures[a]

Catalyst	Temperature (°C)	Molecules consumed (h^{-1})	TOF (h^{-1})
Pt/SBA-15	175	3.2×10^{20}	48.7

Pt/SBA-15	200	1.2×10^{21}	189
Pt/SBA-15	225	1.5×10^{21}	229
Pt/SBA-15	250	1.5×10^{21}	228
Pt/SBA-15	275	1.3×10^{21}	194
Rh/SBA-15	175	7.2×10^{20}	130.9
Rh/SBA-15	200	6.8×10^{20}	122.7
Rh/SBA-15	225	8.8×10^{20}	160.1
Rh/SBA-15	250	0	0
Pd/SBA-15	200	0	0
Pd/SBA-15	225	5.5×10^{19}	8.2
Pd/SBA-15	250	1.9×10^{20}	27.8
Pd/SBA-15	275	3.4×10^{20}	50.2

[a]TOF corresponding to the number of molecules consumed per hour per metal active site.

Table 6. TOFs and selectivity for the MCP hydrogenative isomerisation over different Pt, Pd, Ru, Rh, Fe, and Ir catalysts found in the literature

Catalyst [ref]	Temperature (°C)	Capping agent	Size of NPs (nm)	TOF (h^{-1})	RO/I (%)
Pt/SBA-15	200	PAMAM	1.6	189	99.6
Pt50/SBA-15	225	PAMAM	1.9	334	98.3
Pt/SBA-15[29]	280	PVP	5.2 or 1.5	45 or 19	<20 or <70
Pt/SBA-15[29]	240	PVP	5.2[a]	25	90
Pt/SiO_2 MCF-17[30]	250	PVP	2.5	36	75
Pt/SiO_2[a31]	220	No	2.5	2.2	100
$Pt\text{-}Ru/SiO_2$[31]	160	No	2	23.8	85.6
EUROPT-1Pt/SiO_2[32]	270	No	1.6	2.7	97.7
Pt/Al_2O_3[32]	NM	No	NM	10.8	98
Rh/Al_2O_3[33]	225	No	5 or 1.5	148 or 104	89.5 or 71.2
Rh/SiO_2[33]	225	No	2.5	129.5	84.3
EUROPT-3[34]	275	No	< 1.5	110	NM[b]
Fe-KIT-6[35]	500	No	NM	6.05	24
Fe-KIT-6[35]	200	No	NM	0.0936	100
Pt/Al_2O_3[36]	280	No	2.2	165	97
$Pt\text{-}Ir/Al_2O_3$[36]	280	No	3.4	585	95

[a]Cab-0-Sil, M-5 SiO2 support. [b]Only the percent between the three isomers is mentioned. NO = no capping agent. NM = not mentioned in the publication.

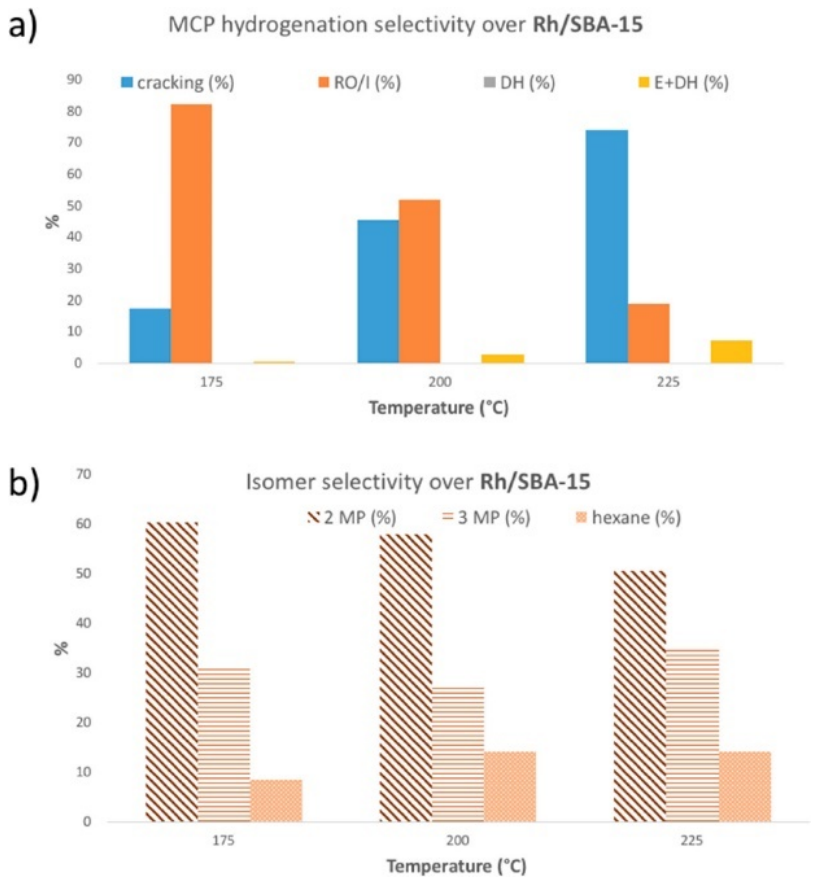

Figure 5. (a) Temperature dependence of MCP hydrogenation selectivity over Rh/SBA-15 and (b) distribution between the three isomers.

The hydrogenative isomerization of MCP on Pd/SBA-15 is also a good example of the effect of the presence of dendrimer on the reaction pathway. First of all, only a 3.43% conversion of MCP was detected at 225 °C, 11.6% at 250 °C, and 20.9% at 275 °C. Moreover, the selectivity of the reaction is also completely different as compares to other Pd catalysts. In term of selectivity we obtained benzene (pathway C) and methyl cyclopentene (pathway D) in preponderance (see Figure 6a). These data are suggestive of an effect of the dendrimer, as Pd selectivity is generally reported to be higher toward the ring-opening products. The selectivity between the three-ring opening isomers is roughly the same as that of the Pt/SBA-15 and Rh/SBA-15 catalysts at similar temperatures (Figure 6b).

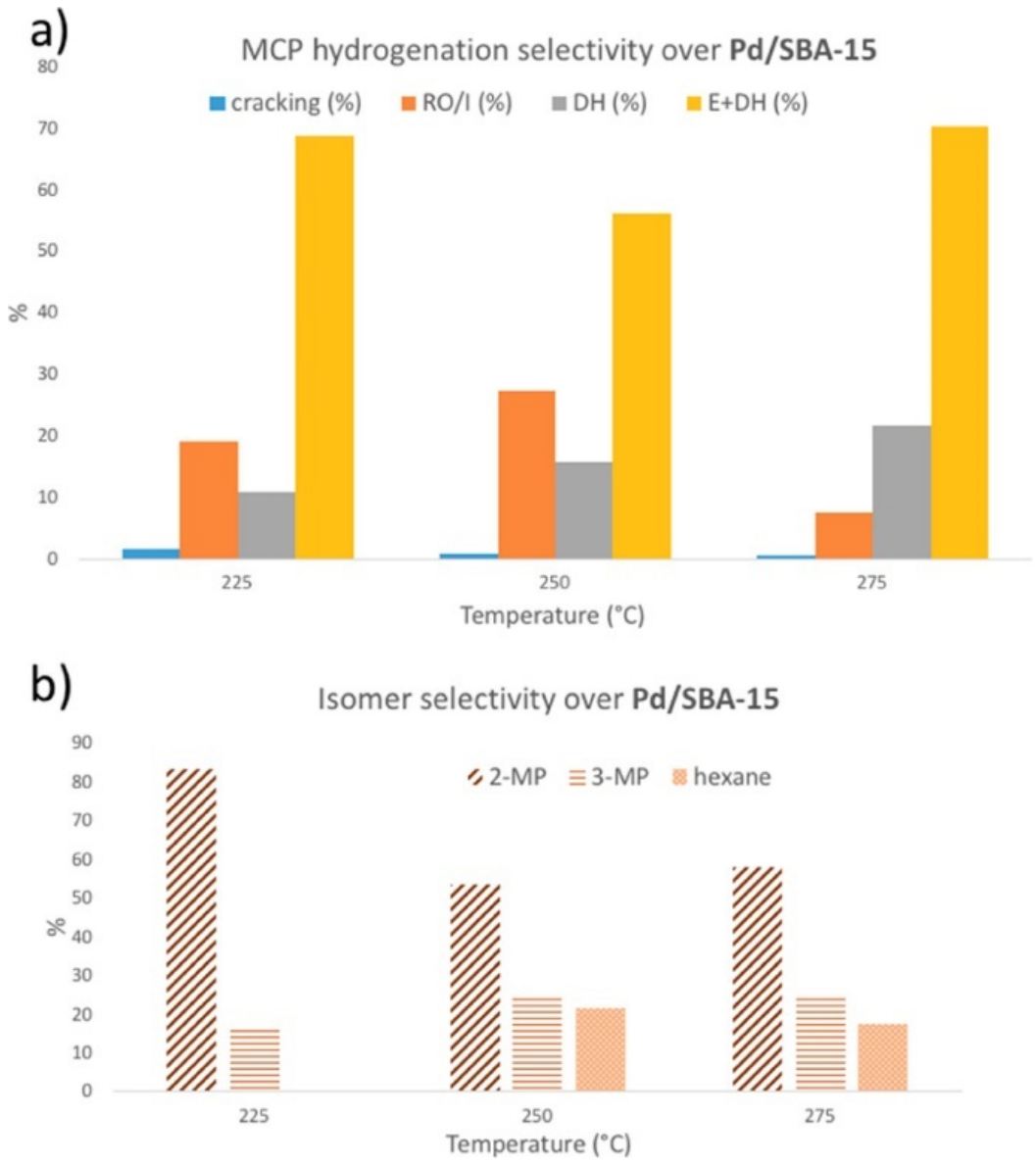

Figure 6. (a) Temperature dependence of MCP hydrogenation selectivity over Pd/SBA-15 and (b) distribution between the three isomers.

TOFs of catalysts Pt/SBA-15, Rh/SBA-15, and Pd/SBA-15 are compared in Table 5. Interestingly, the selectivity trends of the three catalysts are different. Pt prefers follow the pathway A by ring opening hydrogenolysis leading to three noncyclic isomers, Rh prefers the pathway A at 175 °C but the pathway B at higher temperature corresponding to cracking, and Pd prefers the pathways C and D leading to dehydrogenated products. By changing the metal encapsulated inside the dendrimer and supported on SBA-15, the selectivity of the reaction is easily tuned.

To the best of our knowledge, this work is the first attempt to use these catalysts in gaseous phase (flow reactor) above 150 °C. Moreover, these nanoparticles exhibit much more activity and tunable selectivity than colloidal or classically prepared nanoparticles.

Hydrogenation of MCP is a very well-studied reaction but very few catalysts has been found to combine both a high activity and a high selectivity. We attempt to demonstrate the superiority of our catalysts by comparing them to the current literature of MCP hydrogenation (summary of literature data reported in Table 6).

All the catalysts reported in Table 6 are composed of supported nanoparticles on either SiO_2 or Al_2O_3. Most of the catalysts have bare nanoparticles but for the work performed in our group (capping agent polyvinylpyrrolidone or dendrimer). Moreover, we have cited papers that reported NPs close in size to the one used in this work.

In our group, 1.5 nm PtNPs stabilized by PVP and supported on SBA-15 (no difference in activity/selectivity is observed by the changing the support from SBA-15 to MCF-17 there) have been previously used in the MCP hydrogenation and revealed a TOF of 19 h^{-1} at 280 °C, which is 17.6 times lower than TOF of Pt50/SBA-15 at 225 °C. We observed a better selectivity for the ring opening isomers for the dendrimer-capped Pt versus the PVP-capped Pt (96.9% versus 70%).[29] It is generally accepted that smaller NPs are less active than larger ones, in the work of Alayoglu et al. 5.2 nm PVP capped NPs have a TOF of 45 h^{-1} whereas our Pt catalysts have a TOF of 334 h^{-1} (7.4 times) in a similar reactor and conditions. Investigation of the literature indicates the same trend of the better performance of the dendrimer stabilized NPs. The most promising work was done by Paàl et al. using Pt, Ir and Pt–Ir nanoparticles supported on alumina with TOF higher than the one reported here and similar selectivity (97% ring opening). However, to achieve such performance the authors reported temperature between 280 °C-330 °C, while our catalysts only require 200 °C-250 °C indicating a lower activation barrier.[36] High conversions are reported in the literature but those require high reaction temperatures that lead to high cracking and fast deactivation. Our catalysts give 94% conversion with high selectivity toward ring opening and no deactivation is observed at 225 °C.

From our knowledge, the TOFs reported here, up to 334 h^{-1}, are the highest observed for this reaction at low temperatures (see Table 6). Furthermore, the selectivity of the ring opening isomers is also the highest one (up to 99.6%) at high conversion and high TOF.

The high performance of our catalysts could be explained by the presence of the dendrimer.

In fact, we believe that the dendrimer is still present at the surface of the metal at 225 °C when the activity is optimum. Amiridis et al. have demonstrated that temperature above 250 °C and H_2 flow were necessary to remove the dendrimer capping agent at the surface of nanoparticles.[42,43] Zaera et al. have shown that at 250 °C under hydrogen

pretreatment, only 40% of the starting dendrimer was removed.[22] This result induced that our catalysts are composed of dendrimer moieties. According to our results, conversely with previously reported on CO reaction,[42,44] the presence of the dendrimer does not block the reactions sites (see ethylene hydrogenation in SI). Therefore, we believe that the dendrimer (dendrimer moieties) is essential to the high performance observed in the present work. The possible reasons for the observed enhancement of activity and the drastic changes of selectivity (i.e., Rh and Pd) are exposed hereafter.

(1) The dendrimer stabilizes the nanoparticle, preventing sintering, during the whole reaction until 250 °C. In the present work, sintering was only observed at 275 °C (leading to deactivation of the catalyst) due to the destruction of the dendrimer and this is in agreement with Amiridis' work. According to Zaera, the sintering of PtNPs stabilized by dendrimers supported on silica in observed under hydrogen pretreatment only from 350 °C.[22,44]

(2) PAMAM dendrimers are composed of high density electron rich tertiary amines and amide that are well-known in homogeneous catalysis to activate catalysts. The active sites could be electron enriched by the dendrimer/dendrimer moieties, allowing a faster reaction on these sites.

(3) The tree-shape of the dendrimer is stabilizing the reactant or any of the catalytic steps by steric effect (preferential orientation, enhance adsorption/desorption of reactant and products, etc.) leading to a lower activation barrier hence the better turnover frequency obtained.

At this point, we are unable to determine which of these explanations is the best, as the results observed can be linked to any or all of the theories proposed. However, it is unquestionable that G4OH dendrimer is essential to obtaining a new generation of highly active and selective catalyst.

6.3 Conclusions

In conclusion, we have discovered that nanoparticles stabilized by PAMAM dendrimer are very active for heterogenenous reaction in gas phase flow reactor at temperatures above 150 °C, which has never been demonstrated before this work. As an example, the multipathway hydrogenation of MCP was performed with MNPs (M = Pt, Pd, Rh, Au, and Cu) stabilized by PAMAM. Pathway A implying a C—C sp^3 bond breaking leading to three isomers is the ideal target in most cases over benzene formation (pathway C) or cracking products (pathway B) for a certain number of reasons. We found that Pt stabilized by fourth generation dendrimer and supported on SBA-15 (1.2–1.5 wt %) was the most active catalyst reported for the MCP hydrogenative isomerization at 200–225 °C with high conversion, a TOF of 334 h^{-1}, and a very high selectivity toward acyclic C6 isomers (up to 99.6%). The interesting behavior of Rh/SBA-15 leading to majority ring opening isomers at 175 °C with TOF of 130.9 (h^{-1}) and good conversion and leading to cracking alkanes at higher temperatures is also a

surprising discovery. It seems that all the NPs stabilized by dendrimers (except Au and Cu) bring a high activity for this reaction. We believe that this reactivity could be explained by the well-stabilized NPs thanks to the dendrimer capping agent, which at the same time can activate the surface with the electron-donating ligand amine ligands (like in homogeneous catalysts) or by letting the surface be free of steric effect thanks to its spongy shape or by stabilizing/orienting the reactants. The tunable selectivity from one metal to another one is also an attractive characteristic of this family of dendrimer-stabilized catalysts. The research presented here opens the field of dendrimer catalysts in the gas phase heterogeneous catalytic field.

6.4 References

1. Buhleier, E.; Wehner, W.; VÖGtle, F. "Cascade"- and "Nonskid-Chain-like" Syntheses of Molecular Cavity Topologies. *Synthesis* **1978**, *1978*, 155-158.
2. Fischer, M.; Vögtle, F. Dendrimers: from design to application—a progress report. *Angew. Chem. Int. Ed* **1999**, *38*, 884-905.
3. Denkewalter, R.; Kolc, J.; Lukasavage, W. US Patent 4,289,872, 1981. *There is no corresponding record for this reference* **1981**.
4. Tomalia, D. A.; Baker, H.; Dewald, J.; Hall, M.; Kallos, G.; Martin, S.; Roeck, J.; Ryder, J.; Smith, P. A New Class of Polymers: Starburst-Dendritic Macromolecules. *Polym J* **1985**, *17*, 117-132.
5. Newkome, G. R.; Yao, Z.; Baker, G. R.; Gupta, V. K. Micelles. Part 1. Cascade molecules: a new approach to micelles. A [27]-arborol. *The Journal of Organic Chemistry* **1985**, *50*, 2003-2004.
6. Hawker, C. J.; Frechet, J. M. J. Preparation of polymers with controlled molecular architecture. A new convergent approach to dendritic macromolecules. *J. Am. Chem. Soc.* **1990**, *112*, 7638-7647.
7. Crooks, R. M.; Zhao, M.; Sun, L.; Chechik, V.; Yeung, L. K. Dendrimer-Encapsulated Metal Nanoparticles: Synthesis, Characterization, and Applications to Catalysis. *Acc. Chem. Res.* **2001**, *34*, 181-190.
8. Zhao, M.; Crooks, R. M. Homogeneous hydrogenation catalysis with monodisperse, dendrimer-encapsulated Pd and Pt nanoparticles. *Angew. Chem. Int. Ed* **1999**, *38*, 364-365.
9. Giacalone, F.; Campisciano, V.; Calabrese, C.; La Parola, V.; Syrgiannis, Z.; Prato, M.; Gruttadauria, M. Single-Walled Carbon Nanotube–Polyamidoamine Dendrimer Hybrids for Heterogeneous Catalysis. *ACS Nano* **2016**, *10*, 4627-4636.
10. Bernechea, M.; de Jesús, E.; López-Mardomingo, C.; Terreros, P. Dendrimer-Encapsulated Pd Nanoparticles versus Palladium Acetate as Catalytic Precursors in the Stille Reaction in Water. *Inorg. Chem.* **2009**, *48*, 4491-4496.
11. Deraedt, C.; Salmon, L.; Etienne, L.; Ruiz, J.; Astruc, D. "Click" dendrimers as efficient nanoreactors in aqueous solvent: Pd nanoparticle stabilization for sub-ppm Pd

catalysis of Suzuki-Miyaura reactions of aryl bromides. *Chem. Commun.* **2013**, *49*, 8169-8171.
12. Niu, Y.; Yeung, L. K.; Crooks, R. M. Size-Selective Hydrogenation of Olefins by Dendrimer-Encapsulated Palladium Nanoparticles. *J. Am. Chem. Soc.* **2001**, *123*, 6840-6846.
13. Boronoev, M. P.; Zolotukhina, A. V.; Ignatyeva, V. I.; Terenina, M. V.; Maximov, A. L.; Karakhanov, E. A. Palladium Catalysts Based on Mesoporous Organic Materials in Semihydrogenation of Alkynes. *Macromol. Symp.* **2016**, *363*, 57-63.
14. Dhiman, M.; Chalke, B.; Polshettiwar, V. Efficient Synthesis of Monodisperse Metal (Rh, Ru, Pd) Nanoparticles Supported on Fibrous Nanosilica (KCC-1) for Catalysis. *ACS Sustainable Chemistry & Engineering* **2015**, *3*, 3224-3230.
15. Johnson, J. A.; Makis, J. J.; Marvin, K. A.; Rodenbusch, S. E.; Stevenson, K. J. Size-Dependent Hydrogenation of p-Nitrophenol with Pd Nanoparticles Synthesized with Poly(amido)amine Dendrimer Templates. *J. Phys. Chem. C* **2013**, *117*, 22644-22651.
16. Esumi, K.; Isono, R.; Yoshimura, T. Preparation of PAMAM− and PPI−Metal (Silver, Platinum, and Palladium) Nanocomposites and Their Catalytic Activities for Reduction of 4-Nitrophenol. *Langmuir* **2004**, *20*, 237-243.
17. Gatard, S.; Salmon, L.; Deraedt, C.; Ruiz, J.; Astruc, D.; Bouquillon, S. Gold Nanoparticles Stabilized by Glycodendrimers: Synthesis and Application to the Catalytic Reduction of 4-Nitrophenol. *Eur. J. Inorg. Chem.* **2014**, *2014*, 2671-2677.
18. Deraedt, C.; Wang, D.; Salmon, L.; Etienne, L.; Labrugère, C.; Ruiz, J.; Astruc, D. Robust, Efficient, and Recyclable Catalysts from the Impregnation of Preformed Dendrimers Containing Palladium Nanoparticles on a Magnetic Support. *Chemcatchem* **2015**, *7*, 303-308.
19. Huang, W.; Kuhn, J. N.; Tsung, C.-K.; Zhang, Y.; Habas, S. E.; Yang, P.; Somorjai, G. A. Dendrimer Templated Synthesis of One Nanometer Rh and Pt Particles Supported on Mesoporous Silica: Catalytic Activity for Ethylene and Pyrrole Hydrogenation. *Nano Lett.* **2008**, *8*, 2027-2034.
20. Witham, C. A.; Huang, W.; Tsung, C.-K.; Kuhn, J. N.; Somorjai, G. A.; Toste, F. D. Converting homogeneous to heterogeneous in electrophilic catalysis using monodisperse metal nanoparticles. *Nat. Chem.* **2010**, *2*, 36-41.
21. Gross, E.; Liu, J. H.-C.; Toste, F. D.; Somorjai, G. A. Control of selectivity in heterogeneous catalysis by tuning nanoparticle properties and reactor residence time. *Nat. Chem.* **2012**, *4*, 947-952.
22. Albiter, M. A.; Morales, R.; Zaera, F. Dendrimer-based synthesis of Pt catalysts for hydrocarbon conversion. *Appl. Catal., A* **2011**, *391*, 386-393.
23. Ye, R.; Yuan, B.; Zhao, J.; Ralston, W. T.; Wu, C.-Y.; Unel Barin, E.; Toste, F. D.; Somorjai, G. A. Metal Nanoparticles Catalyzed Selective Carbon–Carbon Bond Activation in the Liquid Phase. *J. Am. Chem. Soc.* **2016**, *138*, 8533-8537.

24. Brandenberger, S. G.; Callender, W. L.; Meerbott, W. K. Mechanisms of methylcyclopentane ring opening over platinum-alumina catalysts. *J. Catal.* **1976**, *42*, 282-287.
25. Zhuang, Y.; Frennet, A. Kinetic studies of methylcyclopentane ring opening on EuroPt-1 (Pt/SiO2). *Appl. Catal., A* **1999**, *177*, 205-217.
26. Galperin, L. B.; Bricker, J. C.; Holmgren, J. R. Effect of support acid–basic properties on activity and selectivity of Pt catalysts in reaction of methylcyclopentane ring opening. *Appl. Catal., A* **2003**, *239*, 297-304.
27. Teschner, D.; Paál, Z.; Duprez, D. The effects of hydrogen pressure and temperature on the methylcyclopentane conversion on Rh catalysts. *Catal. Today* **2001**, *65*, 185-190.
28. Samoila, P.; Boutzeloit, M.; Especel, C.; Epron, F.; Marécot, P. Selective ring-opening of methylcyclopentane on platinum-based bimetallic catalysts. *Appl. Catal., A* **2009**, *369*, 104-112.
29. Alayoglu, S.; Aliaga, C.; Sprung, C.; Somorjai, G. A. Size and Shape Dependence on Pt Nanoparticles for the Methylcyclopentane/Hydrogen Ring Opening/Ring Enlargement Reaction. *Catal. Lett.* **2011**, *141*, 914-924.
30. Na, K.; Alayoglu, S.; Ye, R.; Somorjai, G. A. Effect of Acidic Properties of Mesoporous Zeolites Supporting Pt Nanoparticles on Hydrogenative Conversion of Methylcyclopentane. *J. Am. Chem. Soc.* **2014**, *136*, 17207-17212.
31. Diaz, G.; Garin, F.; Maire, G.; Alerasool, S.; Gonzalez, R. D. Hydrogenolysis of methylcyclopentane and isomerization of 2-methylpentane over well characterized silica-supported platinum-ruthenium catalysts. *Appl. Catal., A* **1995**, *124*, 33-46.
32. Vaarkamp, M.; Dijkstra, P.; Vangrondelle, J.; Miller, J. T.; Modica, F. S.; Koningsberger, D. C.; Vansanten, R. A. The Effect of Hydrogen Partial-Pressure on Methylcyclopentane Ring-Opening. *J. Catal.* **1995**, *151*, 330-337.
33. Teschner, D.; Duprez, D.; Paál, Z. Reactivity of the hydrocarbon C–C bonds as a function of the reaction conditions in the conversion of C6 alkanes and methylcyclopentane over Rh catalysts. *J. Mol. Catal. A: Chem.* **2002**, *179*, 201-212.
34. Kramer, R.; Fischbacher, M. Hydrogen pretreatment effects on the hydrogenolysis of methylcyclopentane on Pt/SiO2 and Pt/Al2O3 catalysts. *J. Mol. Catal.* **1989**, *51*, 247-259.
35. Merkache, R.; Fechete, I.; Maamache, M.; Bernard, M.; Turek, P.; Al-Dalama, K.; Garin, F. 3D ordered mesoporous Fe-KIT-6 catalysts for methylcyclopentane (MCP) conversion and carbon dioxide (CO2) hydrogenation for energy and environmental applications. *Appl. Catal., A* **2015**, *504*, 672-681.
36. Poupin, C.; Pirault-Roy, L.; Fontaine, C. L.; Tóth, L.; Chamam, M.; Wootsch, A.; Paál, Z. Promising PtIr, catalysts for hydrocarbon transformation: Comparison of different preparation methods. *J. Catal.* **2010**, *272*, 315-319.
37. Bai, X.; Sachtler, W. M. H. Methylcyclopentane conversion catalysis by zeolite encaged palladium clusters and palladium-proton adducts. *J. Catal.* **1991**, *129*, 121-129.

38. Kuhn, J. N.; Tsung, C.-K.; Huang, W.; Somorjai, G. A. Effect of organic capping layers over monodisperse platinum nanoparticles upon activity for ethylene hydrogenation and carbon monoxide oxidation. *J. Catal.* **2009**, *265*, 209-215.
39. Flaherty, D. W.; Hibbitts, D. D.; Iglesia, E. Metal-Catalyzed C–C Bond Cleavage in Alkanes: Effects of Methyl Substitution on Transition-State Structures and Stability. *J. Am. Chem. Soc.* **2014**, *136*, 9664-9676.
40. Zhao, Z.-J.; Moskaleva, L. V.; Rösch, N. Ring-Opening Reactions of Methylcyclopentane over Metal Catalysts, M = Pt, Rh, Ir, and Pd: A Mechanistic Study from First-Principles Calculations. *ACS Catal.* **2013**, *3*, 196-205.
41. Paál, Z. Hydrocarbon product selectivity: a tool for characterizing the active state of platinum catalysts. *Catal. Today* **1988**, *2*, 595-604.
42. Deutsch, D. S.; Lafaye, G.; Liu, D.; Chandler, B.; Williams, C. T.; Amiridis, M. D. Decomposition and Activation of Pt-Dendrimer Nanocomposites on a Silica Support. *Catal. Lett.* **2004**, *97*, 139-143.
43. Lafaye, G.; Williams, C. T.; Amiridis, M. D. Synthesis and Microscopic Characterization of Dendrimer-Derived Ru/Al2O3 Catalysts. *Catal. Lett.* **2004**, *96*, 43-47.
44. Albiter, M. A.; Crooks, R. M.; Zaera, F. Adsorption of Carbon Monoxide on Dendrimer-Encapsulated Platinum Nanoparticles: Liquid versus Gas Phase. *J. Phys. Chem. Lett.* **2010**, *1*, 38-40.

Chapter 7 - A Comparison of Photocatalytic Activities of Gold Nanoparticles Following Plasmonic and Interband Excitation and a Strategy for Harnessing Interband Hot Carriers for Solution Phase Photocatalysis

(This chapter covers similar material as in Zhao, J.; Nguyen, S. C.; Ye, R.; Ye, B.; Weller, H.; Somorjai, G. A.; Alivisatos, A. P.; Toste, F. D. *ACS Cent. Sci.* **2017**, *3*, 482-488. – reproduced with permission, copyright 2017 American Chemical Society.)

Abstract

Light driven excitation of gold nanoparticles (GNPs) has emerged as a potential strategy to generate hot carriers for photocatalysis through excitation of localized surface plasmon resonance (LSPR). In contrast, carrier generation through excitation of interband transitions remains a less explored and underestimated pathway for photocatalytic activity. Photoinduced oxidative etching of GNPs with $FeCl_3$ was investigated as a model reaction in order to elucidate the effects of both types of transitions. The quantitative results show that interband transitions more efficiently generate hot carriers and that those carriers exhibit higher reactivity as compared to those generated solely by LSPR. Further, leveraging the strong π-acidic character of the resulting photogenerated Au^+ hole, an interband transition induced cyclization reaction of alkynylphenols was developed. Notably, alkyne coordination to the Au^+ hole intercepts the classic oxidation event and leads to the formation of the catalytically active gold clusters on subnanometer scale.

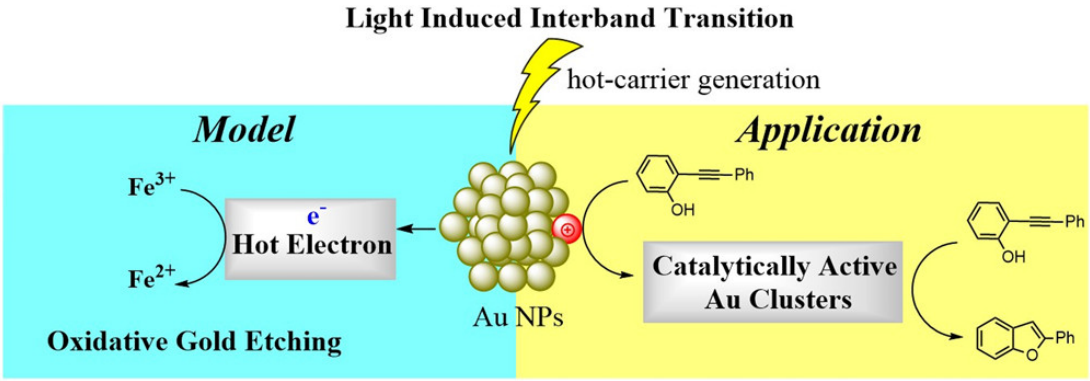

7.1 Introduction

Plasmonic noble metal nanoparticles (such as those of Au, Ag or Cu) exhibit strong light absorption through excitation of a localized surface plasmon resonance (LSPR). The strong light absorption, robust nature, recyclability, and large surface areas of these nanoparticles render them candidates as photocatalytic materials. Therefore, these nanoparticles have recently been examined as photocatalysts for selective chemical synthesis by harvesting visible light to drive reactions at ambient conditions.[1,2] Although the catalytic mechanism is not fully understood, hot carriers (here referred to as high kinetic energy carriers) generated from surface plasmon excitation have been strongly implicated for driving some catalytic reactions.[1,3,4] These plasmonic noble metal nanoparticles also have strong absorption on the high-energy side of their plasmon resonances due to intrinsic interband transitions (Figure 1B and 2A). Limited studies of gold nanoparticles supported on metal oxides show higher photocatalytic activities in oxidation reactions for interband transitions as compared to that of LSPR. The higher potential for the interband transition results from the creation of a hot hole with a high reduction potential in the *d* band and a hot electron, to some extent, in the *sp* band.[5-7]

To gain insights into how hot carriers are generated under specific excitation wavelength, recent theoretical work predicted that photoexcitation of Au or Ag nanoparticles with photon energy below the interband energy can create hot s electrons or hot s holes in the intraband. However, when the photon energy is above the interband energy threshold, more hot carriers are generated from direct excitation of *d*-*sp* transitions even though these carriers do not have as high kinetic energy as those produced in the intraband transition.[8] These findings imply that photoexcitation at surface plasmon resonance, which usually has lower energy than the interband transition, does not produce hot carriers terribly efficiently. This is not surprising when considering how the energy of an absorbed photon is divided in these two excitation regimes. In a classical description (Figure 1A, left), the LSPR photon energy is split between thousands of carriers in the sp band and their distribution among all continuous energy states approximately follows a Fermi–Dirac distribution after the LSPR decays.[1] Consequently, the probability of having high-energy carriers is very low (Figure 1A, right). A more rigorous description is a quantum mechanical picture of superposition of many single-electron, quantized energy transitions (Figure 1A, right).[4] When considering momentum conservation in this discrete energy picture, the hot carrier generation is relatively weak because there is only a limited joint density of states in the particles with finite momentum that are matched with the LSPR wave vector.[8] In contrast, interband transitions efficiently create hot carriers because the photon energy is concentrated to a hot electron-hole pair (Figure 1B, right). In this regard, an important question is raised: is the ability to generate higher kinetic energy carriers (i.e. hotter carriers) by LSPR responsible for the observed light-driven catalysis by plasmonic metal nanoparticles, as

compared to interband transitions, which produce a larger number of “cooler” hot carriers? In this work, we provide evidence to support the latter mechanism.

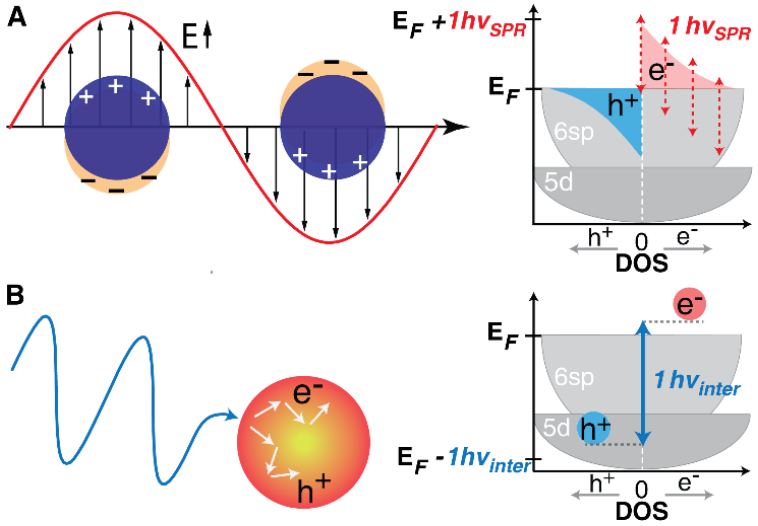

Figure. 1. Carriers generated after photoexciting metallic nanoparticles at the LSPR and interband transition. (**A**) A classical description of LSPR shows oscillation of collective electrons driven by the electric field (left). The LSPR decay generates a population of hot carriers at various energies (right). The integral energy of both e^- (red area) and h^+ (blue) occupation is equivalent to a single photon energy. A quantum mechanical description of LSPR uses red arrows to represent a superposition of multiple isoenergetic, single-electron transitions when one photon is absorbed. (**B**) Interband transition results from absorption of a higher energy photon (left) and directly generates an e^--h^+ pair (right).

7.2 Results and discussion:

7.2.1 Photoinduced etching of gold nanorods

Recent research on photocatalysis of plasmonic nanoparticles has shifted heavily toward elucidating catalytic activity originating from LSPR and away from catalysis induced by interband transitions. In contrast, there is a dearth of experimental assessment of these two excitation pathways and the resulting mechanism of catalysis. Herein, the photocatalytic activities of gold nanoparticles following LSPR and interband excitation are compared in two reactions: the oxidative etching of gold nanoparticles with $FeCl_3$ and the cyclization of 2-(phenylethynyl) phenol. Colloidal gold nanorods (GNRs) and spheres (GNSs) were chosen as photo-catalysts to avoid any affect from supporting materials. Moreover, GNRs have longitudinal LSPR absorption that is well separated from the interband transition absorption, allowing the evaluation of only the contribution of LSPR to the photocatalysis. Comparison of the catalytic performance of the particles

as a function of the excitation wavelength supports the conclusion that interband transitions provide for greater catalytic activity than direct LSPR.

In the first reaction, the etching rate of GNRs and GNSs by a $FeCl_3$ solution in the dark, and LSPR and interband excitations was compared. GNRs and GNSs gave similar results in this reaction; therefore GNRs were selected for examination. Previous studies have shown that, under dark conditions, etching occurs selectively at the tips of the GNRs and follows equation (1) because the gold ion product creates a strongly coordinated complex with halide ions so that the reduction potential of Au^+/Au is lower than that of Au^{3+}/Au and Fe^{3+}/Fe^{2+}.[9] To quantify the reaction rate, the blue-shifting rate of the longitudinal LSPR absorption was measured (Figure S2). This absorption peak is an effective probe for reaction rate as it is well separated from absorption of other reactants and products in solution. TEM and UV-Vis spectroscopy proved a proportional dependence of this blue-shifting rate to reaction rate due to the selective etching at the GNR tips (see SI). A first order rate constant of $k_{dark} = 3.41 \times 10^{-7}$ s^{-1} was measured. The reaction showed first order dependence on $[Fe^{3+}]$, and an activation energy of 2.87 kcal/mol. These observations are consistent with homogenous reaction with low absorption of Fe^{3+} on the GNR surface.

$$Fe^{3+}_{(aq)} + Au_{(s)} \rightarrow Fe^{2+}_{(aq)} + Au^{+}_{(aq)} \quad (1)$$

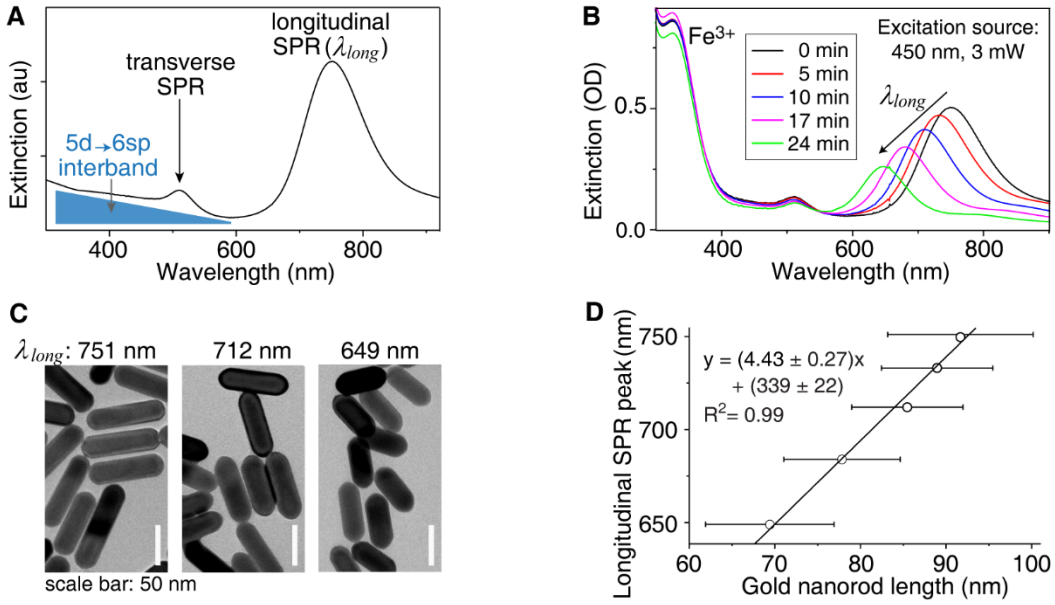

Figure. 2. Photo-induced fast etching of GNRs in an $FeCl_3$ solution at room temperature. (**A**) Optical spectra of colloidal CTAB capped GNRs in water with depiction of the interband and LSPR absorptions. (**B**) Spectral progression of a typical reaction under 450 nm excitation. (**C**) Representative TEM images showing tip etching of GNRs in B. (**D**)

Linear dependence of λ_{long} vs. GNR length (data in Table S3). The fitting does not propagate the errors in length to the final errors of intercept and slope values.

In order to study the light driven reaction, a monochromatic light source from a Xenon lamp equipped with narrow band-pass fitter (10-12 nm FWHM) was used and the reaction was monitored via a UV-Vis spectrometer after various irradiation times (Figure 2B). TEM inspection shows a similar tip etching profile as in the reaction performed in the dark (Figure 2C). Upon photoexcitation, the etching reaction occurred through a pathway that generates soluble Au^{3+} as an intermediate that further etches the GNRs (see Eq S8, S9 in SI). However, the overall reaction still follows equation (1). The reaction rate was again measured via the blue-shifting rate of the longitudinal LSPR absorption (Figure 2D, 3A, 3B). At first glance, the etching rate appears faster under photoexcitation. Noticeably, interband excitation resulted in the highest etching rate while the rate following longitudinal LSPR excitation showed only an incremental difference as compared to k_{dark} (Table S1). Kinetics studies confirmed the first order of $[Fe^{3+}]$ in the rate equation and the linear dependence of the reaction rate to the excitation power (SI). Moreover, the increase in local temperature around the GNRs is very small (< 1K) and the rise in temperature of the reaction solution is just few degrees above room temperature (Table S1) under our experimental conditions, and therefore the photothermal enhancement of the reaction rate can be ignored.[10,11] Taken together, these observations support the hypothesis that photoexcitation is responsible for promoting the etching reaction.

Since the reaction rate constant increased linearly with the photon flux, the rate constant, $k_{excitation}$, was normalized per single photon absorbed so that the rate can be compared properly across excitation wavelengths (Figure 3C). Strikingly, the rate constant was three to four orders of magnitude higher for the interband transition as compared to the longitudinal LSPR. The rate in the region of 480 to 600 nm excitation does not show a catalytic enhancement due to the transverse LSPR. In fact, the rate in this region was still very high as compared to the longitudinal LSPR due to the tail of the interband absorption starting at ~ 600 nm.[12] The quantum yield also exhibited a similar trend (Figure S10).

A stepwise mechanism for the etching reaction is proposed (Figure 3D). The first absorbed photon promotes an interband transition that results in a hot electron that reduces Fe^{3+} on the surface of the GNR to give an Fe^{2+} product and effectively leaves a positive charge on the GNRs. This step is repeated three times to produces an Au^{3+} product. The Au^{3+} further reacts with the GNRs to give the final product Au^{+}. This mechanism is supported by our detection of Au^{3+} intermediates, the observation of Au^{3+} further etched GNRs immediately after stopping irradiation, and that hole scavengers (acetone, methanol) resulted in decreased reaction rates (SI). With this mechanism of hot carriers catalyzing the reaction, the aforementioned reaction rates and quantum yield

measurements indicate a significantly better efficiency of generating hot carriers for catalysis via interband transition as compared to direct surface plasmon excitation. These observations and conclusions beg the next question: can this mechanism be harnessed effectively for catalysis in liquid solution?

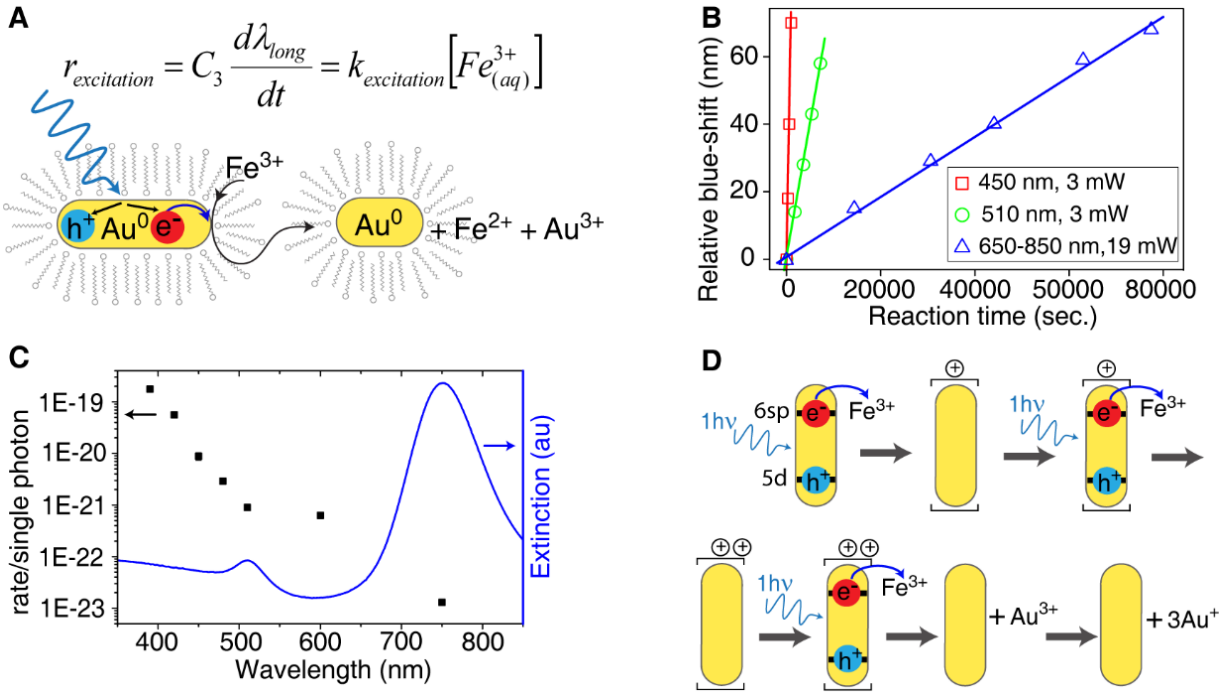

Figure. **3.** Kinetic studies of photo-induced fast etching of GNRs in an $FeCl_3$ solution at room temperature. (**A**) Illustration of that photoexcitation promotes fast etching, and the reaction rate is measured via the blue-shifting rate of the longitudinal SPR absorption (SI). (**B**) The etching rates at various wavelengths and absorbed photon powers. (**C**) Reaction rate normalized to each single photon absorbed, with respect to optical spectra of GNRs. (**D**) Proposed mechanism of the etching reaction.

7.2.2 Photoinduced gold nanoparticle catalysis

Over the last decades, several studies involving light driven oxidation[13-20] and reduction[21-28] reactions catalyzed by semiconductor supported gold nanoparticles (GNPs) excited at their plasmon resonance have been described.[29] In these studies, a semiconductor support is often required to perform the electron-hole separation. Notably, the probability of interband transition, based on the intensity of optical absorption, accounts for roughly 50% of the overall optical absorprion at the transverse LSPR frequency of GNRs or at the single LSPR frequency of GNSs. Therefore, we hypothesized that photocatalysis activities observed at the plasmon frequency in some

of these studies might originate from the hidden tail of the interband transition similar to those observed in the etching study described above.

Photoinduced nanoparticle-catalyzed redox reactions are proposed to occur by a mechanism involving transfer of a hot electron on the surface of the semiconductor bulk, resulting in formation of a hole at the metal. In accord with this classic operational mode and the mechanism proposed above for carrier generation in GNPs via interband transition, we envisioned improved generation of hot carriers for catalysis. More specifically, we posited that the photogenerated Au^{+} hole would have strong π-acidic character,[30-33] which could be leverage for alkyne activation to intercept the oxidation event and drive to downstream catalysis.

On the basis of this hypothesis, 2-(phenylethynyl) phenol was chosen as a model substrate and the corresponding cyclization reaction has been previously studied using gold nanoparticle catalysts and chemical oxidants.[34] CTAB-coated gold nanospheres with 40 nm diameter were initially used as catalysts in the cyclization. Additional CTAB was necessary for stabilizing the catalyst and solublizing the alkynyl phenol into the aqueous media. The GNS-catalyzed reaction at 60 °C under 26 W household fluorescent compact light (CFL) irradiation produced 2-phenyl benzofuran in excellent yield (99%). On the other hand, blank and dark experiments in the absence of the catalyst and light irradiation respectively gave only trace amounts of the benzofuran product (<5%). Given these observations, the influence of incident light on the performance of cyclization was studied using Xenon light with various wavelengths ranging from 390 nm to 660 nm with normalized incident photon numbers (Figure 4A). The studies found that the reaction proceeded with poor chemical conversions under the irradiation of light with wavelengths ranging from 480 nm to 660 nm. Notably, the low conversion at LSPR suggests that the cyclization was not driven effectively by the local surface plasmonic effect. On the other hand, nearly quantitative yields of the desired benzofuran were obtained when irradiating the reaction mixture in the near ultraviolet region (390 nm and 420 nm). The same trend in reaction conversions was obtained when using GNSs with various diameters as well as GNRs with different aspect ratios (see SI). In addition, a nearly linear relationship between the conversion of phenol and the power of the incident light was established (Figure 4B). These results advocate for a mechanism wherein hot carriers from interband excitation have a dramatic impact on the performance of cyclization.

In order to gain further insight into the mechanism of the photocatalysis, plot-time-conversion studies were performed under both “Light-Always-On” and “Light-On/Off” conditions (Figure 4C). A reaction-induction period with “light-on” of 20 minutes was observed, after which the product was steadily formed even without further light irradiation. Examination of the supernatant (see SI) revealed that during the irradiation period a soluble catalyst was formed in situ from the GNPs. Most notably, several subnanosized Au_2 and Au_4 clusters complexed with the phenol substrates were

identified in the supernatant solution by HR-ESI mass spectroscopy (Figure 4D). In accord with observations of Corma[35] and Hutchings,[36] these subnanosized clusters exhibit striking reactivity as catalysts in the cyclization reaction. In terms of scope, alkynyl phenols with steric or electronic modifications on both arenes were found to be compatible under the same reaction conditions, affording the corresponding benzofurans in good yields (see SI).

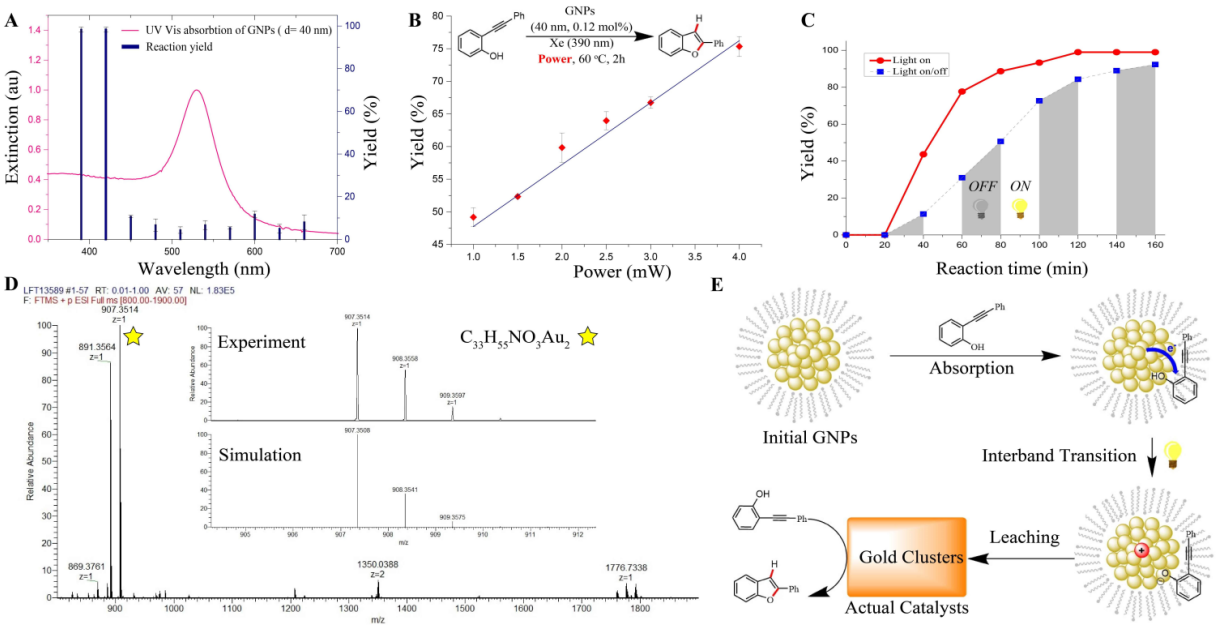

Figure. **4**. Photoinduced gold nanoparticle catalysis. (**A**) UV-Vis absorption of GNSs (diameter = 40 nm) and study on the catalytic activities of aforementioned GNSs using Xenon light with various wavelength, number of incident photons was normalized. (**B**) The power dependence study of catalytic reaction using GNSs as catalyst and Xenon lamp with 390 nm filter (**C**) plot-time-conversion studies under both “Light-Always-On” (red) and “Light-On/Off” (gray) conditions, pink shadow mains during that period, light was turned off and the “Light-On/Off” reaction was undergoing dark conditions, 23W CFL was used as light source. (**D**) The major Au_2 cluster formed in situ in supernatant and detected by HR-ESI mass spectroscopy. See HR-ESI assignment of other Au_2 and Au_4 clusters in SI. (**E**) Proposed mechanism of the leaching process of GNPs.

By analogy to the iron-promoted etching of GNPs, a mechanism involving initial interaction of alkynyl phenol on the GNPs surface was proposed (Figure 4E). This alkynyl phenol substrate acts as the electron acceptor (much like Fe^{3+}) for the hot electron produced from the light-driven interband transition. Subsequent oxidation on the Au^{+} hole and strong alkyne coordination to gold generates the corresponding nanoclusters that are leached into the solution. Compared to our previous catalysis[34,37-43]

in the use of dendrimers capped GNPs with iodonium oxidants, the model phenol substrate plays a key role of not only an oxidant of GNPs but also a stabilizing ligand in the forming cluster.

7.3 Conclusions

While localized surface plasmon resonance (LSPR) provides a powerful platform for nanoparticle catalysis, our studies suggest that in some cases interband transitions should be considered as an alternative mechanism of light-driven nanoparticle catalysis. The benefits already demonstrated by plasmonic nanostructures as catalysts provided the impetus for examining complementary activation modes based on the metal nanoparticle itself. Leveraging these transitions has the potential to provide a means to highly active catalysis modes that would otherwise be challenging to access. For example, only a few methods have been reported for the preparation of highly active metal catalysts on a subnanosized scale, thus limiting their exploitation and study in catalysis.[44] This work suggests a novel and facile strategy for the formation of highly active gold nanocluster catalysts by light illumination of the interband transitions in the presence of the appropriate substrate. Finally, these studies implicated interband transitions, rather than LSPR, as important for the specific reactions and catalysts under study and should be applied judiciously beyond that. Indeed, it is likely that the activation mode will depend on catalyst features (metal, size, support) and the reaction and, therefore, warrants careful evaluation.

7.4 References

1. Brongersma, M. L.; Halas, N. J.; Nordlander, P. Plasmon-induced hot carrier science and technology. *Nat Nano* **2015**, *10*, 25-34.

2. Linic, S.; Aslam, U.; Boerigter, C.; Morabito, M. Photochemical transformations on plasmonic metal nanoparticles. *Nat. Mater.* **2015**, *14*, 567-576.

3. Brus, L. Plasmon-driven chemical synthesis: Growing gold nanoprisms with light. *Nat. Mater.* **2016**, *15*, 824-825.

4. Moskovits, M. The case for plasmon-derived hot carrier devices. *Nat Nano* **2015**, *10*, 6-8.

5. Zhu, H.; Chen, X.; Zheng, Z.; Ke, X.; Jaatinen, E.; Zhao, J.; Guo, C.; Xie, T.; Wang, D. Mechanism of supported gold nanoparticles as photocatalysts under ultraviolet and visible light irradiation. *Chem. Commun.* **2009**, 7524-7526.

6. Liu, L.; Li, P.; Adisak, B.; Ouyang, S.; Umezawa, N.; Ye, J.; Kodiyath, R.; Tanabe, T.; Ramesh, G. V.; Ueda, S.; Abe, H. Gold photosensitized SrTiO3 for visible-light water oxidation induced by Au interband transitions. *Journal of Materials Chemistry A* **2014**, *2*, 9875-9882.

7. Hou, W.; Hung, W. H.; Pavaskar, P.; Goeppert, A.; Aykol, M.; Cronin, S. B. Photocatalytic Conversion of CO2 to Hydrocarbon Fuels via Plasmon-Enhanced Absorption and Metallic Interband Transitions. *ACS Catal.* **2011**, *1*, 929-936.

8. Bernardi, M.; Mustafa, J.; Neaton, J. B.; Louie, S. G. Theory and computation of hot carriers generated by surface plasmon polaritons in noble metals. *Nat. Commun.* **2015**, *6*, 7044.
9. Zou, R.; Guo, X.; Yang, J.; Li, D.; Peng, F.; Zhang, L.; Wang, H.; Yu, H. Selective etching of gold nanorods by ferric chloride at room temperature. *CrystEngComm* **2009**, *11*, 2797-2803.
10. Keblinski, P.; Cahill, D. G.; Bodapati, A.; Sullivan, C. R.; Taton, T. A. Limits of localized heating by electromagnetically excited nanoparticles. *J. Appl. Phys.* **2006**, *100*, 054305.
11. Nguyen, S. C.; Zhang, Q.; Manthiram, K.; Ye, X.; Lomont, J. P.; Harris, C. B.; Weller, H.; Alivisatos, A. P. Study of Heat Transfer Dynamics from Gold Nanorods to the Environment via Time-Resolved Infrared Spectroscopy. *ACS Nano* **2016**, *10*, 2144-2151.
12. Khurgin, J. B. How to deal with the loss in plasmonics and metamaterials. *Nat Nano* **2015**, *10*, 2-6.
13. Wang, J.; Ando, R. A.; Camargo, P. H. C. Controlling the Selectivity of the Surface Plasmon Resonance Mediated Oxidation of p-Aminothiophenol on Au Nanoparticles by Charge Transfer from UV-excited TiO2. *Angew. Chem. Int. Ed* **2015**, *54*, 6909-6912.
14. Wang, C.; Astruc, D. Nanogold plasmonic photocatalysis for organic synthesis and clean energy conversion. *Chem. Soc. Rev.* **2014**, *43*, 7188-7216.
15. Wang, F.; Li, C.; Chen, H.; Jiang, R.; Sun, L.-D.; Li, Q.; Wang, J.; Yu, J. C.; Yan, C.-H. Plasmonic Harvesting of Light Energy for Suzuki Coupling Reactions. *J. Am. Chem. Soc.* **2013**, *135*, 5588-5601.
16. Tsukamoto, D.; Shiraishi, Y.; Sugano, Y.; Ichikawa, S.; Tanaka, S.; Hirai, T. Gold Nanoparticles Located at the Interface of Anatase/Rutile TiO2 Particles as Active Plasmonic Photocatalysts for Aerobic Oxidation. *J. Am. Chem. Soc.* **2012**, *134*, 6309-6315.
17. Tanaka, A.; Hashimoto, K.; Kominami, H. Preparation of Au/CeO2 Exhibiting Strong Surface Plasmon Resonance Effective for Selective or Chemoselective Oxidation of Alcohols to Aldehydes or Ketones in Aqueous Suspensions under Irradiation by Green Light. *J. Am. Chem. Soc.* **2012**, *134*, 14526-14533.
18. Zheng, Z.; Huang, B.; Qin, X.; Zhang, X.; Dai, Y.; Whangbo, M.-H. Facile in situ synthesis of visible-light plasmonic photocatalysts M@TiO2 (M = Au, Pt, Ag) and evaluation of their photocatalytic oxidation of benzene to phenol. *J. Mater. Chem.* **2011**, *21*, 9079-9087.
19. Kowalska, E.; Abe, R.; Ohtani, B. Visible light-induced photocatalytic reaction of gold-modified titanium(iv) oxide particles: action spectrum analysis. *Chem. Commun.* **2009**, 241-243.

20. Chen, X.; Zhu, H.-Y.; Zhao, J.-C.; Zheng, Z.-F.; Gao, X.-P. Visible-Light-Driven Oxidation of Organic Contaminants in Air with Gold Nanoparticle Catalysts on Oxide Supports. *Angew. Chem.* **2008**, *120*, 5433-5436.
21. Yang, J.; Li, Y.; Zu, L.; Tong, L.; Liu, G.; Qin, Y.; Shi, D. Light-Concentrating Plasmonic Au Superstructures with Significantly Visible-Light-Enhanced Catalytic Performance. *ACS Appl. Mater. Interfaces* **2015**, *7*, 8200-8208.
22. Li, P.; Ma, B.; Yang, L.; Liu, J. Hybrid single nanoreactor for in situ SERS monitoring of plasmon-driven and small Au nanoparticles catalyzed reactions. *Chem. Commun.* **2015**, *51*, 11394-11397.
23. Kang, L.; Han, X.; Chu, J.; Xiong, J.; He, X.; Wang, H.-L.; Xu, P. In Situ Surface-Enhanced Raman Spectroscopy Study of Plasmon-Driven Catalytic Reactions of 4-Nitrothiophenol under a Controlled Atmosphere. *Chemcatchem* **2015**, *7*, 1004-1010.
24. Hajfathalian, M.; Gilroy, K. D.; Yaghoubzade, A.; Sundar, A.; Tan, T.; Hughes, R. A.; Neretina, S. Photocatalytic Enhancements to the Reduction of 4-Nitrophenol by Resonantly Excited Triangular Gold–Copper Nanostructures. *J. Phys. Chem. C* **2015**, *119*, 17308-17315.
25. Ding, Q.; Chen, M.; Li, Y.; Sun, M. Effect of aqueous and ambient atmospheric environments on plasmon-driven selective reduction reactions. **2015**, *5*, 10269.
26. Collado, L.; Reynal, A.; Coronado, J. M.; Serrano, D. P.; Durrant, J. R.; de la Peña O'Shea, V. A. Effect of Au surface plasmon nanoparticles on the selective CO2 photoreduction to CH4. *Appl. Catal., B* **2015**, *178*, 177-185.
27. Fasciani, C.; Alejo, C. J. B.; Grenier, M.; Netto-Ferreira, J. C.; Scaiano, J. C. High-Temperature Organic Reactions at Room Temperature Using Plasmon Excitation: Decomposition of Dicumyl Peroxide. *Org. Lett.* **2011**, *13*, 204-207.
28. Zhu, H.; Ke, X.; Yang, X.; Sarina, S.; Liu, H. Reduction of Nitroaromatic Compounds on Supported Gold Nanoparticles by Visible and Ultraviolet Light. *Angew. Chem. Int. Ed* **2010**, *49*, 9657-9661.
29. Mukherjee, S.; Libisch, F.; Large, N.; Neumann, O.; Brown, L. V.; Cheng, J.; Lassiter, J. B.; Carter, E. A.; Nordlander, P.; Halas, N. J. Hot Electrons Do the Impossible: Plasmon-Induced Dissociation of H2 on Au. *Nano Lett.* **2013**, *13*, 240-247.
30. Dorel, R.; Echavarren, A. M. Gold(I)-Catalyzed Activation of Alkynes for the Construction of Molecular Complexity. *Chem. Rev.* **2015**, *115*, 9028-9072.
31. Wang, W.; Hammond, G. B.; Xu, B. Ligand Effects and Ligand Design in Homogeneous Gold(I) Catalysis. *J. Am. Chem. Soc.* **2012**, *134*, 5697-5705.
32. Gorin, D. J.; Sherry, B. D.; Toste, F. D. Ligand Effects in Homogeneous Au Catalysis. *Chem. Rev.* **2008**, *108*, 3351-3378.
33. Gorin, D. J.; Toste, F. D. Relativistic effects in homogeneous gold catalysis. *Nature* **2007**, *446*, 395-403.

34. Witham, C. A.; Huang, W.; Tsung, C.-K.; Kuhn, J. N.; Somorjai, G. A.; Toste, F. D. Converting homogeneous to heterogeneous in electrophilic catalysis using monodisperse metal nanoparticles. *Nat. Chem.* **2010**, *2*, 36-41.
35. Oliver-Meseguer, J.; Cabrero-Antonino, J. R.; Domínguez, I.; Leyva-Pérez, A.; Corma, A. Small Gold Clusters Formed in Solution Give Reaction Turnover Numbers of 107 at Room Temperature. *Science* **2012**, *338*, 1452-1455.
36. Herzing, A. A.; Kiely, C. J.; Carley, A. F.; Landon, P.; Hutchings, G. J. Identification of Active Gold Nanoclusters on Iron Oxide Supports for CO Oxidation. *Science* **2008**, *321*, 1331-1335.
37. Gross, E.; Shu, X.-Z.; Alayoglu, S.; Bechtel, H. A.; Martin, M. C.; Toste, F. D.; Somorjai, G. A. In Situ IR and X-ray High Spatial-Resolution Microspectroscopy Measurements of Multistep Organic Transformation in Flow Microreactor Catalyzed by Au Nanoclusters. *J. Am. Chem. Soc.* **2014**, *136*, 3624-3629.
38. Gross, E.; Toste, F. D.; Somorjai, G. A. Polymer-Encapsulated Metallic Nanoparticles as a Bridge Between Homogeneous and Heterogeneous Catalysis. *Catal. Lett.* **2015**, *145*, 126-138.
39. Gross, E.; Liu, J. H.; Alayoglu, S.; Marcus, M. A.; Fakra, S. C.; Toste, F. D.; Somorjai, G. A. Asymmetric Catalysis at the Mesoscale: Gold Nanoclusters Embedded in Chiral Self-Assembled Monolayer as Heterogeneous Catalyst for Asymmetric Reactions. *J. Am. Chem. Soc.* **2013**, *135*, 3881-3886.
40. Gross, E.; Liu, J. H.-C.; Toste, F. D.; Somorjai, G. A. Control of selectivity in heterogeneous catalysis by tuning nanoparticle properties and reactor residence time. *Nat. Chem.* **2012**, *4*, 947-952.
41. Li, Y.; Liu, J. H.-C.; Witham, C. A.; Huang, W.; Marcus, M. A.; Fakra, S. C.; Alayoglu, P.; Zhu, Z.; Thompson, C. M.; Arjun, A.; Lee, K.; Gross, E.; Toste, F. D.; Somorjai, G. A. A Pt-Cluster-Based Heterogeneous Catalyst for Homogeneous Catalytic Reactions: X-ray Absorption Spectroscopy and Reaction Kinetic Studies of Their Activity and Stability against Leaching. *J. Am. Chem. Soc.* **2011**, *133*, 13527-13533.
42. Huang, W.; Liu, J. H.-C.; Alayoglu, P.; Li, Y.; Witham, C. A.; Tsung, C.-K.; Toste, F. D.; Somorjai, G. A. Highly Active Heterogeneous Palladium Nanoparticle Catalysts for Homogeneous Electrophilic Reactions in Solution and the Utilization of a Continuous Flow Reactor. *J. Am. Chem. Soc.* **2010**, *132*, 16771-16773.
43. Jin, R.; Zeng, C.; Zhou, M.; Chen, Y. Atomically Precise Colloidal Metal Nanoclusters and Nanoparticles: Fundamentals and Opportunities. *Chem. Rev.* **2016**, *116*, 10346-10413.
44. Ye, R.; Yuan, B.; Zhao, J.; Ralston, W. T.; Wu, C.-Y.; Unel Barin, E.; Toste, F. D.; Somorjai, G. A. Metal Nanoparticles Catalyzed Selective Carbon–Carbon Bond Activation in the Liquid Phase. *J. Am. Chem. Soc.* **2016**, *138*, 8533-8537.

Chapter 8 - Effects of Acidic Properties of Mesoporous Zeolites Supporting Pt Nanoparticles on Hydrogenative Conversions of Methylcyclopentane

(This chapter covers similar material as in Na, K.; Alayoglu, S.; Ye, R.; Somorjai, G. A. *J. Am. Chem. Soc.* **2014**, *136*, 17207-17212. – reproduced with permission, copyright 2014 American Chemical Society.)

Abstract

The effect of acidic properties of mesoporous zeolites on the control of product selectivity during the hydrogenative isomerization of methylcyclopentane has been investigated. A series of mesoporous zeolites with controlled acidic properties were prepared by postdealumination process with hydrochloric acid under hydrothermal conditions, and the resultant zeolites used for supporting colloidal Pt nanoparticles (NPs) with a mean size of 2.5 nm (±0.6 nm). As compared to the pure Pt NPs supported on catalytically inert mesoporous silica (MCF-17) as the reference catalyst that can produce isomers most selectively (~80%), the Pt NPs supported on mesoporous zeolites produced C_6-cyclic hydrocarbons (i.e., cyclohexane and benzene) most dominantly. The type and strength of the Brönsted (B) and Lewis (L) acid sites of those zeolites with a controlled Al amount are analyzed by using FT-IR after the adsorption of pyridine and NH_3 temperature-programmed desorption measurements, and they are correlated with the selectivity change between cyclohexane and benzene. From this investigation, we found a linear relationship between the number of Brönsted acid sites and the formation rate for cyclohexane. In addition, we revealed that more Lewis acidic zeolite having relatively smaller B/L ratio is effective for the cyclohexane formation, whereas more Brönsted acidic zeolite having relatively larger B/L ratio is effective for the benzene formation.

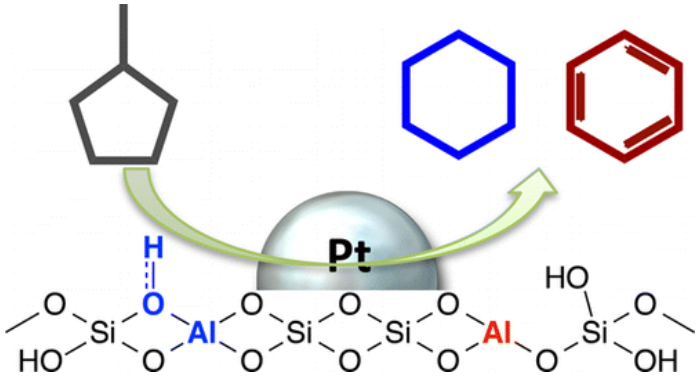

8.1 Introduction

Supported metal nanoparticle (NP) catalysts are the typical form of heterogeneous catalysts used ubiquitously in the current chemical industries.[1-5] The surface of a metal NP is the catalytic site on which the reactant can be adsorbed and converted to various product molecules. The molecular interaction to the surface of metal NPs can affect the overall catalytic activity and the product selectivity.[6-9] Size, shape, and composition of metal NPs are also crucial factors for controlling the reaction processes. [6-9] In practical reaction processes, the metal NPs are used as the catalytic sites after supporting on the robust inorganic support materials of porous materials with high surface area and large pore volume.[10-13] Therefore, the structural properties of supporting materials also possess prominent functions that can critically influence the reactions.[14-16]

Among the various porous inorganic materials, zeolites are greatly contributing to the heterogeneous catalytic reactions.[17-19] In current chemical industries, zeolites occupy more than 40% among the whole solid catalysts, which is the largest portion, followed by metal oxides.[17] Zeolites have a charge-localized surface due to the presence of isolated heteroatoms such as Al, Sn, V, and Ti that are covalently surrounded by crystalline microporous silicon oxide framework.[20-22] Zeolites can catalyze many reactions over the charge-localized atomic sites on the zeolite surface that can induce the catalytic reactions through forming an acid–base pair with reactant molecules. Zeolites can usually do the catalysis alone, but they can also make catalytic synergies when metal NPs are supported on them. Such combinations of metal NPs with zeolites make an interface between them, which can sometimes make considerable changes in catalytic activity and product selectivity.[11] Particularly in the viewpoint of product selectivity, achieving 100% product selectivity to a single desired product would become much more feasible through the rational design of catalyst system.[23-25]

In this work, we investigated the effect of acidic properties of zeolite on the control of product selectivity and catalytic activity during model hydrogenative isomerization of methylcyclopentane (MCP). We used mesoporous BEA zeolites having secondary mesopores within nanocrystalline zeolite particles to control the amount and strength of Brönsted and Lewis acid sites for elucidating effects of acidic properties on the selectivity control during the MCP/H_2 reaction under ambient pressure at 150 °C. The acidic properties of mesoporous zeolite were controlled by systematic postdealumination with different concentrations of hydrochloric acid and hydrothermal condition,[26] where 2.5 nm Pt NPs were supported inside mesopore voids with the mean diameter of 15 nm to build catalytic architectures with Pt/zeolite interfaces.

8.2 Experimental section

Mesoporous BEA zeolite and mesoporous silica MCF-17 were synthesized by following the literature reported elsewhere.[10,27]

For postdealumation of mesoporous BEA zeolite, 0.5 g of H^+-exchanged mesoporous BEA zeolite was diluted in 20 mL of 1–2 M HCl solutions, and heated for 30–90 min under reflux condition. After treatment, the zeolite was collected by filtration, washed with distilled water three times, and dried in an oven at 120 °C. The resultant mesoporous BEA zeolite was denoted as BEA-*x*, where *x* is the content (%) of Al in the zeolite framework.

Poly(vinylpyrrolidone) (PVP)-capped Pt NPs with an average size of 2.5 nm were synthesized by following the literature reported elsewhere.[16] The PVP-capped Pt NPs were supported on the mesoporous BEA zeolites with controlled Al amount and mesoporous silica MCF-17.

The catalytic materials synthesized in this work were characterized with X-ray diffraction (XRD), transmission electron microscope (TEM), inductively coupled plasma atomic emission spectroscopy (ICP-AES), N_2 physisorption analysis, FT-IR analysis and NH_3 temperature-programmed desorption (TPD). The catalytic testing was performed using lab-build plug-flow reactor connected to a gas chromatograph (GC) equipped with FID detector

8.3 Results and discussion

8.3.1 Pt metal NPs supported mesoporous BEA zeolites with controlled acidity

Upon postdealumination, Al contents in mesoporous BEA zeolites were systematically controlled. The resultant mesoporous BEA zeolites with controlled amount of Al were further characterized with ICP-AES, XRD, FT-IR, and NH_3 TPD before supporting Pt metal nanoparticles. According to the ICP-AES, the total Al content decreased from 10% to 4%, 1% and 0.5% upon postdealumination. No significant collapse of zeolite framework was observed according to the XRD analysis. N_2 adsorption analysis also proved that the series of dealuminated BEA zeolites possessed similar pore properties to the pristine BEA zeolite (see Table 1 for pore analysis data).

The acidic properties of mesoporous BEA zeolites were investigated by FT-IR after the adsorption of pyridine as a probe base molecule and TPD experiments after the adsorption of NH_3 (Figure 1). The IR data shows the stretching bands of pyridine adsorbed on the Brönsted (B) and Lewis (L) acid sites at 1550 and 1450 cm^{-1}, respectively (Figure 1A). The selective quantification of both acid sites was carried out with adsorption coefficients,[28] which shows that the number of acid sites decreased proportionally to the total Al contents upon postdealumination (Figure 1B and Table 1). The pristine mesoporous BEA zeolite (BEA-10) showed the largest amount of Brönsted acid sites (0.98 mmol/g) with comparable amount of Lewis acid sites (0.58 mmol/g). The ratio between Brönsted and Lewis acid sites (B/L ratio) is 1.69. The B/L ratio was progressively increased with the decrease of Al contents in the dealuminated BEA zeolites (Table 1). This result indicates that the Lewis acid sites are dealuminated more preferably than the Brönsted acid sites upon hydrochloric acid treatment. As already

reported in literatures, the Lewis acid sites are mostly originated from the extraframework Al Species that can be leached out by aqueous acid more easily than Brönsted acid sites surrounded tetrahedrally by −O–Si bonds.[26]

Table 1. Quantification of acid sites according to the FT-IR and NH_3 TPD experiments

	BET surface area[a]	Pore size[b]	Pore volume[c]	Pt[d]
BEA-10	755	20	0.85	0.49
BEA-4	815	18	0.93	0.51
BEA-1	770	11	0.86	0.52
BEA-0.5	865	13	1.23	0.48

(continue)

	IR			NH_3 TPD			
	B[e]	L[f]	B/L[g]	L_w[h]	B_w[i]	B_M[j]	B_s[k]
BEA-10	0.98	0.58	1.69	0.568	0.388	0.359	0.247
	(1545)[l]	(1541)[l]		(130)[m]	(196)[m]	(274)[m]	(522)[m]
BEA-4	0.43	0.21	2.05	0.228	0.158	0.145	0.109
	(1548)[l]	(1449)[l]		(123)[m]	(174)[m]	(227)[m]	(550)[m]
BEA-1	0.12	0.04	3.00	0.042	0.038	0.042	0.038
	(1550)[l]	(1448)[l]		(105)[m]	(157)[m]	(187)[m]	(660)[m]
BEA-0.5	0.07	0.01	7.00	0.011	0.024	0.013	0.032
	(1552)[l]	(1447)[l]		(89)[m]	(140)[m]	(198)[m]	(707)[m]

[a]BET surface area calculated by Brunauer–Emmett–Teller method (m^2/g). [b]Average size of mesopore (nm). [c]Total pore volume calculated by BJH method (cm^3/g). [d]Pt loading (wt %) of Pt NPs supported zeolites determined by ICP-AES. [e and f](*e*) Brönsted and (*f*) Lewis acid sites (mmol/g). [g]Relative ratio of B/L. [h]Lewis acid sites with weak strength, [i–k]Brönsted acid sites with (i) weak, (j) medium, and (k) strong strength. [l]Center of the IR peak (cm^{-1}). [m]Center of the deconvoluted TPD profile (°C).

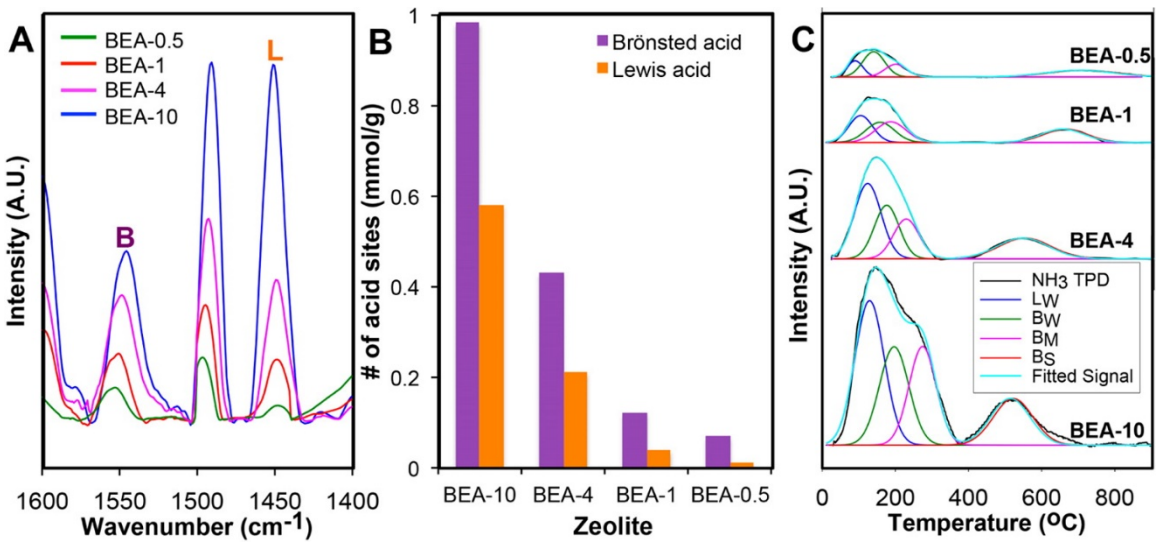

Figure 1. (A) FT-IR spectra after the adsorption of pyridine followed with desorption at 150 °C of BEA-10, 4, 1, and 0.5 (blue, pink, red and green, respectively), where Brönsted (B) and Lewis (L) acid sites are observed at around 1550 and 1450 cm^{-1}, respectively. (B) Quantification of Brönsted and Lewis acid sites of zeolites from FT-IR spectra in (A). (C) NH_3 temperature-programmed desorption (TPD) profiles for BEA-10, 4, 1, and 0.5 (from bottom to top), where each TPD profile was deconvoluted into four distinct peaks of weak Lewis acid sites (L_W, blue) and Brönsted acid sites with weak (B_W, green), medium (B_M, pink) and strong (B_S, red) strengths. The fitted signals from four peaks were also drawn together (cyan).

Figure 1C shows NH_3 TPD profiles of mesoporous BEA zeolites, showing the desorption phenomena of NH_3 molecules adsorbed on the acid sites upon increase of temperature. The TPD profiles can be deconvoluted further to four peaks according to the desorption temperature. For example, NH_3 TPD profile of pristine zeolite BEA-10 can be deconvoluted to four peaks at 130, 196, 274, and 522 °C that can be assigned by desorption of pyridine from Lewis acid sites with weak strength (L_W), Brönsted acid sites with weak (B_W), medium (B_M), and strong (B_S) strengths, respectively. Table 1 summarized the quantification results of the series of BEA zeolites from NH_3TPD profiles in comparison with values calculated by FT-IR. For the analysis of the NH_3-TPD spectra, a protocol was employed in which the calculated B/L ratios form the pyridine-probed FTIR spectra were used as constraints to slave the peak deconvolution.

On the series of BEA zeolite with controlled Al contents, Pt NPs with mean diameter of 2.5 nm were supported. The Pt NPs were synthesized by colloidal synthesis reaction of H_2PtCl_6 precursor salt in ethylene glycol in the presence of PVP as the capping agent. Prior to catalytic runs, the catalysts were conditioned in 150 Torr O_2 at 250 °C and in 150 Torr H_2 at 150 °C, which were found as the optimum conditions to treat the residual PVP capping and activate Pt NPs.[10] The Pt NPs were supported with

good dispersion. In addition, as proved by TEM, the dealuminated mesoporous BEA zeolites have very similar morphology with the pristine mesoporous BEA zeolite (BEA-10) before postdealumination. The crystalline lattice fringes from the microporous zeolite framework were also observed clearly over the zeolite catalysts, which indicated that no significant structural collapse of zeolite framework occurred upon postdealumination with HCl.

8.3.2 Catalytic hydrogenative conversion of methylcyclopentane

The series of mesoporous BEA zeolites with and without supporting Pt metal NPs was tested for the MCP/H_2 reaction. In Scheme 1, MCP can be converted into various hydrocarbon species via reforming pathways such as dehydrogenation to olefins (1, green), ring-opening isomerization to acyclic isomers (2, pink), ring-enlargement cyclization to cyclohexane (3, blue) or benzene (4, red), and cracking to C_1–C_5 hydrocarbons (5, gray). Figure 2A shows the product selectivity during the MCP/H_2 reaction over the tested catalysts. As shown in Figure 2A, 2.5 nm PVP-capped Pt metal NPs supported on the mesoporous silica (Pt/SiO_2) produced acyclic isomers most dominantly (pink, ~80%) and a lesser amount of olefin products (green, ~20%). Note that the pure mesoporous silica without supporting Pt NPs has no catalytic activity, and hence Pt/SiO_2 is the catalyst for giving a sole function of Pt NPs for this reaction.

Scheme 1. Schematic drawing for the reaction of methylcyclopentane reforming

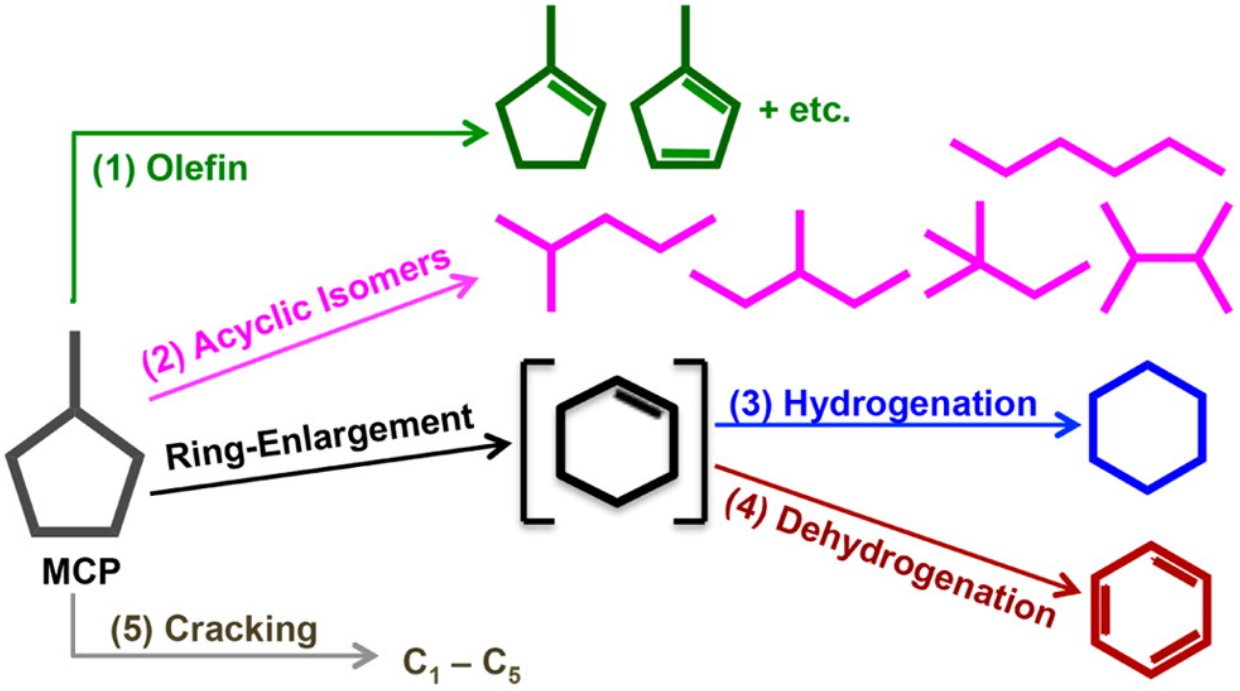

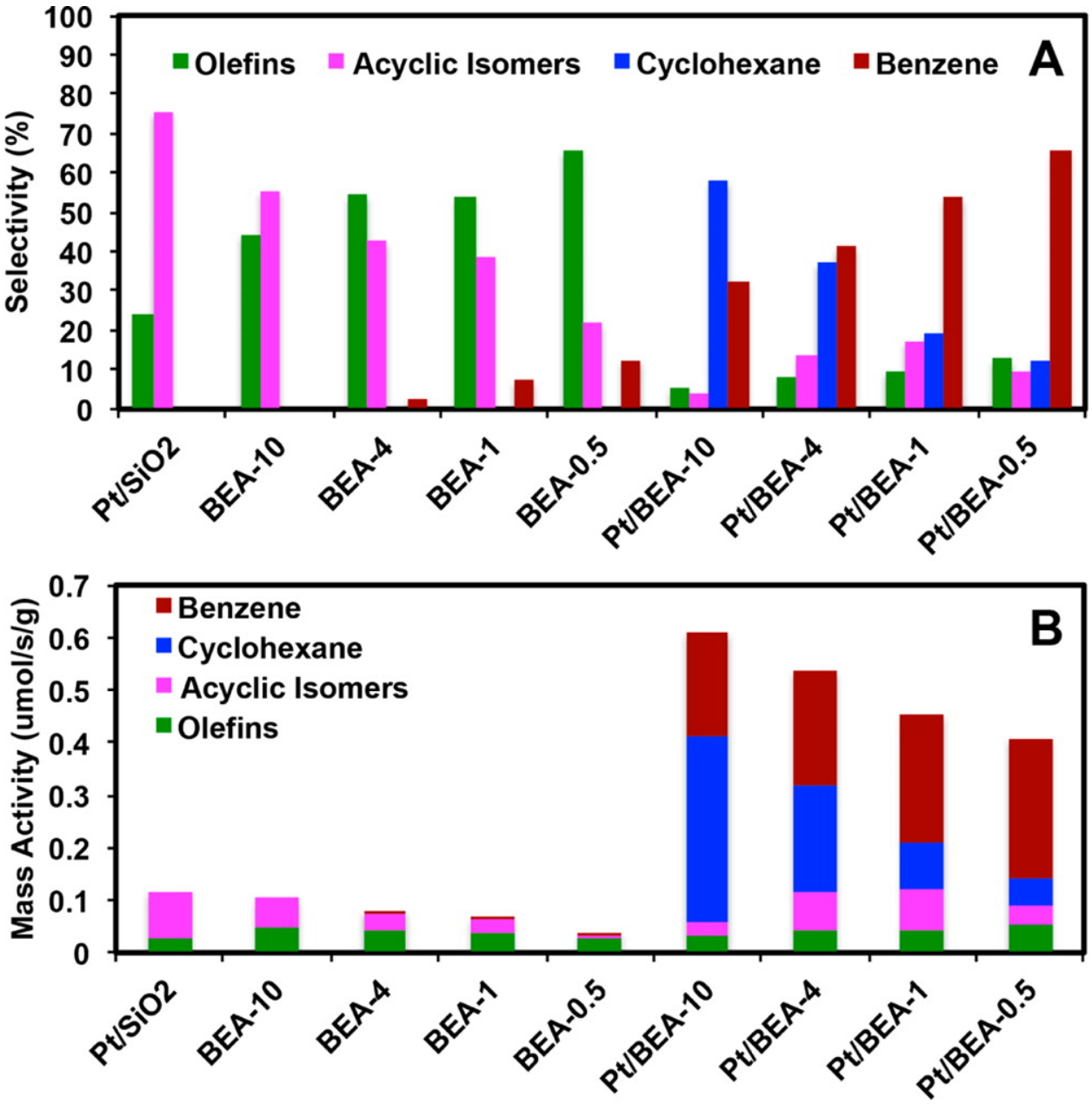

Figure 2. (A) Product selectivity (%) and (B) mass activity data over tested catalysts based on the catalyst weight (μmol/(s/g)).

The effect of making catalytic interface between Pt and acid sites on the zeolite surface was investigated after supporting Pt NPs on the series of mesoporous BEA zeolites. In contrast to the Pt/SiO_2, the major products over Pt/zeolites were C_6-cyclic hydrocarbons such as cyclohexane (blue) and benzene (red) that are ring-enlarged products from MCP. It is highly remarkable that such ring-enlarged hydrocarbons were not formed over Pt/SiO_2 at the same reaction condition (150 °C). Benzene can only be

produced over Pt/SiO_2 when the reaction temperature approached 250 °C. However, cyclohexane was not obtained over Pt/SiO_2 no matter how the reaction condition was changed. The favorable formation of C_6-cyclic hydrocarbons can be attributed to the synergistic catalytic actions at the interface of Pt and acid sites on the zeolite surface. Interestingly, the relative selectivity ratio between cyclohexane and benzene was progressively changed according to the acidic properties of zeolite supports. Pt/BEA-10 zeolite produced the largest product selectivity to cyclohexane (58%) followed with 32% of benzene. The selectivity to cyclohexane decreased upon decrease of Al content in the mesoporous BEA zeolite, while the benzene selectivity increased at the expense of cyclohexane decrease. Hence, Pt/BEA-0.5 zeolite produced the largest amount of benzene (65%) with 12% of cyclohexane. This is in similar trend with our previous findings over Pt/MFI catalyst with similar ratios of Al/Si and Pt/Al as the Pt/BEA-0.5 catalyst.[10]

The four pure mesoporous BEA zeolites without supporting Pt NPs were investigated in order to elucidate the sole roles of mesoporous BEA zeolites in the absence of Pt NPs. The results show that these pure zeolites behave like Pt/SiO_2. They could also produce both acyclic isomers (pink) and olefin products (green). The result demonstrated that the role of acidic sites on the zeolite surface is quite similar to the role of Pt NPs, both of which are responsible for dehydrogenation via C–H bond activation and ring-opened isomerization via activations of C–C and C–H bonds. However, the product selectivities toward olefins and acyclic isomers were different depending on the catalyst. BEA-10 zeolite could produce more acyclic isomers, whereas BEA-0.5 zeolite produced more olefins. In addition, small amount of benzene (2.7–12.6%) was also produced over BEA-4, 1, and 0.5 zeolites, where its amount was progressively increased upon the decrease of Al content.

Figure 2B shows the mass activity data for the tested catalysts based on the catalyst weight. The mass activity decreased upon the decrease of Al contents. Pt/BEA-10 showed 0.61 μmol/s/g of total mass activity, which was about six times higher activity than the pure zeolite (i.e., BEA-10). The mass activity decreased to 0.41 μmol/(s/g) for Pt/BEA-0.5, which was also about five times higher activity than pure zeolite (i.e., BEA-0.5). The fact that acyclic isomers and olefin products did not change at any significant rate (see horizontal line in Figure 3A), and the absence of cyclohexane for pure zeolite supports and pure Pt (i.e., SiO_2 is inert) indicates that the reaction could be decomposed into two major pathways: (i) hydrogen extraction and hydrogenative ring-opening over individual Pt and acidic zeolite sites, decoupled from one another; and (ii) hydrogenative ring closure that led to cyclohexene intermediate, not observed in the effluent gas mixture only to be revealed by SFG vibrational spectroscopy,[10] and subsequent hydrogenation/dehydrogenation at the interface of Pt and acidic sites of zeolite.

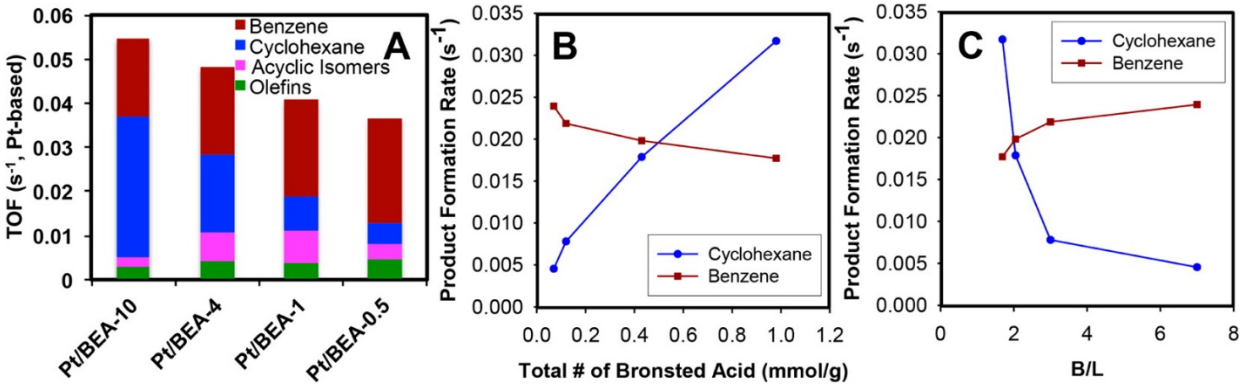

Figure 3. (A) Turnover frequency (TOF, s^{-1}) of Pt NPs supported catalysts. TOFs were calculated based on the number of Pt atoms exposed at the surface of 2.5 nm-Pt NPs, assuming that all the surface Pt sites were reduced at 250 °C under H_2 gas. Each bar is divided into product formation rates for olefins (green), acyclic isomers (pink), cyclization to cyclohexane (blue) and cyclization/dehydrogenation to benzene (red). (B) Correlation of product formation rates (s^{-1}) for cyclohexane (blue) and benzene (red) with the total amount of Brönsted acid sites (mmol/g), and (B) with the relative ratio of Brönsted and Lewis acid sites (B/L).

To elaborate this last conclusion that invokes a multipath chemistry at some dynamic interface, the number densities of acid sites around Pt NPs were calculated for different BEA supports. Monodisperse Pt NPs and uniformly distributed aluminosilicate framework of zeolite could render modeling based on simple geometric variables and physical constraints (i.e., surface area, %Pt loading, NH_3-TPD results) possible. With this model, the numbers of different acid sites (Lewis and various Brönsted sites) were calculated along the surface plane and in concentric domains away from Pt NP surfaces. It was found that there is, in average, 1 Lewis and 7 Brönsted acid sites within approximately 5 nm of Pt NP surfaces for the BEA-0.5 support. It should be noted that these numbers are negligibly small as compared to the large number of surface Pt atoms per NP (approximately 250). However, 60 Lewis and 110 Brönsted acid sites were calculated using the same model and identical radial distance for the BEA-10 support. The implications of this observation are 2-fold. First, the probability that a surface Pt atom would see an acid side of any kind within the bonding vicinity (0–3 Å) is very small in general, and approaches to zero in the case of BEA-0.5. This suggests Pt surface intermediate should spillover to zeolite surface and diffuse several nanometers before encountering, at any significant probability, with any acid site. Second, the changes in overall activity, both mass-based and surface-normalized, are within 30% for the Pt/BEA catalyst for Al concentrations in the 0.5–10% range. This indicates that the ring enlargement chemistry over the zeolites should be the rate-limiting step while the spillover and diffusion processes should be relatively fast. This also implies that the

cyclization reaction might still take place on the zeolite support within the bonding proximity of surface Pt atoms.

8.3.3 Correlation of acidic properties with product formation rates

Given the systematic changes in product selectivity between cyclohexane and benzene over the series of Pt/BEA catalysts, one should turn into particular structure–reactivity correlations based on the acidic properties of zeolite supports. To this end, the product formation rates (s^{-1}) were correlated with the number distributions of various acidic sites of different types and strengths; this is illustrated in Figure 3B. It was found that the formation of cyclohexane dramatically increased with increasing the number of Brönsted sites, summed over different strengths, whereas benzene formation showed a slight negative slope. It should be noted that the strengths of various Brönsted sites (weak, medium and strong) were defined in the broadest definition of the term, referring to the low, medium and high temperature NH_3 desorption peaks. The relative strengths of various Brönsted sites are, however, different for the Pt/BEA catalysts. In general, strong Brönsted sites increased in strength (i.e., higher desorption temperature of NH_3) in the order BEA-10 < BEA-4 < BEA-1 < BEA-0.5, while weak and medium Brönsted sites decreased in strength in the same order (Figure 1C). Pyridine-probed FT-IR study also indicated an increase in average vibrational frequency of pyridine adsorbed on Brönsted sites from BEA-10 to BEA-0.5 (Figure 1A) and, therefore, corroborated the conclusions drawn from the analysis of NH_3-TPD data. Likewise, the relative strengths of weak Lewis sites increased in the order BEA-0.5 < BEA-1 < BEA-4 < BEA-10, indicated by the NH_3-TPD and pyridine-probed FT-IR results. Therefore, the selectivity switchover from cyclohexane to benzene for the Pt/BEA catalysts (i.e., the ease of hydrogen extraction) could be single-handedly delivered by the presence of strong Brönsted sites, in particular, those that exhibited stronger bonding with the base molecules as in the case of BEA-0.5. In support of this, it should be noted that pure BEA-0.5 led to the formation of benzene in low, yet measurable amounts, while pure BEA-10 did not produce any measurable cyclic isomers.

Alternative to this view, the Lewis acid sites could interact with C═C double bonds, present in either benzene or cyclohexene intermediate, by forming π-complex with aluminum at Lewis acid sites. If correct, this should lead to stronger (weak) Lewis acid sites for the Pt/BEA-0.5 catalyst than the Pt/BEA-10 catalyst. Our findings, however, indicate the opposite trend; the desorption temperature of NH_3 over the Pt/BEA-10 catalyst was higher than that over the Pt/BEA-0.5 catalyst (130 vs 89 °C in Table 1). Furthermore, the number of weak Lewis sites over the Pt/BEA-10 outmatched those over the Pt/BEA-0.5 by 50:1. Nonetheless, it should be noted that we tried and found a correlation between the B/L ratios and formation rate toward benzene; the larger the B/L ratio, the higher the formation rate toward benzene, and vice versa (Figure 3C).

8.4 Conclusion

In conclusion, effect of the acidic properties of mesoporous zeolites supporting Pt NPs has been investigated for the hydrogenative reforming of MCP. The sole Pt NPs and the pure mesoporous zeolites without Pt NPs have similar catalytic functions that can make olefin and acyclic isomer products with different selectivity. However, making catalytic interfaces of Pt NPs with acid sites on the zeolite surface enhanced the activity very significantly and hence lowered the temperature for the formation of C_6-cyclic hydrocarbons by ~100 °C as compared to the Pt/SiO_2. In particular, relative selectivities between cyclohexane and benzene were systematically changed according to the mesoporous BEA zeolites. The cyclohexane formation rate increased linearly with the increased number of Brönsted acid sites. In particular, the larger the Brönsted/Lewis ratio in the zeolite framework, the higher the formation rate toward benzene, and vice versa. The present work provides the detailed effect of acidic sites on the selective formation of C_6-cyclic hydrocarbons, such as cyclohexane and benzene. The results described in this work promote the zeolite-based solid acids supporting metal nanoparticles as potential catalyst candidates for selective C–C and C–H bond activations.

8.5 References

1. Campelo, J. M.; Luna, D.; Luque, R.; Marinas, J. M.; Romero, A. A. Sustainable Preparation of Supported Metal Nanoparticles and Their Applications in Catalysis. *ChemSusChem* **2009**, *2*, 18-45.
2. White, R. J.; Luque, R.; Budarin, V. L.; Clark, J. H.; Macquarrie, D. J. Supported metal nanoparticles on porous materials. Methods and applications. *Chem. Soc. Rev.* **2009**, *38*, 481-494.
3. Zheng, N.; Stucky, G. D. A General Synthetic Strategy for Oxide-Supported Metal Nanoparticle Catalysts. *J. Am. Chem. Soc.* **2006**, *128*, 14278-14280.
4. Samant, M. G.; Boudart, M. Support effects on electronic structure of platinum clusters in Y zeolite. *The Journal of Physical Chemistry* **1991**, *95*, 4070-4074.
5. Corma, A.; Garcia, H. Supported gold nanoparticles as catalysts for organic reactions. *Chem. Soc. Rev.* **2008**, *37*, 2096-2126.
6. Somorjai, G. A.; Park, J. Y. Colloid Science of Metal Nanoparticle Catalysts in 2D and 3D Structures. Challenges of Nucleation, Growth, Composition, Particle Shape, Size Control and Their Influence on Activity and Selectivity. *Top. Catal.* **2008**, *49*, 126-135.
7. Tsung, C.-K.; Kuhn, J. N.; Huang, W.; Aliaga, C.; Hung, L.-I.; Somorjai, G. A.; Yang, P. Sub-10 nm Platinum Nanocrystals with Size and Shape Control: Catalytic Study for Ethylene and Pyrrole Hydrogenation. *J. Am. Chem. Soc.* **2009**, *131*, 5816-5822.
8. Joo, S. H.; Park, J. Y.; Renzas, J. R.; Butcher, D. R.; Huang, W.; Somorjai, G. A. Size Effect of Ruthenium Nanoparticles in Catalytic Carbon Monoxide Oxidation. *Nano Lett.* **2010**, *10*, 2709-2713.

9. Pushkarev, V. V.; Musselwhite, N.; An, K.; Alayoglu, S.; Somorjai, G. A. High Structure Sensitivity of Vapor-Phase Furfural Decarbonylation/Hydrogenation Reaction Network as a Function of Size and Shape of Pt Nanoparticles. *Nano Lett.* **2012**, *12*, 5196-5201.
10. Alayoglu, S.; Aliaga, C.; Sprung, C.; Somorjai, G. A. Size and Shape Dependence on Pt Nanoparticles for the Methylcyclopentane/Hydrogen Ring Opening/Ring Enlargement Reaction. *Catal. Lett.* **2011**, *141*, 914-924.
11. Na, K.; Musselwhite, N.; Cai, X.; Alayoglu, S.; Somorjai, G. A. Promotional Effects of Mesoporous Zeolites with Pt Nanoparticle Catalysts during Reforming of Methylcyclopentane. *The Journal of Physical Chemistry A* **2014**, *118*, 8446-8452.
12. Li, H.; Bian, Z.; Zhu, J.; Zhang, D.; Li, G.; Huo, Y.; Li, H.; Lu, Y. Mesoporous Titania Spheres with Tunable Chamber Stucture and Enhanced Photocatalytic Activity. *J. Am. Chem. Soc.* **2007**, *129*, 8406-8407.
13. Prieto, G.; Martínez, A.; Concepción, P.; Moreno-Tost, R. Cobalt particle size effects in Fischer–Tropsch synthesis: structural and in situ spectroscopic characterisation on reverse micelle-synthesised Co/ITQ-2 model catalysts. *J. Catal.* **2009**, *266*, 129-144.
14. Schwab, G. M.; Koller, K. Combined action of metal and semiconductor catalysts. *J. Am. Chem. Soc.* **1968**, *90*, 3078-3080.
15. Boffa, A. B.; Lin, C.; Bell, A. T.; Somorjai, G. A. Lewis acidity as an explanation for oxide promotion of metals: implications of its importance and limits for catalytic reactions. *Catal. Lett.* **1994**, *27*, 243-249.
16. An, K.; Alayoglu, S.; Musselwhite, N.; Plamthottam, S.; Melaet, G.; Lindeman, A. E.; Somorjai, G. A. Enhanced CO Oxidation Rates at the Interface of Mesoporous Oxides and Pt Nanoparticles. *J. Am. Chem. Soc.* **2013**, *135*, 16689-16696.
17. Rinaldi, R.; Schuth, F. Design of solid catalysts for the conversion of biomass. *Energy Environ. Sci.* **2009**, *2*, 610-626.
18. Corma, A. State of the art and future challenges of zeolites as catalysts. *J. Catal.* **2003**, *216*, 298-312.
19. Vermeiren, W.; Gilson, J.-P. Impact of Zeolites on the Petroleum and Petrochemical Industry. *Top. Catal.* **2009**, *52*, 1131-1161.
20. Corma, A.; Nemeth, L. T.; Renz, M.; Valencia, S. Sn-zeolite beta as a heterogeneous chemoselective catalyst for Baeyer-Villiger oxidations. *Nature* **2001**, *412*, 423-425.
21. Camblor, M. A.; Corma, A.; Martinez, A.; Perez-Pariente, J. Synthesis of a titaniumsilicoaluminate isomorphous to zeolite beta and its application as a catalyst for the selective oxidation of large organic molecules. *J. Chem. Soc., Chem. Commun.* **1992**, 589-590.
22. Sen, T.; Chatterjee, M.; Sivasanker, S. Novel large-pore vanadium alumino- and boro-silicates with BEA structure. *J. Chem. Soc., Chem. Commun.* **1995**, 207-208.
23. H. Clark, J. Green chemistry: challenges and opportunities. *Green Chem.* **1999**, *1*, 1-8.

24. Bell, A. T. The Impact of Nanoscience on Heterogeneous Catalysis. *Science* **2003**, *299*, 1688-1691.
25. Burda, C.; Chen, X.; Narayanan, R.; El-Sayed, M. A. Chemistry and Properties of Nanocrystals of Different Shapes. *Chem. Rev.* **2005**, *105*, 1025-1102.
26. Zhang, W.; Smirniotis, P. G.; Gangoda, M.; Bose, R. N. Brønsted and Lewis Acid Sites in Dealuminated ZSM-12 and β Zeolites Characterized by NH3-STPD, FT-IR, and MAS NMR Spectroscopy. *J. Phys. Chem. B* **2000**, *104*, 4122-4129.
27. Na, K.; Choi, M.; Ryoo, R. Cyclic diquaternary ammoniums for nanocrystalline BEA, MTW and MFI zeolites with intercrystalline mesoporosity. *J. Mater. Chem.* **2009**, *19*, 6713-6719.
28. Ayrault, P.; Datka, J.; Laforge, S.; Martin, D.; Guisnet, M. Characterization of the Internal and External Acidity of H-MCM-22 Zeolites. *J. Phys. Chem. B* **2004**, *108*, 13755-13763.